LUND UNIVERSITY

Laser-Induced Incandescence for Soot Diagnostics: Theoretical Investigation and Experimental Development

Johnsson, Jonathan

2012

Doctoral Thesis

Laser-Induced Incandescence for Soot Diagnostics

Theoretical Investigation and Experimental Development

Jonathan Johnsson

Division of Combustion Physics
Department of Physics

LUND UNIVERSITY

Front cover image: Transmission electron microscope image of soot aggregates from a flame-based soot generator (see Sections 2.3.3 and 3.2). The carbon layer that the aggregates stick to has ruptured so that some aggregates can be seen hanging out from the edge of the layer. The large soot aggregate in the centre is approximately 2μm across.

Printed by Tryckeriet i E-huset, Lund University, Lund, Sweden
October 2012
Lund Reports on Combustion Physics, LRCP-164
ISSN 1102-8718
ISRN LUTFD2/TFCP-164-SE
ISBN 978-91-7473-397-6

Jonathan Johnsson
Division of Combustion Physics
Department of Physics
Lund University
P.O. Box 118
SE-221 00 Lund, Sweden

Abstract

Laser-induced incandescence, LII, is a laser-diagnostic technique that can be used to measure the volume fraction and the sizes of soot particles suspended in a gas, such as within a combustion process or in its exhausts. The technique is based on the facts that the time-decay of the radiation from laser-heated soot particles is directly related to the particle size in the probed volume, and that the time-integrated radiation is related to the soot volume fraction.

In the present work, the properties of LII were investigated, such as its dependence on different parameters, how it can be used to calculate soot properties and how it relates to and can be combined with other techniques. Both theoretical and experimental studies were carried out. An LII model was used for the theoretical work and its predictions under various conditions were investigated. The studies addressed different questions with regard to the sensitivity of LII to various parameters. Simulations were made to determine the best choices for the laser system settings when measuring the soot volume fraction under different conditions. This resulted in general suggestions for what practices are best under various conditions. It was also found that if the two modes of a bimodal particle size distribution are of about the same magnitude the smaller mode has no significant effect on the LII particle size evaluated. Studies of soot aggregates consisting of ramified clusters of spherical primary particles were carried out using numerically constructed aggregates, together with a Monte Carlo algorithm for calculating heat conduction. The effect of different degrees of bridging between the primary particles on primary particle size as evaluated with use of LII was examined, and found to be noticeable but relatively small.

A laser system was designed for use in the experimental studies and evaluation routines that use our LII model were designed and implemented, to be able to evaluate particle sizes from experimental LII signals. The experimental setup was designed so as to possess properties suitable for obtaining well-controlled LII particle size measurements. That setup was employed, with slight variations, for investigating the properties of LII. It was also applied in different laboratory soot sources for measurement of particle sizes and of soot volume fraction.

The same setup was used for studying the effects of the beam profile, which was found to have only a marginal effect on the evaluated size, other uncertain parameters involved in the LII technique being of greater importance in this respect. Two collaborative projects were also carried out for investigating how LII could be used for determining particle sizes both of cold soot aggregates obtained from a flame-based soot generator and of industrial carbon black samples. With use of the soot generator it was investigated, when the primary particle distributions were similar, if the differing decay rates of the LII signals could be explained by the differing degrees of aggregation. This could be an effect of the increase in shielding between the primary particles with an increase in aggregate size, as predicted by theory. The LII sizes as determined for the carbon black samples were closely correlated with the equivalent particle sizes as determined by industrial surface-area analysis of the particles.

The properties of a flat ethylene/air flame on a McKenna burner were also investigated, as a function both of height and of radial position. The absorption function for soot was found to increase with an increase in height from 6 to 14 mm above the burner, due probably to the changes that occurred in soot composition from nascent soot to more mature soot. In the central part of the flame, at a height of 10 mm above the burner, the temperatures and the soot particle sizes were found to be nearly constant.

Populärvetenskaplig sammanfattning

Mer än 75 % av energianvändningen i världen kommer idag från förbränning av fossila bränslen, biobränslen och avfall. Trots att alternativa energikällor är på framfart kommer förbränning stå för den största andelen av världens energianvändning även de kommande decennierna. Tyvärr medför förbränning flera negativa konsekvenser, såsom ökad koldioxidhalt i atmosfären och utsläpp av olika slags hälsofarliga mikroskopiska partiklar. Därför är det viktigt utveckla metoder för att rena utsläppen och förbättra effektiviteten i de förbränningsprocesser som används.

Sotpartiklar bildas vid förbränning då det finns ett tillräckligt stort överskott på bränsle i förhållande till mängden syre. I vissa fall förbränns dessa partiklar senare i samma förbränningsprocess, och i andra följer partiklarna med avgaserna ut i atmosfären. Ett problem med det senare är att cancerogena molekyler sitter på sotpartiklarnas ytor. Om man andas in sotpartiklarna så kan de följa med luftströmmen ner i lungorna och de minsta partiklarna kan därifrån ta sig vidare in i kroppen. När sotpartiklarna släpps ut i atmosfären påverkar de dessutom jordens strålningsbalans och därmed klimatet, genom att de mycket effektivt absorberar solljus. Det är även intressant att veta var och när sot bildas i själva förbränningsprocessen. Eftersom motorer, gasturbiner, värmekraftverk och andra apparater baserade på förbränning redan har utvecklats under mer än hundra år så är avancerade verktyg och kunskap om hur förbränningen sker till stor hjälp för att processerna ska kunna förbättras ytterligare. Sotpartiklarna är en del i den komplicerade förbränningsprocessen och påverkar hur effektiv till exempel en motor är och vilka utsläpp som sker. I alla dessa fall är det viktigt att ha kunskap om sotpartiklarnas egenskaper för att kunna förstå och beräkna vilken inverkan de har i olika miljöer.

I det dagliga livet kan vi se sotpartiklar till exempel när vi tänder ett stearinljus eller vid en lägereld. Det gulorangea ljuset och värmen kommer från de glödheta mikroskopiska sotpartiklarna. Vi kan inte se de enskilda partiklarna eftersom de är mycket små, omkring 1000 gånger mindre än tjockleken av ett hårstrå. Anledningen till att sotpartiklarna lyser och utstrålar så mycket värme

är att de har en så hög temperatur, ca 1000–1500 °C. Vid rumstemperatur är sotpartiklarna däremot svarta. Det kan vi se om vi fångar in sotpartiklar på ett metallföremål genom att sticka in det en kort tid i flamman.

En laser kan användas för att mäta på sotpartiklarna direkt i förbränningsprocessen. Laserljus i mycket korta pulser sänds in i förbränningsgasen och hettar upp sotpartiklarna så att de blir mycket varmare än omgivningen, ofta över 3000 °C. Då lyser de mycket starkare än de omgivande partiklarna som inte träffats av laserpulsen. Med hjälp av noggranna detektorer eller kameror kan ljuset, eller *signalen*, från dessa sotpartiklar mätas och användas för att ta fram var sotpartiklarna fanns, men även koncentrationer och partikelstorlekar. För att räkna ut dessa värden från signalen så behövs en avancerad fysikalisk datormodell av mätprocessen. I allmänhet är det dock en bra uppskattning att en högre koncentration av partiklar leder till en starkare signal och att mindre partiklar ger en signal som avtar snabbare. De upphettade sotpartiklarna svalnar av på mindre än 0,000001 sekund så avancerad utrustning krävs för att kunna mäta signalen under denna tid. Metoden som just beskrivits kallas laserinducerad inkandescens, LII, och är en av de mest avancerade metoderna för att beröringsfritt mäta egenskaper hos sotpartiklar, dvs mäta utan att föra in något instrument i gasen och därmed störa förbränningsprocessen. LII kan även användas för att mäta sotkoncentrationer och partikelstorlekar i avgaser.

I denna avhandling har mättekniken LII undersökts och utvecklats och även använts för att undersöka sotpartiklarna i olika laboratorieflammor. Utvecklingen har skett genom att använda avancerade lasrar med noggranna detektionssystem, tillsammans med stabila laboratorieflammor. LII-signalerna har sedan undersökts med en datormodell av mätningen för att ta reda på hur LII påverkas av förändringar i olika parametervärden. En stor del av avhandlingen har också ägnats åt att undersöka hur LII påverkas av *aggregerade* sotpartiklar. Aggregering sker genom att mindre, sfäriska sotpartiklar slår sig samman och bildar stora, förgrenade kluster. Varje kluster har en slumpmässig form och i varje liten volym i en flamma finns ofta ett enormt antal kluster med varierande storlek. Det är en utmaning att kunna utgå från ljuset som detekteras då LII används och dra slutsatser om sotaggregatens egenskaper. I denna avhandling har sotaggregat konstruerats numeriskt i en dator och dess egenskaper med avseende på LII har undersökts genom att simulera de fysikaliska processerna hos mätningen. Denna avhandling bidrar med kunskap som kan användas för att vidareutveckla LII för att mäta på aggregerade sotpartiklar.

List of Papers

I. Henrik Bladh, Jonathan Johnsson and Per-Erik Bengtsson. "On the dependence of the laser-induced incandescence (LII) signal on soot volume fraction for variations in particle size", Applied Physics B: Lasers and Optics, 90(1), 109–125, 2008

II. Henrik Bladh, Jonathan Johnsson and Per-Erik Bengtsson. "Influence of spatial laser energy distribution on evaluated soot particle sizes using two-colour laser-induced incandescence in a flat premixed ethylene/air flame", Applied Physics B: Lasers and Optics, 96(4), 645–656, 2009

III. Jonathan Johnsson, Henrik Bladh and Per-Erik Bengtsson. "On the influence of bimodal size distributions in particle sizing using laser-induced incandescence", Applied Physics B: Lasers and Optics, 99(4), 817–823, 2010

IV. Henrik Bladh, Jonathan Johnsson, N.-E Olofsson, A. Bohlin and Per-Erik Bengtsson "Optical soot characterization using two-color laser-induced incandescence (2C-LII) in the soot growth region of a premixed flat flame", Proceedings of the Combustion Institute, 33, 641–648, 2011

V. Henrik Bladh, Jonathan Johnsson, Jenny Rissler, Hussam Abdulhamid, Nils-Erik Olofsson, Mehri Sanati, Joakim Pagels and Per-Erik Bengtsson. "Influence of soot particle aggregation on time-resolved laser-induced incandescence signals", Applied Physics B: Lasers and Optics, 104(2), 331–341, 2011

VI. Nils-Erik Olofsson, Henrik Bladh, Alexis Bohlin, Jonathan Johnsson and Per-Erik Bengtsson. "Are sooting premixed porous-plug burner flames one-dimensional? A laser-based experimental investigation", Combustion Science and Technology, DOI: 10.1080/00102202.2012.718006, 2012

VII. Jonathan Johnsson, Henrik Bladh, Nils-Erik Olofsson and Per-Erik Bengtsson. "Influence of soot aggregate structure on particle sizing using laser-induced incandescence: Importance of bridging between primary particles", submitted to Applied Physics B, 2012

Related Work

I. Edouard Berrocal, Jonathan Johnsson, Elias Kristensson and Marcus Aldén. "Single scattering detection in turbid media using single-phase structured illumination filtering", Journal of the European Optical Society Rapid Publications, 7, 12015, 2012.

Contents

Chapter 1

Introduction

Humans have been using fire as a tool for millennia and it has been known how to control fire for hundreds of thousands of years [1]. In the last two hundred years, combustion processes have played an important role in industrialisation. Although the basic knowledge of how to use combustion as a tool has been around for a long time, there is still much to be learned with regard to details of the combustion processes. The knowledge acquired can be used to improve combustion efficiency and reduce emissions.

The use of fossil fuels has steadily increased and accounts for over 80 % of the total primary energy supply in the world [2]. The large amounts of emissions from combustion have become a cause for climatic concerns [3]. Soot particles are included in these emissions and have been shown to have a significant effect on the climate [3, Sections 2.4.4.3 and 2.5.4]. There are also health issues in connection with airborne soot particles, carcinogenic hydrocarbons being found on the surfaces of these particles. Smaller soot particles in particular can easily follow the air taken into the lungs, where carcinogenic molecules can then enter the blood stream [4, 5].

The major aim of the thesis is to develop and test a measurement technique termed laser-induced incandescence, LII. This technique can be used to determine soot particle sizes and soot volume fractions (volume of soot particles/total volume) for soot suspended in a gas, both in combustion processes and in exhaust gases, without this disturbing the processes involved. The soot properties are found by using laser light to heat the particles. This induces radiation by the particles that can then be detected and assessed. The time-integrated radiation involved is approximately proportional to the soot volume fraction, which means it can be measured by use of an intensified CCD camera, enabling measurements of high spatial and temporal resolution to be obtained. Images can then be created, showing the soot distribution within a sooting environment at a specific moment in time. Although soot particle sizes can also be measured in a manner indicating their spatial distribution, limitations in ex-

perimental equipment make detailed particle size measurements rather complicated. Accordingly, time-resolved point measurements of particle size are currently employed both in measurements for applied purposes, and in measurements under controlled laboratory conditions used for developing the LII technique.

The most important areas in which measurements of soot suspended in a gas are of interest can be divided roughly into those of fundamental research, combustion process development, and research concerning climate and concerning matters of health. In fundamental research concerning development of the LII technique, the soot sources are usually simple and have well-defined properties, since theories of how the LII technique works are often involved. Apart from improving the LII technique itself, the results of such research can be of interest to scientists concerned with modelling combustion processes, such as in soot formation. In the development of combustion processes it can be of interest to know where and when the soot appears, and also the properties it possesses. Such knowledge can be used, for example, by engine designers who want to improve an engine in some way, such as through increasing its efficiency and reducing emissions.

The second chapter of the thesis describes the properties of soot that are relevant for LII measurements. In the third chapter, the basics of LII and of various other methods for measuring properties of soot are described. The fourth chapter concerns how the current LII system for soot particle measurements is designed. The fifth chapter deals with how particle sizes can be determined by use of the LII model, and the evaluation routines that are employed. Chapter six discusses the properties of aggregated soot particles and how aggregation can be taken into account when LII is used for particle sizing. Chapter seven takes up various of the results of the papers included in the thesis, together with certain unpublished results. Chapter eight, finally, provides a short summary and an outlook.

Chapter 2

Soot in Combustion Processes

A combustion process can be described as an exothermic chemical reaction between a fuel and an oxidiser. Usually the fuel is a carbon-based solid, liquid or gas and the oxidiser is usually either oxygen or air. In the LII community, one of the most highly investigated combustion processes in laboratory measurements is the burning of ethylene (also called ethene, C_2H_4) in air. In the text that follows, the combustion of ethylene in air is described; for detailed descriptions of combustion and soot formation generally, see e.g. [6–10].

An ideal form of the combustion of ethylene by oxygen is one described by the chemical formula

$$1C_2H_4 + 3O_2 \rightarrow 2CO_2 + 2H_2O. \tag{2.1}$$

Ideal refers here to the fact that the only product gases are carbon dioxide and water. In reality, other species are always present in the product gases too, due to the effects of chemical equilibrium. The actual chemical reaction involves the production and interaction of a large number of intermediate species. What thus occurs can be imagined as being processes that are hidden within the arrow in the formula. The reactions of these intermediate species eventually lead to the product species, consisting mainly of carbon dioxide and water, although it also includes small amounts of other species.

The combustion reaction (2.1) is termed *complete* or *stoichiometric* because the fuel/air ratio is chosen so that it would only produce carbon dioxide and water, with no excess atoms or molecules of different kinds, if an ideal combustion were possible. Even if the reaction (2.1) is simply an idealised model of a real chemical process, it is a good indicator of the main results of the complete combustion of ethylene in air.

There are two commonly used definitions for describing the fuel/oxidiser ratio: the equivalence ratio, Φ, and the carbon/oxygen (C/O) ratio. The definition of the former is

$$\Phi = \frac{\left(n_{\text{fuel}}/n_{\text{oxidiser}}\right)_{\text{actual mixture}}}{\left(n_{\text{fuel}}/n_{\text{oxidiser}}\right)_{\text{stoich. mixture}}}, \tag{2.2}$$

where n_i represents the number of moles of each species. By definition, a stoichiometric reaction, such as (2.1), has an equivalence ratio of $\Phi = 1$. If $\Phi < 1$, the combustion process is *lean*; if $\Phi > 1$, it is *rich*. The C/O ratio is defined simply as

$$\frac{n_{\text{C}}}{n_{\text{O}}}, \tag{2.3}$$

where n_{C} and n_{O} stand for the number of moles of carbon and of oxygen atoms, respectively. For the reaction (2.1), the C/O ratio is

$$\frac{n_{\text{C}}}{n_{\text{O}}} = \frac{2}{6} \approx 0.33. \tag{2.4}$$

2.1 Soot Formation

If the fuel/oxygen ratio in the reaction (2.1) is increased, the amount of oxygen will not be sufficient to completely burn the ethylene to carbon dioxide and water. Carbon monoxide, CO, and hydrogen, H_2, will then be present in the product gases. If the fuel/oxygen ratio is further increased, the carbon/air (C/O) ratio will eventually become larger than one, meaning that even if all of the oxygen atoms have been used to create carbon monoxide, there is an excess in the amount of carbon that remains. Soot particles are formed from such excess amounts of carbon (hydrogen also being present in the particles). When the C/O ratio is close to one, the simplified global reaction for combustion of ethylene by oxygen can be described by

$$C_2H_4 + x\,O_2 \rightarrow 2\,x\,CO + 2H_2 + (2 - 2\,x)C_S, \tag{2.5}$$

where it is assumed that no H_2O or CO_2 are formed. This simplified reaction predicts that, if $x < 1$, carbon, C_S, for creating soot particles will be available.

In experiments, soot is usually formed for C/O ratios of less than one. Soot starts to form in the C/O-ratio range 0.5–0.8 [10]. Where within this range the value of the ratio lies depends upon the fuel composition and the way the fuel burns. The difference between theory and experiment evident here is due to the formula above being too simple to describe the combustion process accurately. A more detailed analysis shows that there are always certain amounts of CO_2 and H_2O present in the resulting species, due to chemical equilibrium

between the species involved. This leads to less oxygen being available for creating CO, which results in soot formation occurring at a lower C/O ratio than would be the case otherwise.

As already indicated, a combustion reaction, including that of soot formation, is not a one-step process. It usually consists of a large number of intermediate steps, the fuel first being decomposed into smaller molecules, some of them highly reactive and unstable, which then react and finally form the product species.

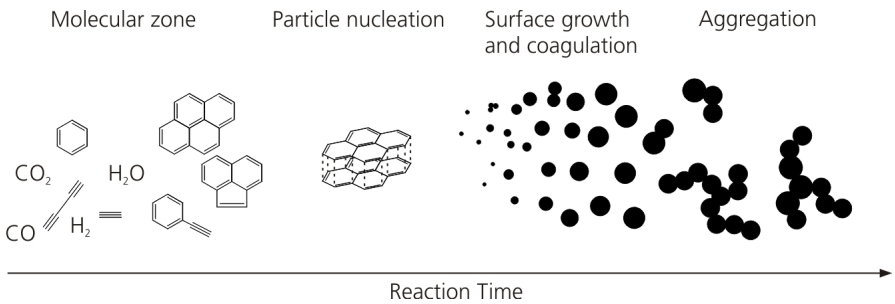

Figure 2.1: A schematic visualization of soot formation. The building blocks of soot are believed to be primarily polyaromatic hydrocarbons and acetylene. These molecules stick together and form the nuclei of the soot particles, which in turn grow through surface growth and coagulation. If the particle density is sufficiently high, the soot particles can stick together and form soot aggregates at the end of their growth process.

The formation of soot particles can be divided into three main processes: particle inception, growth and aggregation; see Fig. 2.1. The processes of soot formation are not generally separated completely, there rather being a smooth transition from one process to the next. Before soot particles start to form, the fuel is broken down from (what are usually) larger hydrocarbons to smaller molecules. This is called *pyrolysis*. The very first soot particles are believed to be formed out of polyaromatic hydrocarbons, PAHs, and different unsaturated hydrocarbons such as acetylene. A detailed description of the particle inception process is still a subject of research [11, 12]. The nucleated (<2 nm) soot particles grow when hydrocarbons react with active sites on the surfaces

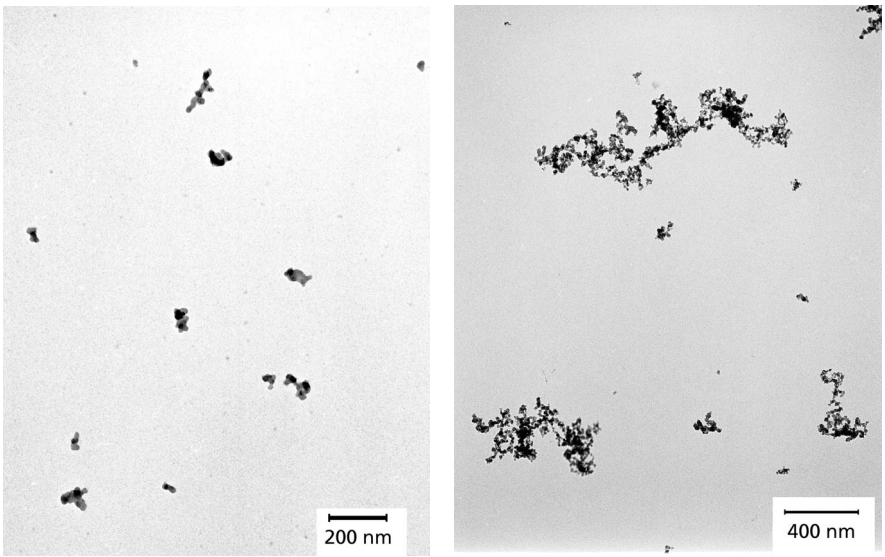

Figure 2.2: TEM images, the scale on the left differing from that on the right. **Left:** Soot particles as produced by a flat flame on a McKenna burner, as described in Section 2.3.1. **Right:** Soot particles from the soot generator described in Section 2.3.3.

of the particles, although they also grow by coagulation, the particles sticking together to form larger particles. The surface growth increases the soot volume fraction, while it is kept constant during the coagulation. The particles can also grow by aggregation, through sticking together to form fractal-like structures. It can be seen that there can be a thick connection between primary particles which we call *bridging*. This is most probably caused by the surface growth continuing also some time after the aggregation has occurred. The influence of bridging on LII is investigated in Paper VII and is also described briefly in Chapter 6.

If the number density is sufficiently large, the aggregated particles can become entangled to form agglomerates. The soot particles can oxidise in any of the growth steps described above, provided such oxidisers as O_2 or OH radicals are present, and in some cases they oxidise the soot particles completely, so that no soot at all is present in the exhaust gases. In Fig. 2.2 two transmission electron microscopy (TEM) images, that contain soot particles sampled under differing conditions are shown.

Since the building blocks of the soot particles are hydrocarbons, there is always a certain amount of hydrogen present in soot particles. As the particles grow, the hydrogen content decreases [10].

2.2 Soot Properties

The soot properties of relevance to LII measurements are those that affect the internal energy of the particles and the rate of energy transfer into and out of the soot particles during measurement. The energy transfer is brought about mainly by radiation, heat conduction and loss of mass. In using LII, the particles are heated by a laser pulse, this representing the main energy transfer into the particles. The amount of energy transferred depends upon the characteristics of the laser pulse, as discussed in Section 3.1.3, and upon the optical properties of the particles. The absorption of energy leads to an increase in the temperature of the particle, which depends on its specific heat capacity and mass. If the incident laser fluence (J/cm^2 per laser pulse) is sufficiently high, the mass of the affected particles decreases through sublimation. The major energy loss processes are sublimation and heat conduction to the surrounding gas, which means that the heat of sublimation of soot and the heat transfer coefficients are important when using LII.

The rate of change of the internal energy of a soot particle is dependent upon the density, volume, and heat capacity of the particle. In the LII model used in the present work, it is assumed that the density of soot slowly decreases with an increase in temperature, whereas the specific heat capacity increases when the temperature rises [13]. The temperature dependence of the density means that, if there is no mass loss, the diameter of the particle increases slowly with an increase in temperature. The property of a soot particle describing its ability to exchange heat with the gas surrounding it is termed the thermal accommodation coefficient. The size of the coefficient depends upon the composition of the gas and of the particle surface. Sublimation of the particle is dependent upon the surface area of the particle, the heat of sublimation and the molecular flux of the sublimated carbon. The sublimation of soot starts to becomes significant at temperatures above ~3600 K [13].

In the previous section, the shape of the soot particles was mentioned briefly. Soot particles can be almost spherical, but can also stick together to form large fractal aggregates. The building blocks of these aggregates are termed *primary particles*. When the primary particles stick together to form aggregate particles, they shield each other, resulting in an effective decrease in the surface area of each primary particle. If correction factors that take shielding effects into

account are used in LII particle size evaluation, this means that it is the diameters of the primary particles that are measured, rather than the diameter of the aggregate. In the present work, LII particle size evaluation is first described, in Chapter 5, under the assumption of no aggregation being present. The aggregate structure and its effect on LII particle sizing is then discussed in detail in Chapter 6. The effects of aggregation are the main theme in Papers V and VII.

The thermal radiation from soot particles is a physical process that has no more than a negligible effect on the energy transfer that takes place during the LII process, though it still is highly relevant. This radiation is detected so as to obtain the LII signal, which contains the information used to evaluate the soot volume fractions and particle sizes. The absorption and thermal radiation of soot particles is dependent upon their optical properties.

2.2.1 Optical Properties and Thermal Radiation

The optical properties of soot can be used to describe what happens when light interacts with a soot particle, such as how much of the light is absorbed, transmitted or scattered. Also, the thermal radiation from the particles depends upon optical properties of the particles.

The simplest model of a soot particle, with regard to its optical properties, is a homogeneous sphere with the (relative) complex refractive index m,

$$m = n + ik, \tag{2.6}$$

where n is the refractive index of the particle, which is related to the phase velocity in the medium ($n = c/v_{\text{phase}}$, where c is the speed of light in a vacuum and v_{phase} is the phase velocity within the particle), and k is a measure of the particle's absorption. Generally, both n and k depend upon the wavelength of the incident light, λ, so that $m = m(\lambda)$. For soot, this dependence upon the wavelength has been shown to be relatively small, as discussed in Schulz et al. [14], for example. According to Krishnan et al. [15, 16], the dependence of the complex refractive index of soot upon the type of fuel involved is very slight.

The complex refractive index is of interest not only for LII but also for scattering measurements. There have been a number of papers published in which it has been measured; see e.g. [15, 17]. It is difficult to determine the complex refractive index of soot with a high degree of accuracy, however, since it depends upon the environment in which the soot was formed. Thus, the values determined by different groups vary rather markedly. Different values have been obtained and been used by different groups, the ns being in the range of

1.3–2.0 and the ks in the range of 0.4–0.9 [15], this resulting in very differing absorption and scattering cross sections. When a complex refractive index is selected for evaluation in a particular experiment, it is necessary to consider the different published values and use one that is applicable to the conditions that are present.

The value of m is not needed explicitly when using LII, but it is sufficient to know the value of the absorption function $E(m)$, defined as

$$E(m) = \mathrm{Im}\left(\frac{m^2 - 1}{m^2 + 2}\right). \tag{2.7}$$

This has led to publications, such as Snelling et al. [18], in which $E(m)$ has been determined directly, without any knowledge of m. Unfortunately, here too the results of different measurements differ rather markedly, making it difficult to determine which value is the most appropriate one to use in a given experiment. The values of $E(m)$ reported in the literature indicate that the function changes slowly with wavelength, and that its values are in the approximate range of 0.2–0.4 within the wavelength interval of 350–700 nm [15,16]. Because of the problems involved in determining m and $E(m)$, LII evaluation procedures have been invented in which the effects these parameters have on the results is minimised. One such procedure is the two-colour LII technique, described in Section 5. In Paper IV, we investigated the value of $E(m)$ in the flat flame on a McKenna burner, one of the most important findings there being strong indications of $E(m)$ increasing with the height above the burner.

The thermal spectral radiance, I, of a soot particle at the wavelength λ can be described by the blackbody radiation expression, multiplied with the emissivity of soot, $\varepsilon(d_\mathrm{p}, \lambda)$,

$$I(d_\mathrm{p}, \lambda, T) = \varepsilon(d_\mathrm{p}, \lambda) \frac{2\pi h c^2}{\lambda^5 \left(\exp\left(\frac{hc}{\lambda k_\mathrm{B} T}\right) - 1\right)}, \tag{2.8}$$

where T is the absolute temperature of the particle, h is the Planck constant and k_B is the Boltzmann constant. The emissivity is generally in the range of $0 \leq \varepsilon \leq 1$. In this case it can be approximated by the expression for emission from a spherical particle in the Rayleigh regime* [19] ($d_\mathrm{p} \ll \lambda$),

*The Rayleigh regime expression is only a good approximation for wavelengths much larger than the particle diameter, a condition that is not fulfilled for the spectrum in its entirety. The shape of the soot blackbody function is still quite accurate, however, when this expression is used for the emissivity. It is the shape which is important in evaluating the particle

$$\varepsilon(d_\mathrm{p},\lambda) = \frac{4\pi d_\mathrm{p} E(m(\lambda))}{\lambda}. \tag{2.9}$$

Since the emissivity for soot is less than one, Eq. (2.8) is sometimes described as concerning *greybody* radiation. Examples of the greybody radiation described here, for soot particles of different temperatures, is shown in Fig. 2.3.

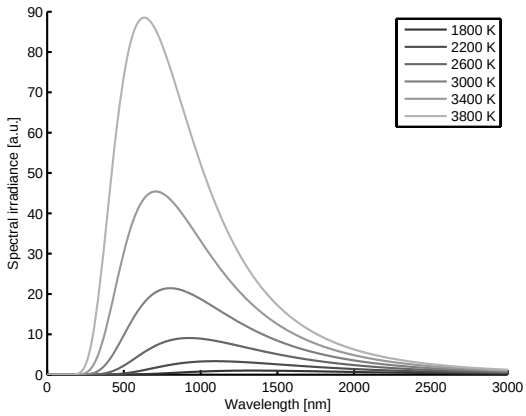

Figure 2.3: Soot greybody radiation at different temperatures. The flame temperatures are at around 1800 K, whereas in LII measurements the soot can have peak temperatures as high as 4000 K.

The radiation profile shown in Fig. 2.3 can be used to determine the temperature of a soot particle on the basis of its radiation, a technique termed *pyrometry*. There are different ways to carry out pyrometry, in this work the two-wavelength method being employed. Detecting the greybody radiation at two different wavelengths enables the temperature to be calculated. How this is carried out is described in detail in Chapter 5.

If $E(m)$ is assumed to be independent of the wavelength, the total irradiation from a soot particle can be found by integrating Eq. (2.8) over all the respective wavelengths with the emissivity obtained using Eq. (2.9), and multiplying this with the geometrical cross section, $\pi d_\mathrm{p}^2/4$. This yields [13]

temperature on the basis of the particle's radiation, using two-colour pyrometry, which is an important part of the particle size evaluation process described in Chapter 5.

$$\dot{Q}_{\mathrm{rad}} \approx \frac{199\pi^3 d_{\mathrm{p}}^3 (k_{\mathrm{B}} T)^5 E(m)}{h(hc)^3}, \tag{2.10}$$

where it can be seen that the power radiating from the particle is proportional both to the volume of the particle and to T^5.

2.3 Laboratory Soot Sources

One of the major aims in the development of LII has been to make it possible to measure soot properties in applied environments, such as within internal combustion engines and gas turbines. These sooty environments are complex and not suited for use as reference sources during development of the technique. To simplify the development of LII, soot sources are used which are easier to control and that provide better optical access. These soot sources are usually designed to be stable, and have specifications making them suitable for LII measurements. The following soot sources have been employed in the present work, their being only a few examples of the soot sources used within the LII community.

2.3.1 McKenna Burner

One burner commonly used in LII development is the McKenna burner, Fig. 2.4. It is a porous-plug burner used to produce premixed, stable flat flames. It is currently manufactured by Holthuis & Associates* (previously McKenna Products). There are different types of McKenna burners. The one described here is the bronze porous plug burner used in Papers II, IV and VI. This burner has a central sintered porous plug with a diameter of 60 mm and an outer porous ring having an outer diameter of 88 mm. The premixed fuel and the oxidiser gas flow through the central plug, whereas the outer ring can be used for a stabilising co-flow, employing either combustible gas, inert gas or air. To stabilise the flame, a cylindrical stainless steel plate with a diameter of 60 mm is centred above the burner. Since the porous plug is heated by the flame, it needs to be cooled to avoid damage to it. This is done by means of water that flows through a coiled metal pipe inside the plug.

One important feature of the McKenna burner flame is that it is one-dimensional, in the sense that the flame properties are essentially the same at

*Address: Sebastopol, California, USA
URL: http://www.flatflame.com

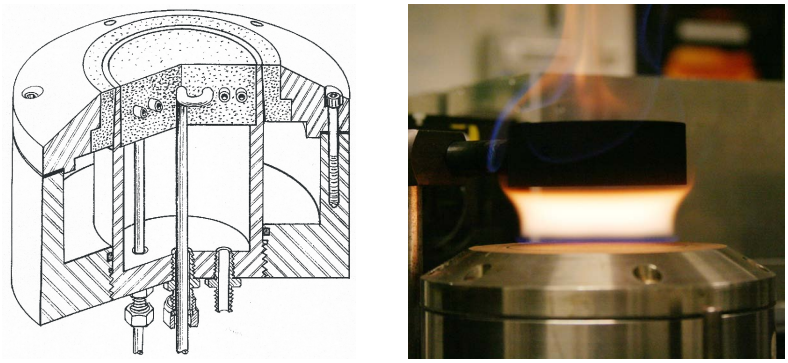

Figure 2.4: Left: Design of the McKenna burner. **Right:** A McKenna burner with an ethylene/air flame, stabilised by a nitrogen co-flow and a steel plate.

all positions at a certain height above the burner, as long as one is not too close to the edges of the flame [20]. Different heights thus represent soot in different phases of growth, coagulation and aggregation, so that the vertical axis through the flame can be thought of as a time axis. Thus, the McKenna burner has properties favourable to studying soot particles of different age and size. It should be noted, however, that there has been some discussion of how one-dimensional the flame actually is [21].

The properties of soot particles along the centre axis in a McKenna flame is investigated in Paper IV. In Paper VI we investigate the one-dimensionality of the bronze McKenna burner mentioned above. Here, the effects of different stabilising co-flows are also tested. Summaries of the Papers IV and VI can be found in Section 7.2.

Comparing results obtained from experimental setups of different research groups is much easier if important parameters, such as those of the burner, are the same. In line with this, the McKenna burner has been proposed as the standard flat-flame burner in to be used the LII community. (The Gülder burner and the Santoro burner have been proposed as standards for diffusion flames, but since they have not been used in the work presented here, they will not be discussed further.) Even when it is specified that the McKenna burner is used, there are a number of parameters that can be changed which can affect the flame properties. Such parameters include the following: the type of porous plug employed (stainless steel or bronze); the shape, material and position of the flame stabiliser; the type of combustible gas, oxidiser and shielding gas employed; the total volume flow of the combustible gas mixture and of the

shielding gas; and the equivalence ratio. The parameters our group is currently investigating the use of as standard conditions for the McKenna burner are shown in Table 2.1.

Table 2.1: Parameters that our group is currently investigating the use of as standard conditions for the McKenna burner.

Porous plug material	bronze
Combustible gas mixture	ethylene (C_2H_4) and air
Combustible gas flow	10 slm (1 atm, 0 °C)
Co-flow	N_2 or air, same velocity as the combustible gas
Stabiliser	Stainless steel plate
Height of stabiliser	21 mm above burner surface

2.3.2 Carbon Black Distributor

In a master thesis project [22], the time-resolved LII technique was used to measure the sizes of soot particle samples employed in the carbon black industry. Carbon blacks are soot particles that are produced industrially for use in tires, rubber and plastic products and in printing inks. Eight million metric tons are produced in the world each year, placing it in the top 50 of industrially manufactured chemicals [23]. The industry produces carbon black having different properties, such as different surface areas and sizes. Since the particle properties are determined using methods that cannot be used online in the production of carbon black, it is of interest to create an online measurement system, so as to better be able to control production.

The carbon black distributor was designed by Nils Hernäng during his master thesis project and was manufactured at Orion Engineered Carbons (URL: http://www.orioncarbons.com/). The distributor, shown in Fig. 2.5, makes it possible to whirl the carbon black powder into the measurement volume of the LII setup. The main part of the construction is a closed-loop stainless-steel pipe in which air can be circulated by means of an electric fan. The pipe has two holes, the one intended for use in injecting soot into the closed loop, and the other intended for use in extracting soot from the loop. The inlet and the outlet can be closed by use of cork plugs.

Figure 2.5: The carbon black soot distributor.

A typical measurement using the distributor starts by injecting a small amount of carbon black into the inlet of the running distributor. The outlet is then opened and soot is blown out into the measurement volume of the LII setup. The flow out from the distributor can be controlled by using different outlet extenders of differing diameter. Preliminary measurements we have made using the distributor [22] suggest it to produce a reasonably steady flow of particles.

2.3.3 Flame-based Soot Generator

We have investigated a flame-based soot generator built by Hussam Abdulhamid and Mehri Sanati, at the Division of Ergonomics and Aerosol Technology, Lund University, one having a design partly based on suggestions and feedback from our group. The soot is generated by a rich diffusion flame on top of a cylindrical burner which is mounted in a T-pipe construction, Fig. 2.6. The tip of the flame is quenched using a cold cross flow of nitrogen or air that cools the gas effectively, preventing further soot formation and oxidation. At the end of the quenching pipe, the soot volume fraction can be reduced by dilution using nitrogen or air. The height of the flame can be adjusted so that the tip is quenched at different heights. Since the soot particle size distribu-

tions varies with the height in the flame, this means that the distributions that are generated can be varied. The soot size distribution which is produced is monitored using a scanning mobility particle sizer, SMPS, that measures the mobility diameter of the particles. Monitoring can be employed to ensure that the size distribution of the particles produced by the soot generator is stable.

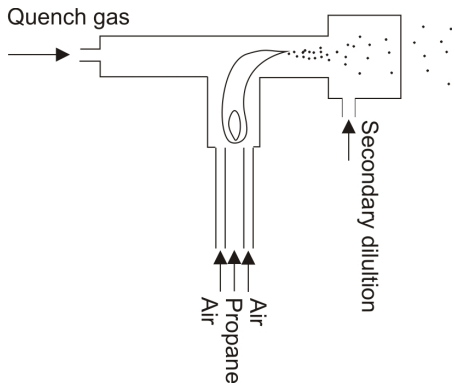

Figure 2.6: The Ergonomics and Aerosol Technology soot generator.

Chapter 3

Soot Diagnostic Techniques

A number of diagnostic techniques have been employed in the thesis. These techniques are described in the present chapter, concerned mainly with the general properties of laser-induced incandescence, the main technique used in the work presented here.

3.1 Laser-Induced Incandescence

Laser-induced incandescence (LII) is a laser-based diagnostic technique for measuring soot volume fractions and particle sizes in combustion applications, both during the combustion process and in the exhaust gases produced. The technique was proposed and described already in the 1970s by Weeks and Duley [24] and by Eckbreth [25], but has been mostly used and developed during the last 15 years. In the mid 1990s, the first demonstrations were made showing that the time-resolved LII signal can be used for particle sizing [26,27], the LII particle sizes being shown to correlate with sizes as determined by transmission electron microscopy, TEM [28]. Following these developments, studies on the effects of aggregation on LII particle sizing were carried out. Because both the model and the theory of aggregation are relatively complicated, however, these will not be discussed here but in Chapter 6.

The common use of LII for soot diagnostics involves employing a short laser pulse to heat soot particles suspended in a gas, and use of the enhanced thermal radiation (the LII signal) from the particles to determine the sizes or the volume fraction of the particles. Two examples of (modelled) LII signal are shown in Fig. 3.1.

LII shares many of the advantages and disadvantages of laser-based techniques generally. On the positive side, LII is essentially non-intrusive, so that it does not interfere appreciably with the combustion process, and enables measurements of high temporal and spatial resolution to be obtained. On the neg-

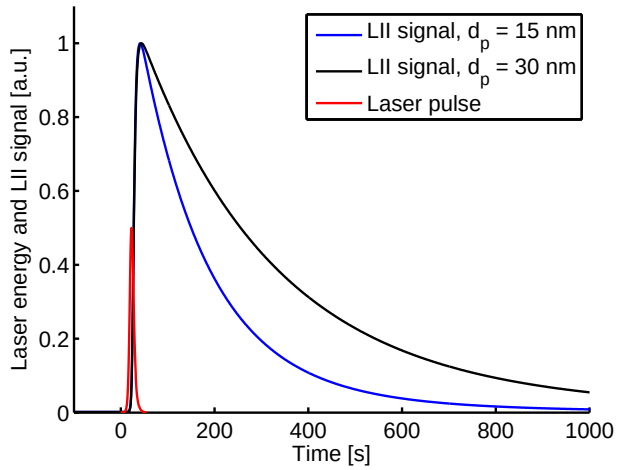

Figure 3.1: Examples of LII signals resulting from a laser pulse (modelled data). Note that smaller particles lead to shorter decay times for the LII signal.

ative side, optical access to the region of interest is required, which in some cases limits the applicability of the technique. Also, the equipment required is relatively expensive, the operator also needing to know how to set up the equipment in such a way as to maximise the quality of the measurements and evaluations. In addition, for particle sizing a theoretical model is needed.

Soot volume fraction measurements are usually made using imaging, by a camera that records the time-integrated LII signals. The soot volume fraction, f_v, is defined as

$$f_v = NV_p = N\frac{\pi d_p^3}{6}, \tag{3.1}$$

where N is the number density of the particles, V_p is the volume of a particle and d_p is its diameter.

Melton [29] showed that the time-integrated LII signal, S, is related to d_p as

$$S \propto d_p^x, \tag{3.2}$$

where

$$x = 3 + \frac{0.154 \cdot 10^{-6}}{\lambda}, \tag{3.3}$$

λ being the detection wavelength (in metres). This expression was derived at the limit of high laser power and high particle temperature. If the approximation is made that $x \approx 3$, Eq. (3.1) and Eq. (3.2) show that the signal can be considered directly proportional to the soot volume fraction,

$$S \propto f_v, \tag{3.4}$$

This expression enables simple imaging measurements of soot volume fractions to be obtained and has since then been used frequently in both laboratory and applied environments, see e.g. [30–32]. Because of the LII models having evolved since Melton's calculations in 1984, one of the things that was tested in Paper I here was the proportionality statement that Eq. (3.2) represents, seeing how well the relation holds with use of the current LII models.

In determining particle sizes, the LII signal needs to be detected with time resolution, the results being better if the time resolution is sufficiently good for faithful reproduction of the signal. Time resolution is needed here since the decay of the LII signal provides information concerning the particle size: the time-decay of the temperature being faster for smaller particles, and the LII signal being stronger for higher particle temperatures. Since high time resolution is desired here, development of the LII technique for particle sizing is carried out mainly by use of point-measurements, for which photomultipliers or fast photodiodes are employed.

3.1.1 A Brief Description of an LII Measurement

The following is a general account of what happens during an LII measurement.

1. A laser emits a light pulse that is partly absorbed by the soot particles to be investigated. The pulse may pass through various optical components before it reaches the soot particles.

2. The temperature of the soot particles increases due to the absorption of laser light. The magnitude of the increase depends on the local fluence (J/cm^2 per pulse) of the laser pulse, which affects the particles, and also on the physical properties of the soot and of the ambient gas. Because of the higher temperature, the particles radiate more strongly. This increase in radiation is termed the LII signal.

3. After being heated, the soot particles cool, due to a number of physical processes that take place. The rate of the cooling is dependent upon such ambient conditions as gas temperature, mixture and pressure, as well as

upon the properties of the particles. As the temperature drops, so does the thermal radiation from the particles.

4. The increased thermal radiation from the laser-heated particles (the LII signal) can be detected, for example by use of a photomultiplier or an ICCD camera. If the time decay of the signal is resolved, information concerning particle sizes can be obtained.

5. Finding the particle sizes on the basis of the signal produced involves comparisons between the experimental signal and signals generated by an LII model. The model endeavours to reproduce the experiment as accurately as possible, making use of a description of the setup and of the different physical properties and processes involved. Varying the particle sizes in the model and comparing the resulting modelled signal with the experimental signal enables a best match to be found. The approximate expression obtained from Eq. (3.4) can be used, together with calibration measurements obtained by use of a complementary technique, for obtaining soot volume fraction measurements.

A schematic diagram of an LII measurement is shown in Fig. 3.2.

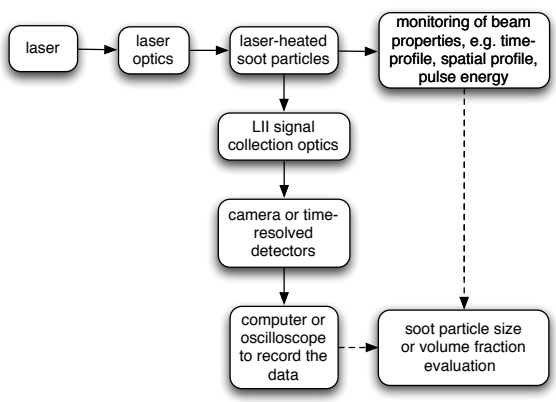

Figure 3.2: Schematic diagram of the LII setup. The extent to which the beam properties are measured depends on the type of setup involved.

3.1.2 Important LII Model Parameters

Many details of the LII model need to be taken into account in the evaluation of an LII measurement. This is especially the case when conducting particle size measurements, in which use is made of the complete LII model. The LII model is dependent, for example, on a number of different parameter values, some of which are relatively uncertain. In order to obtain a measurement with as low a level of uncertainty as possible, one should consider whether the effect of some parameters can be avoided, especially as regards those parameters having a high degree of uncertainty.

Two of the most important parameters are the absorption function, $E(m)$, and the thermal accommodation coefficient, α_T. To understand how these parameters are involved in the LII process, see Section 5.1.

The absorption function, $E(m)$, has already been described in Section 2.2.1. In conducting size measurements by use of LII, it is highly important to know the peak temperature of the particles. To do this properly with use of the model, the correct value of $E(m)$ is needed, since it affects the light absorption of the particle. To avoid the uncertainty introduced in assuming a particular value for $E(m)$, the LII signal can be detected at two wavelengths. The signals can then be used for two-colour pyrometry so as to be able to calculate a good approximation of the peak temperature of the particles without knowledge of $E(m)$. The absolute value of $E(m)$ thus need not be determined.

The thermal accommodation coefficient, α_T, describes the efficiency of the heat conduction from a particle to the ambient gas, which is due to gas molecules that collide with the particle surface. The parameter α_T is important for particle sizing, which is often carried out making use of low laser fluence measurements, in which heat conduction is the major process affecting the signal decay. Thermal accommodation coefficients that have been used in LII studies are in the range 0.07–1.0 [33].

3.1.3 Choice of Laser Wavelength

Soot particles absorb a wide spectrum of electromagnetic radiation, this having the direct consequence that a laser operating at almost any wavelength in the UV–IR spectrum could potentially be used for LII measurements. There is no need here to tune the laser wavelength to specific wavelengths, as would be required in many other laser-diagnostic techniques in which transitions in molecules are matched.

For spherical particles in the Rayleigh regime ($d_p \ll \lambda$), the absorption of light can be described by the absorption cross section [19],

$$C_{\text{abs}} = \frac{\pi^2 d_{\text{p}}^3}{\lambda} E(m), \tag{3.5}$$

where

$$E(m) = \text{Im}\left(\frac{m^2 - 1}{m^2 + 2}\right). \tag{3.6}$$

Note that the absorption cross section is directly proportional to the volume of the soot particle,

$$C_{\text{abs}} \propto \pi d_{\text{p}}^3/6, \tag{3.7}$$

meaning that a small soot particle subjected to a laser pulse having a specific fluence is always heated to the same temperature, regardless of the particle size, its being a *volume absorber*. This is an important fact that is exploited in the particle size evaluation procedure.

Since the absorption function, $E(m)$, is a slowly varying function of the wavelength, λ, it can be seen in Eq. (3.5) that the absorption cross section for a given particle size varies approximately as

$$C_{\text{abs}} \propto \frac{1}{\lambda}. \tag{3.8}$$

On the basis of this relationship alone, shorter wavelengths are to be preferred, since they result in a larger absorption cross section. There are other issues that need to be taken into account, however, such as at which wavelengths other species in the combustion process absorb, and the transmission characteristics of the optics in the setup. In a sooting flame, polyaromatic hydrocarbons, PAHs, are usually also present in the gas surrounding the soot particles, since they are precursors in the soot formation process. PAH is known to have a broadband absorption spectrum in UV, and also in regions of the visible spectrum. C_2 is also known to have interfering peaks in the visual spectrum. Although no appreciable quantities of C_2 are present in a combustion process, it can be created during the sublimation of the soot particles if the laser fluence is sufficiently high [34, 35].

Pulsed Nd:YAG lasers are popular for LII measurements since they are reliable, relatively inexpensive and are easy to work with. The second harmonic (532 nm) of these lasers has long been used, since it is visible and is therefore easy to work with. Unfortunately, it is known that there are interferences from PAH [32,36] at this wavelength, leading to uncertainties in the results of measurements. To avoid absorption from other species the fundamental (1064 nm)

of the Nd:YAG laser has become used more widely [36]. This wavelength is in the infrared portion of the spectrum, where the absorption cross section is smaller and it is more inconvenient and dangerous to work, since the light is invisible to the human eye. Since the ocular media in the eye is transparent to light with wavelengths in the range of 400–1400 nm a high-power laser pulse at 1064 nm can cause severe damage to the retina [37].

3.1.4 Nonlinear Response of the LII Signal

The response of the LII signal to laser fluence is nonlinear and depends on a number of experimental parameters, such as the laser beam profile, the ambient pressure and the particle size distribution. The nonlinearity complicates the evaluation of the LII signal. It is thus important to understand the implications of the experimental parameters on the signal. When LII is used for particle size or volume fraction measurements, the following are the basic factors that affect the nonlinear response of the LII signal to laser fluence (for complementary information, see the description of the LII model in Section 5.1):

1. Soot particles commonly have sizes within the Rayleigh regime, so that they are volume absorbers. This means that as long as the temperature is below the sublimation temperature of soot, the increase in particle temperature is approximately proportional to the laser fluence at the location of the particle. If the laser beam profile is not uniform in fluence, different particles will be heated to different temperatures, adding to the nonlinearity of the points that follow.

2. Since soot particles are essentially volume emitters, the larger particles have a much stronger effect on the LII signal than the smaller ones do, provided their temperatures are the same. Also, the cooling rates are essentially proportional to the particle surface area, and the internal energy is proportional to the particle volume. Because of their larger surface-to-volume ratio, the smaller particles cool faster than the larger ones do. Thus the relative contribution of the smaller particles to the signal decreases with time.

3. The LII signal, S, has a nonlinear dependence on the particle temperature, T, as given approximately by*

$$S \propto T^5, \tag{3.9}$$

*The LII signal is here the increased radiation from the particles integrated over all wavelengths. Usually, the LII signal is detected at specific wavelengths or through use of a low-pass filter. In these cases the relationship only provides a very rough estimate. For the wave-

(cf. Eq. (2.10)), as long as the temperature of the particle is below the sublimation temperature of soot.

4. If the laser fluence is sufficiently high, so that the particle temperature rises above the sublimation level, the relationships above become complicated. The particles lose mass then, leading to a loss in the signal produced. The peak temperature of the particles will also not increase as rapidly with increasing laser fluence above the sublimation level, because of the extra energy required for the sublimation.

The full LII model is used in the evaluation of particle size measurements, meaning that all of the physics involved is modelled, including points 1–4 above. However, since uncertainties are associated with each of the points, it is desirable to reduce their effect. In the investigation of a given experimental soot source, the only points that can be optimised are points 1 and 4. At point 1, the nonlinearity introduced by a nonuniform spatial beam profile can be reduced by use of a uniform profile. At point 4, a low laser fluence can be used to avoid the effects of sublimated particles on the signal.

For soot volume fraction measurements, it is possible to turn the nonlinearities at points 1 and 4 above into an advantage, so that the effects of pulse-to-pulse fluctuations and laser beam absorption on the signal is reduced. To understand the effects of the spatial profile of the laser beam on the time-integrated LII signal, consider first the effects of the fluence on the signal from a single soot particle. In such a case, the (time-integrated) signal increases monotonously with the laser fluence until the mass loss due to sublimation becomes so large that the increase in signal strength due to heating is completely cancelled. Above that fluence level, the LII signal decreases monotonously.

Consider now a large number of soot particles that are being heated by a laser, and that are spread out homogeneously in the beam profile. Also, define the mean fluence of the beam as its total energy divided by its area. If the spatial profile of the laser beam is completely homogeneous, the response of the signal is the same as for a single particle, although the signal amplitude is much greater. However, if the spatial profile is not homogeneous, different particles will be subjected to different fluences, resulting in different signals. The total signal response as a function of the mean fluence can then be significantly different from that in the case of a single particle. These response functions are

lengths and temperatures used in a common laboratory flame, the wavelength-specific signal looks more like it is proportional to T^{10} to T^{6} for wavelengths in the range 400–700 nm (based on Eq. (2.8)). This is because of the greybody peak becoming narrower and being displaced in the direction of the shorter wavelengths as the temperature increases.

called *fluence curves*. Fluence curves for the spatial profiles shown in Fig. 3.3 and the tophat profile, at a laser wavelength of 1064 nm, are shown in Fig. 3.4. Different particles will be in different local fluence regions for a specified mean fluence. This means that the larger contribution to the signal that particles near the peak of the single-particle fluence curve provide could possibly compensate for the loss of signals from particles that are sublimating. This is the reason why the signal can increase in the case of mean fluences that are far above the local fluence that is needed to sublimate a single particle, as can be seen for the fluence curve for the Gaussian sheet in Fig. 3.4.

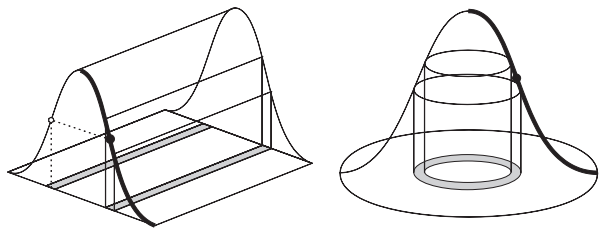

Figure 3.3: Two spatial profiles of the laser pulse that are commonly used in laser diagnostics. An approximation of the Gaussian sheet profile can be created by taking a Gaussian beam and stretch it in one direction and compress it in the other, by use of lenses. The sheet is then obtained by blocking the edges of the stretched beam. The local fluences in both these profiles varies with location in the beam.

When LII is used for volume fraction measurements, a laser profile similar to the Gaussian sheet is often employed. The camera is then placed perpendicular to the direction of beam propagation, so that the laser-heated soot particles in the centre of the beam are imaged onto its pixels. In such a case, the light that hits each pixel in the camera comes from a volume of soot that has been affected by the same (local) beam profile. If the soot volume fraction at some point in the flame is known, through some calibration measurement that has been made (such as of extinction), it is simple to calculate the average soot volume fraction for each point in the image. This is done by using the approximate expression shown in Eq. (3.4). The advantage of using the Gaussian

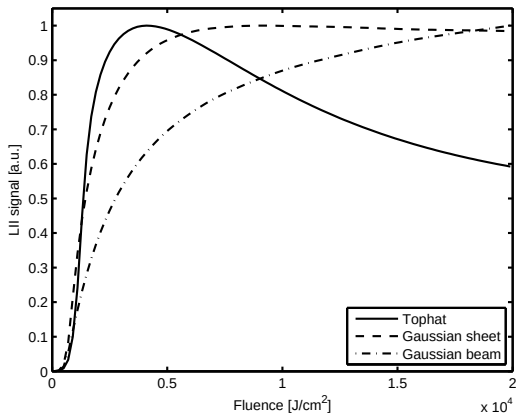

Figure 3.4: Examples of LII signal response on mean laser fluence for different types of laser spatial profiles: the tophat, the Gaussian sheet, and the Gaussian beam. These fluence curves were generated using our model, with experimental parameters set to values similar to those in Paper II, for particles with a diameter of 16 nm and a detection wavelength of 445 nm. The signal created using a prompt gate with a length of 50 ns. The curves are normalised to their peak value, and the area used for the cross section of the laser beam is defined using the $1/e^2$ criterion for the Gaussian profiles.

sheet, as opposed to any general sheet profile, is that the fluence curve above $\sim 0.3\ \mathrm{J/cm^2}$ is relatively flat. If the mean fluence on top of this plateau is selected, the signal will be relatively insensitive to fluctuations in laser pulse energy. It will also be less sensitive to absorption of the pulse energy through the measurement volume, since the fluence will remain on the plateau even if some of the pulse energy is lost.

3.2 Thermophoretic Sampling and TEM

Electron microscopes can be used to visualise samples of very small particles, much smaller than what can be resolved using an ordinary microscope. In a transmission electron microscope, TEM, electrons are first accelerated in an electrical field [38]. The electrons are then focused using electromagnetic lenses, so that they pass through the sample, after which another set of lenses is used to create an image of the sample. Because the images are created using electrons that are transmitted through the sample, the sample cannot be too thick, since it then would absorb the electrons. The potential used in accelerating the electrons is $\gtrsim 100$ kV, which results in a kinetic energy of the electrons that corresponds to a wavelength much shorter than what can be used in conventional microscopes. The short wavelength of the electrons leads to an image resolution on the order of nanometres.

To create images of soot particles using a TEM, they first need to be extracted from the flame. This is done by using a pneumatic sampling device that can insert a small copper grid into the flame, and then retract it, all within a few hundred milliseconds. The copper grid is flat and circular, having a diameter of a few millimetres, and having a thin layer of carbon on top of it. Since the grid is much cooler than the flame, the soot particles stick to the grid, due to the steep temperature gradient (a thermophoretic force).

In creating images using a TEM, it is important to set the intensity of the electron beam to an appropriate value, so that the there is adequate contrast for both the smaller and the larger particles. This can be a challenge to the experimenter if the variety of particle sizes is large. Counting and measuring the primary particle sizes within soot aggregates can also be difficult, particularly when the aggregates are dense or when it is difficult to distinguish the different particles from one another.

3.3 SMPS and DMA-APM

The scanning mobility particle sizer, SMPS, is a device that can be used to measure the particle size distribution for particles in the range of 5 nm to 1.0 μm at concentrations of between 10^6 and 10^{14} particles per cubic meter [39].

In an SMPS, the particles that enter the analyser are first filtered using an impactor, so as to remove particles larger than 10 μm that would otherwise cause problems in the evaluations. The particles are then neutralised, i.e. forced to the equilibrium charge distribution, using a charge neutraliser, before they enter the differential mobility analyser, DMA. The DMA consists of a coaxial tube that is grounded, and a central rod that has a voltage that can be controlled between levels of 20 and 10,000 V. Between the tube and the rod there is a co-axial laminar flow of air, which transports the particles from the beginning to the end of the DMA. Because of the high voltage difference between the tube and the rod, the particles move towards the rod as they pass through the DMA, at a speed that depends on their charge and on the air resistance. Near the end of the central rod, there is a small hole, used to select particles in a small size range. The number of particles that pass through the small hole are then measured using a condensation particle counter, CPC. Scanning the voltage of the central rod enables the particle size distribution of a particle stream to be measured.

When SMPS measurements are compared to LII measurements, it is important to remember that the SMPS measures the electric mobility diameter, i.e. a diameter that is related to how the particles move in air when affected by an electric field. This size can provide a measure of the total size of the particles. As has already been indicated, the diameters found by using the LII technique is related mainly to the primary particle sizes. Thus, it is easier to compare SMPS and LII data when the particles are not aggregated.

The DMA can also be used together with an aerosol particle mass analyser, APM. The output from the DMA, consisting of a single mobility diameter, is introduced to the APM that is used to determine the mass of the particles. The APM consists of two concentric cylinders that rotate at the same angular speed. The particles of interest are introduced in one end of the cylinder. A voltage is then applied over the two cylinders and only particles for which the centrifugal force is equal to the electrical force can pass between the cylinders. The particles are then counted by a CPC.

The SMPS and the DMA-APM systems were used in Paper V, together with LII measurements, to characterize the soot aggregates produced by the flame-based soot generator presented in Section 2.3.3.

Chapter 4

Experimental Setup for Two-Colour LII

The following is a description of the experimental setup for two-colour LII for soot particle sizing used in the work presented in Paper II. The setup, shown in Fig. 4.1, was designed to make it possible to make accurate LII measurements in laboratory sources of soot. It is also flexible and well-controlled, so that it is easy to change the size of the laser beam and of the measurement volume (in the centre of the flame), for example, without changing other properties appreciably, such as the type of beam profile employed.

In Fig. 4.1, two types of imaging are involved: relay imaging using two lenses, and imaging using one lens; an example of each being shown in Fig. 4.2. The relay imaging variant is used from the diaphragm to the measurement volume for the laser beam, and from the aperture to the photomultiplier tubes (PMTs) for the LII signal. The single-lens imaging variant is used from the measurement volume to the beam profiler for the laser beam, and from the measurement volume to the aperture for the LII signal.

In relay imaging, a collimated laser beam that enters from the left, parallel to the optical axis, is both collimated and parallel after the image to the right, Fig. 4.2. This means that near to the image plane the fluence will be essentially constant, provided it was constant when entering the first lens. In the single-lens imaging, if a collimated laser beam enters from the left, parallel to the optical axis, it will be divergent after the image at the right. If this type of imaging is used for the laser beam when LII is employed, it is important to take into account the fact that close to the image plane the fluence will differ, depending on the distance from the lens. Regardless of which type of imaging that is employed, the sharp edges of an image will obtain fringes ("ringing") when moving out of the image plane along the beam axis. The amount of the

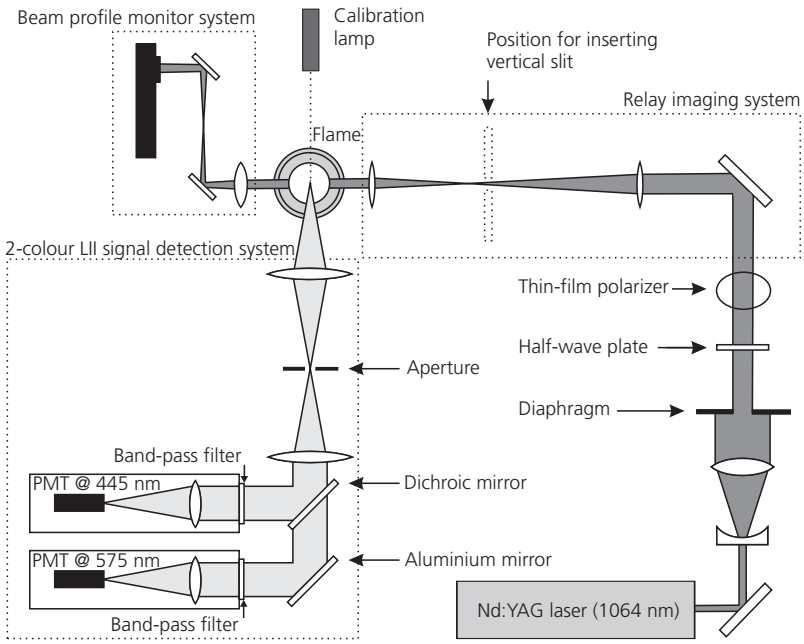

Figure 4.1: The time-resolved two-colour LII setup.

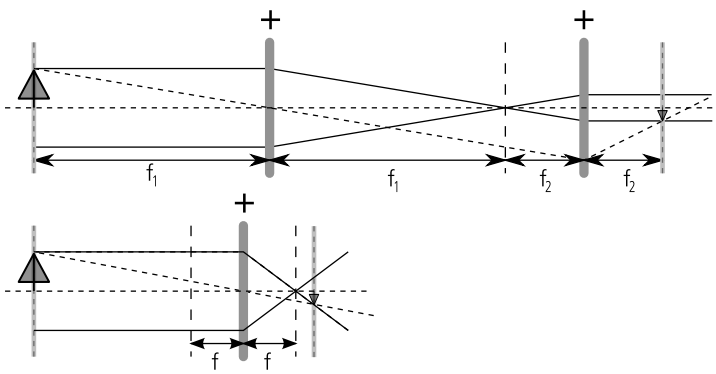

Figure 4.2: Top: Relay imaging using two positive lenses. **Bottom:** Imaging using one positive lens.

fringes present at a given distance from the image plane can be reduced by using lenses having longer focal lengths.

4.1 Laser Setup

The laser setup includes the laser itself and the optics used to shape the laser beam and direct it from the laser into the measurement volume, see Fig. 4.1. The measurement volume is the volume that is both illuminated by the laser and visible to the detectors, only particles within this volume being of interest in the evaluation. To obtain LII measurements having a high degree of accuracy, the setup described below has been designed so as to have well-defined properties, chosen to reduce the uncertainties in the evaluated particle sizes. Also included in the laser setup is an imaging of the laser beam onto a beam profiler having a high-resolution CCD chip. This is used to monitor the laser beam profile in real-time during measurements.

4.1.1 Laser

A laser is a device that can be used to create time- and space-coherent light which either comes in pulses or is continuous, and has a narrow bandwidth, together with a high irradiance, short duration and small divergence [40]. There are many types of lasers, each designed with specific properties in mind, such as laser wavelength, tunability, bandwidth, repetition rate and pulse duration. The Nd:YAG laser type has been much used in the LII community. This laser type has a Q-switch, meaning that the laser light is emitted in short pulses. The pulses are created by first blocking the stimulated light in the laser cavity during flashlight pumping, using a so-called Q-switch, in order to build up a large amount of excited atoms in the gain medium. When the blocking is removed, the laser light builds up almost instantly (~10 ns), resulting in a very short and intense laser pulse. The gain medium in the laser is yttrium aluminium garnet, YAG, some of the yttrium ions (Y^{3+}) of which have been replaced by neodymium ions (Nd^{3+}). For the lasing, the transition $^4F_{3/2} \rightarrow {}^4I_{11/2}$ in the neodymium ion is employed [40], resulting in a laser wavelength of 1064 nm.

In our measurements, we made use of a Quantel* Brilliant B pulsed Nd:YAG laser with a repetition rate of 10 Hz; Fig. 4.3. At this wavelength, the laser delivers a maximum pulse energy of 850 mJ at a pulse duration (FWHM) of 5.5 ns. The laser has a single longitudinal mode (SLM) option, this being provided

*Address: Les Ulis Cedex, France
URL: http://www.quantel-laser.com/

with an injection seeder. The injection seeder has a small continuous-wave infra-red laser that is directed through an optical fibre into the cavity of the Brilliant B, forcing it to generate laser pulses in a single longitudinal mode. Running the laser in the SLM mode provides the benefits of a smooth temporal laser pulse and of a reduced linewidth at the price of a slightly lower maximum energy level, 790 mJ per pulse. The single mode option can be used to minimise effects of steep gradients in the laser fluence that can appear when a multi-mode laser pulse is used. These steep gradients could possibly introduce non-thermal effects, especially at high fluence.

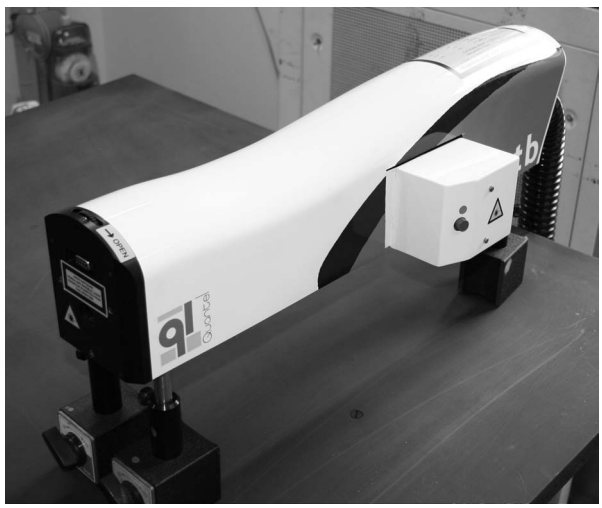

Figure 4.3: The Quantel Brilliant B pulsed Nd:YAG laser. The SLM option is provided by feeding the white box on the side of the laser with a cw beam of 1064 nm, emitted by an external rack. This is not included in the setup shown in this image.

4.1.2 Laser Optics

The laser optics are used to shape and relay the laser beam into the measurement volume. Because of uncertainties in the LII model at high fluences, it is desirable to keep the laser fluence low when evaluating particle sizes, so that the particle sublimation is negligible. It can be argued that a constant fluence

level within the measurement volume should be used for accurate measurement, since the LII signal strength is highly nonlinearly dependent upon the laser fluence. Such a profile, which is termed a tophat, has a constant fluence within the beam, one that drops to zero immediately outside of the beam. Although in the laboratory it is impossible to create a perfect tophat profile, it is possible to come quite close (see the left part of Fig. 7.2 on page 81, for example).

The spatial profile of the Brilliant B laser beam is smooth in shape, i.e. somewhere in-between a Gaussian and a tophat profile. To create a tophat beam profile in the laboratory, the beam is first expanded, using a telescope, see Fig. 4.1. Then an aperture is used to cut out a small part of the centre of the beam, where the fluence is almost constant. The aperture is then relay-imaged, using a pair of lenses, into the centre of the measurement volume.

4.2 Detection Setup

The detection system designed and built for the time-resolved two-colour LII measurements is depicted in Fig. 4.1. The laser-heated soot particles in the measurement volume emit light, which travels through the imaging optics and is then split into two beams by a dichroic mirror. The beams then pass into two aluminium boxes through narrow band-pass filters, that are centred at two different wavelengths. Inside the boxes the light from the measurement volume is imaged onto the sensitive surfaces of the PMTs. When the photons interact with the surfaces, electrons are emitted from the surfaces into the PMTs. These electrons are eventually amplified by a high voltage, resulting in an avalanche of electrons hitting the anodes of the PMTs. The total number of electrons collected there gives rise to a current within a circuit. This eventually results in a change in voltage, recorded using a fast oscilloscope. The voltage produced as a function of time, is the LII signal that is then evaluated to determine the size of the particles in the measurement volume.

By detecting the light at two different wavelengths, it is possible to carry out two-colour pyrometry on the soot particles and to measure their temperature with a temporal resolution. This simplifies and improves the LII measurement process, as described in Chapter 5.

4.2.1 Collection Optics

The collection optics of the system was designed to suppress light outside the measurement volume, and to be flexible so that the size of the measurement

volume could be changed easily. The first part of the optical setup consists of a single achromatic lens that images the centre of the measurement volume onto an aperture. By changing the size of the aperture, the size of the measurement volume can be controlled in the *x-y* plane (perpendicular to the direction of the propagation of light through the system).

The light that passes through the aperture is imaged using three lenses, the second and third performing the same action for each of the detectors. Since both of these last two lenses have the same purpose, only the imaging from the aperture to one of the detectors will be described. The imaging is achieved using two lenses that are set up for relay imaging; see Fig 4.2. For this imaging method, the first lens is positioned so that its distance to the aperture is equal to its focal length, whereas the second lens is positioned so that its distance to the detector is equal to its focal length. If the size of the intermediary aperture is relatively small, this arrangement results in the light between the two lenses being almost parallel to the optical axis. This matches the requirement for the filter specifications described below, which are valid for incoming light that is close to perpendicular to the filter surface. This arrangement results in almost all of the light that is collected by the first lens being imaged onto the detectors provided the light source at the aperture is not particularly large.

Between the two relay imaging lenses, the light is divided up by a dichroic mirror, which transmits light below a certain wavelength in the visible region, the rest being reflected at a 90° angle. The reflected light is filtered through a relatively narrow band-pass filter before it is imaged onto the sensitive surface of the first detector. The transmitted light is first reflected at a 90° angle by an aluminium mirror, before it is also filtered through a narrow band-pass filter into the second detector. The filters used here are ones manufactured by SEMROCK,* their having a high transmission level for the wavelengths of interest, resulting in a strong signal. The transmission profile of one of our filters is shown in Fig. 4.4 (SEMROCK BrightLine HC 575/25 50 mm).

The flame on the McKenna burner is designed to be one-dimensional, the soot particles in a rich flame occupying a cylindrical volume having a diameter of slightly less than 6 cm. Since there have been certain doubts regarding whether the flame actually is one-dimensional [21], and since we also had the intention of using the setup to test the one-dimensionality of the McKenna flame (Paper VI), the laser beam that was used for measurements in this flame

*Address: Rochester, New York
URL: http://www.semrock.com/

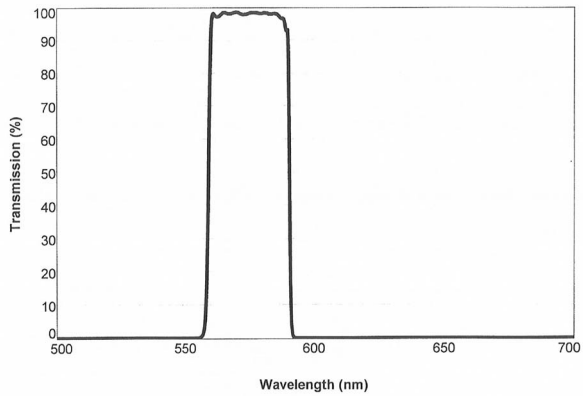

Figure 4.4: The transmission profile of one of our narrow-bandwidth transmission filters (SEMROCK BrightLine HC 575/25 50 mm).

was collimated and was small, its having a rectangular tophat beam profile of 1×2 mm (height×width).

It can be understood from Fig. 4.1 that, despite the aperture, light is collected not only from the strongly radiating soot particles present at the time in the measurement volume, but also from the weakly radiating particles located behind and in front of the measurement volume. These weakly radiating particles greatly outnumber the particles found in the measurement volume, this resulting in a noticeable background which affects the LII measurements negatively. It is easy to subtract the background from a time-resolved LII signal, since the background level is shown immediately before the LII signal appears, when it is recorded by use of the oscilloscope. This subtraction includes the light from the soot particles that are heated by the laser, and the same thing can easily be done for the model signals as well, prior to evaluation. Also, it is only the decay, not the background level, that determines the sizes of the particles found in the measurement volume. However, the extra background radiation that is collected also increases the noise contained in the signal, a matter which should be avoided. It can also reduce the accuracy of the signal level measurements if the background is too strong, due to the finite dynamic range of the detectors and the oscilloscope.

The temperature evaluation of the signals represents a much worse problem than the problems just described. To be able to perform the temperature evaluation accurately at all temperatures, it is necessary to subtract the background only of those particles that are *not* laser-heated. This has not been here. Instead only the temperature near the peak of the signal has been employed, where the

background is very small as compared with the signal and these errors can be neglected.

The background radiation can be partially suppressed by detecting the LII signals at short wavelengths. As can be seen in Fig. 2.3, the radiation envelope from the soot particles moves towards shorter wavelengths when the temperature increases. This is why the filters selected in Paper II are at the centre wavelengths of 445 nm and 575 nm. The LII signal is strong for the particle temperature interval of interest, but the level of the background radiation from the flame is relatively small at these wavelengths.

4.2.2 Detectors and Oscilloscope

At atmospheric pressure the LII signal has a duration typically on the order of a microsecond, which could appear to imply that the detectors, even if rather slow, can still reproduce the actual decay time with a high degree of fidelity. There are a number of reasons, however, why it is best to be able to detect the signal with a time resolution on the order of nanoseconds. One reason for this is that if one wants as much information out of a signal as possible, one would want, at least theoretically, to have access to the complete signal. This includes the very rapid increase at the beginning of a signal, one which is on the order of the duration of the laser pulse, i.e. ~10 ns. In cases of high fluence, the signal also has a sharper peak and a faster initial decay than otherwise, due to sublimation of the particles. Finally, the LII decay time decreases with pressure, so that at 20 bar the decay time is of the same order as the laser pulse duration [41]. Instead of using a high-time-resolution detector, deconvolution of the low-resolution signal can be used to restore the original signal.

To be able to accurately measure the LII signal shape, use was made of photomultiplier tube (PMT) modules with a rise time of 0.78 ns (Hamamatsu H6780–04 and –20). The signals from the PMTs are detected using a 1 GHz oscilloscope having 5 gigasamples per second per channel, a typical risetime of 400 ps and 8-bit vertical resolution (LeCroy WaveRunner 104MXi). A high bandwidth was chosen for the oscilloscope so as to not limit the fast response of the PMTs.

4.2.3 Beam Profiler

A beam profiler having a high density CCD chip was employed so as to be able to monitor the spatial laser beam profile in real-time during measurement. The centre of the measurement volume was imaged onto the CCD chip. In order to not damage the chip, the relatively strong laser beam was attenuated by use

of reflections from a series of glass plates (normally two or three of them) and a combination of neutral density filters.

4.2.4 Calibration Source

In order to be able to use the PMTs to conduct two-colour pyrometry on the soot particles, they need to be calibrated. This is carried out by using a calibration lamp of known spectral irradiance profile. For two-colour pyrometry, it is sufficient to calibrate the detectors in a manner such that the ratio of the soot particle irradiances at the two wavelengths is measured correctly, since only the ratio is needed for calculating the temperature.

The calibration lamp used in our experiments was the IES 1000 Intensity/Irradiance Calibration Lamp Standard manufactured by Labsphere Inc.,* irradiation data from 300 to 1050 nm being provided at 1 nm intervals. The IES 1000 consists of a tungsten halogen based lamp mounted in a cylindrical enclosure. There is a diffuser at the opening of the enclosure, making the calibration less sensitive to the exact directional positioning of the lamp in relation to the collection optics.

The calibration lamp is so placed that the light along its optical axis falls onto the centres of the PMTs. It is important to adjust the distance from the calibration lamp appropriately in relation to the measurement volume, and the gain of the PMTs, so that the light that reaches the PMTs has an irradiance that is within the linear regime of the detectors. Since only the ratio of the irradiances at the two wavelengths are needed, the distance to the lamp need not be measured. Once the detection setup has been calibrated, the gain of the PMTs should not be changed during the subsequent LII measurements, since otherwise the calibration data would no longer be valid. For experimental convenience, it is thus often a good idea to set the gain of the PMTs such that the LII signals are always within their linear response regimes, and to then only use the distance from the calibration lamp to the aperture to ensure that the calibration irradiance is within the linear regimes of the PMTs.

*Address: North Sutton, New Hampshire, USA
URL: http://www.labsphere.com

Chapter 5

Particle Size Evaluation using LII

The first part of this work has involved building an experimental setup for time-resolved two-colour LII, and developing the evaluation tools necessary for determining the particle sizes from laboratory measurements. To evaluate particle sizes from an LII signal, it needs to be time-resolved, since the size information is extracted from the decay rate of the signal. Smaller particles cool faster than larger ones do, and since the LII signal is dependent on the temperatures of the particles, it is possible to determine the particle sizes in a probe volume on the basis of the decay of the signal. In some cases it is even possible to obtain an estimate of the particle distribution. Since there are many different ways of evaluating experimental LII signals so as to determine the sizes of the soot particles, the choices made for our evaluation procedure will be motivated.

5.1 The LII Model

To be able to evaluate experimental LII signals it is necessary to use a model of the LII process. The LII model describes the process of the laser heating of the soot particles, and the interactions of the particles with their surroundings during the laser pulse and the cooling phase.

5.1.1 Energy and Mass Balance

The differential equations for the energy and mass balance describe the energy and mass flow into and out of the soot particles, and how this affects their internal energy and changes in temperature. The heat-transfer equation for the current model can be written as

$$\dot{Q}_{\text{int}} = \dot{Q}_{\text{abs}} - \dot{Q}_{\text{con}} - \dot{Q}_{\text{sub}} - \dot{Q}_{\text{rad}}, \tag{5.1}$$

where the dots denote time derivatives. The equation describes how the internal energy, $\dot{Q}_{\text{int}}$, of a soot particle changes when the energy of the laser pulse is absorbed. The heat conduction term, $\dot{Q}_{\text{con}}$, describes how heat is transferred from the particle to the ambient gas through collisions with the molecules of the gas. If the temperature of the soot particles becomes sufficiently high, $\gtrsim$3600–4000 K, the soot particles start to sublime, which is described by the sublimation term, $\dot{Q}_{\text{sub}}$. The thermal radiation term, $\dot{Q}_{\text{rad}}$, describes the blackbody radiation from the particle.

Assuming the soot particles to be spherical, the mass balance equation can be written as

$$\frac{dm_{\text{p}}}{dt} = -\pi d_{\text{p}}^2 N_{\text{v}} \frac{M_{\text{v}}}{N_{\text{A}}}, \tag{5.2}$$

where m_{p} is the mass of the particle, d_{p} is the particle diameter, N_{v} is the molecular flux of sublimated carbon, M_{v} is the molecular weight of soot vapour and N_{A} is the Avogadro constant.

In the LII model, the temperature and the particle diameter can be thought of as state variables for the differential equations, Eqs. (5.1) and (5.2), after the influence of the laser pulse. This means that if the temperature and the diameter are both known at one time, all the properties of the system can be calculated for that point in time and forward.

The following descriptions of the different terms in the energy balance equation will not include thorough definitions and discussions of all of the terms, but include what is needed to provide a basic understanding of the model. A detailed description of the model is available in Paper I and in [42]. Since it is relatively complicated to describe aggregation and its effects on LII, aggregation is not taken up in this chapter. Instead, it is described in Chapter 6, in which the model for LII described here is modified so as to include aggregated particles.

The rate of change of the internal energy of a soot particle can be written as

$$\dot{Q}_{\text{int}} = \frac{\pi d_{\text{p}}^3}{6} \rho_{\text{s}} c_{\text{s}} \frac{dT}{dt}, \tag{5.3}$$

where $\pi d_{\text{p}}^3/6$ is the volume of a particle, ρ_{s} is its mass density, c_{s} is its specific heat capacity and dT/dt is its rate of temperature change. The light absorption of a spherical soot particle leads to an energy transfer term,

$$\dot{Q}_{\text{abs}} = C_{\text{abs}} F(t) = \frac{\pi^2 d_{\text{p}}^3}{\lambda} E(m) F(t), \tag{5.4}$$

in which C_{abs} is the absorption cross section as described previously in Eq. (3.5), and $F(t)$ is the laser irradiance incident on the particle presented, as a function of time, t.

5.1.1.1 Heat Conduction

The most important term in evaluating particle sizes at low fluence is the heat conduction term. During the cooling of a soot particle, the molecules in the ambient gas interact with the hot surface of the particle, so that the gas becomes heated by the particle, resulting in a heat loss for the particle. There are three regimes for heat conduction from a particle to a gas. These can be characterised using the Knudsen number [43],

$$\text{Kn} = \frac{\lambda_{\text{MFP}}}{L}, \tag{5.5}$$

where λ_{MFP} is the Maxwell mean free path [44] of the molecules in the gas and L is a characteristic length scale of the particle, chosen here as the diameter of the particle. The mean free path of a molecule is the average distance a molecule in the gas travels before it collides with another molecule in the gas. In the free-molecular regime, the Knudsen number is $\gtrsim 10$, so that the molecules that interact with the particle move far away from the particle before starting to exchange energy with the surrounding gas. In the continuum regime, the Knudsen number is $\lesssim 0.1$, so that the gas can be regarded there as a viscous fluid with respect to the particle. In between the free-molecular and the continuum regime is the transition regime, in which $0.1 \lesssim \text{Kn} \lesssim 10$. In LII applications, the two most interesting regimes are the free-molecular regime and the transition regime. In open-air flames under standard ambient conditions, $\lambda_{\text{MFP}} \approx 560$ nm, which results in a Knudsen number in the range of 11–56 for particles having diameters in the range of 10–50 nm. Since the mean free path is inversely proportional to the gas pressure, measurements in internal combustion engines and other high-pressure applications result in heat conduction in the transition regime.

McCoy and Cha [45] proposed an expression describing the heat transfer from a spherical particle to the surrounding gas, in the transition regime,

$$\dot{Q}_{\text{con,MC}} = \frac{2k_{\text{g}}(T - T_{\text{g}})\pi d_{\text{p}}^2}{d_{\text{p}} + G\lambda_{\text{MFP}}}, \tag{5.6}$$

where k_g is the thermal conductivity of the gas, T_g is the gas temperature, T is the temperature of the particle and G is the geometry-dependent heat transfer factor. This expression is valid only if the temperature of the particle is close to that of the gas, meaning that the expression is generally not valid for LII measurements [44]. It does have a closed form expression, however, and is useful in providing an understanding of the approximate effect of different parameters on the heat transfer due to conduction. Also, it has often been used in LII investigations, following Melton [29].

Filippov and Rosner [46] extended the heat conduction model of Fuchs [47]. In that model, termed in the LII community the Fuchs model, it is not assumed that there is only a small temperature difference between the particle and the gas. The Fuchs model describes the gas surrounding the spherical particle by use of an approximation involving two layers. In the inner layer, having a thickness of δ_{FM}, heat conduction occurs in the free-molecular regime, without collisions between the molecules, the soot particle being at temperature T and the boundary sphere at temperature T_δ. In the outer layer, which stretches to infinity, heat conduction occurs in the continuum regime, from the boundary sphere at temperature T_δ to the ambient gas at temperature T_g. For this approximation to make physical sense, the heat flux away from the free-molecular regime must be equal to that of the heat flux into the continuum regime. Such conditions can be obtained by tuning δ_{FM} and T_δ until $\dot{Q}_{con,FM} = \dot{Q}_{con,cont.}$ at the boundary sphere. For a detailed account of the Fuchs model, see Liu et al. [48].

It has been shown that the Fuchs model is in very close agreement with Monte Carlo simulations of the heat transfer, and that it compares favourably with many other heat conduction expressions, especially when the temperature difference is large [48]. The Fuchs model does not have a closed form expression, and determining the heat transfer under given conditions is an iterative procedure. Both the McCoy and Cha model and the Fuchs model for heat conduction are included as options in our LII model implementation.

5.1.1.2 Sublimation, Annealing, Oxidation and Photodesorption

In the high fluence regime (a pulse fluence of $\gtrsim 0.3\,J/cm^2$ for a laser wavelength of 1064 nm), particle sublimation becomes an important factor. The rate of sublimation depends on the heat of sublimation for soot, the particle surface area, and the molecular flux of sublimated carbon. In our model, the expression that describes the energy transfer caused by sublimation is based on that

given by Snelling et al. [49] and by Smallwood et al. [50], which can be written as

$$\dot{Q}_{\mathrm{sub}} = -\frac{\Delta H_{\mathrm{v}}}{M_{\mathrm{v}}}\frac{dm_{\mathrm{p}}}{dt}, \tag{5.7}$$

where ΔH_{v} is the heat of sublimation for soot, M_{v} is the molecular weight of soot vapour, and m_{p} is the mass of the particle.

There may be additional physical terms that affect the LII process. Three terms that have been discussed are those of annealing, oxidation and photodesorption [13]. If the laser fluence is high, the particles may possibly anneal, meaning that their surface structure changes. Oxidation of the particles may also affect the LII process. If very high fluences are employed, photodesorption may affect the measurements. In a photodesorption event, a single photon causes the desorption of an atom or molecule from the particle surface [51]. The three terms referred to above are not included in the present work, not because they are known to have no effect, but because the extent of their effect is uncertain or unknown. Since annealing and photodesorption are not believed to be an issue in low-fluence measurements [13], it is only the oxidation term that may have an effect on the results under such conditions. Omission of these terms in the present work is dealt with as an uncertainty in the evaluation.

5.1.2 Calculation of the Temperature and Diameter as Functions of Time

As already indicated, the temperature, T, and the particle diameter, d_{p}, can be seen as variables that describe the state of the soot particle. If these variables are known as functions of time, the time-resolved LII signal can be calculated. If the initial values of T and d_{p} are known, Eqs. (5.1) and (5.2) can be used to calculate their values at all future times, in the following way:

First Eq. (5.2) is rewritten in terms of d_{p} instead of the particle mass, m_{p}. The mass can be written then as

$$m_{\mathrm{p}} = \frac{\pi}{6}\rho_{\mathrm{s}} d_{\mathrm{p}}^3, \tag{5.8}$$

which has the time-derivative

$$\frac{dm_{\mathrm{p}}}{dt} = \frac{\pi}{2}\rho_{\mathrm{s}} d_{\mathrm{p}}^2 \frac{dd_{\mathrm{p}}}{dt} + \frac{\pi}{6} d_{\mathrm{p}}^3 \frac{d\rho_{\mathrm{s}}}{dT}\frac{dT}{dt}. \tag{5.9}$$

This expression can then be rewritten as

$$\frac{dd_\mathrm{p}}{dt} = \frac{2}{\pi \rho_\mathrm{s} d_\mathrm{p}^2} \left(\frac{dm_\mathrm{p}}{dt} - \frac{\pi}{6} d_\mathrm{p}^3 \frac{d\rho_\mathrm{s}}{dT} \frac{dT}{dt} \right). \tag{5.10}$$

By using the expression for the internal energy, Eq. (5.3), the heat transfer expression, Eq. (5.1), can be rewritten as

$$\frac{dT}{dt} = \frac{6}{\pi d_\mathrm{p}^3 \rho_\mathrm{s} c_\mathrm{s}} \left(\dot{Q}_\mathrm{abs} - \dot{Q}_\mathrm{con} - \dot{Q}_\mathrm{sub} - \dot{Q}_\mathrm{rad} \right). \tag{5.11}$$

Eqs. (5.10) and (5.11) can then be time-integrated, using a numerical method for solving ordinary differential equations to calculate $T(t)$ and $d_\mathrm{p}(t)$, starting from their initial values.

5.1.3 LII Signal

The LII signal is the detected enhanced thermal radiation from the soot particles within the measurement volume. To detect the signal, it is usually collected and imaged onto a detector, such as a PMT or a camera. The signal from a single spherical soot particle can be described by

$$S_\mathrm{mod,mono} \propto \int_0^\infty R(\lambda) \left[I(d_\mathrm{p}, \lambda, T) - I(d_\mathrm{p}, \lambda, T_\mathrm{g}) \right] d\lambda, \tag{5.12}$$

where λ is the wavelength, R contains all wavelength dependencies of the collection optics, such as filters, I is the thermal irradiation of soot as given by Eq. (2.8), T_g is the ambient gas temperature, and d and T are the particle diameter and the particle temperature, respectively.

The particles in the measurement volume can be of different sizes and there can be different numbers of those of each size, resulting in a signal that can be written as

$$S_\mathrm{tot}(t) = \int_0^\infty S_\mathrm{mod,mono}(d_\mathrm{p}, t)\, p(d_\mathrm{p})\, dd, \tag{5.13}$$

where $p(d_\mathrm{p})$ is the particle size distribution. For computer evaluations it is convenient to approximate the continuous particle size distribution $p(d_\mathrm{p})$ with its discretised equivalent,

$$S_\mathrm{tot}(t) = \sum_{i=1}^{N} S_\mathrm{mod,mono}(d_{\mathrm{p},i}, t)\, p_i, \tag{5.14}$$

where the $d_{\mathrm{p},i}$s are the discretised diameters.

5.2 Low-Fluence Approximation

The energy and mass balance equations, Eqs. (5.1) and (5.2), consist of a number of terms having parameters that all are to various degrees uncertain. Since the sublimation term is one of the most uncertain terms, it is of considerable interest to be able to reduce the effect of this term in performing LII measurements for particle sizing. This is done by operating in the low-fluence regime, using a laser fluence of less than ~0.12 J/cm^2, when the laser wavelength is 1064 nm. When the fluence is that low, the temperatures of the particles are always well below the sublimation level, so that the effect of the sublimation term to a good approximation can be omitted. Staying below the sublimation temperature, however, unfortunately means that the signal is weaker than it would otherwise have been, if the temperature of the particles is higher (see Eq. (2.10)). The following indicates how particle size evaluations in the low-fluence regime can be carried out.

5.3 Adaptation of Model Parameters to Experiment

In order to be able to compare an experimental LII signal with a theoretical signal from the LII model, the (setup) parameters of the computer LII model need to be set to match as closely as possible the conditions of the experiment. For particle size evaluation, all parameters except those involving the particle size distribution are usually fixed. Even though the experimental LII signal can be considered to be continuous in time, the sampling of the digital oscilloscope results in a time-discretised signal. The experimental signal is then represented as a vector, its values corresponding to the strength of the signal at different times. The vector length and time steps for the model signals are set to the same values as those for the experimental signal.

The LII signal generated by the model is created by using a modelled laser pulse, one having the same characteristics as in the experiment, as input data. Alternatively, the laser pulse time profile can be measured in the experiment, and then be used as input data in the model. To ensure that the experimental and modelled signals are properly aligned in time prior to the comparison, the position of the peak of the modelled laser pulse is adjusted so that the experimental and modelled signal peaks coincide.

5.4 Temperature Evaluation

A correct temperature for the particles can only be calculated from LII signals under certain circumstances, which will now be described in some detail.

Assuming that the shape of the broadband radiation function of soot is given by the greybody radiation formula in Eq. (2.8), it is possible to calculate the temperature of a soot particle by simply knowing the relative irradiances of its thermal radiation at two wavelengths. The ratio of the two irradiances, I_1 and I_2, at the wavelengths, λ_1 and λ_2, is given by (see Eq. (2.8))

$$\frac{I_1}{I_2} = \frac{\varepsilon(d_\mathrm{p},\lambda_1)\dfrac{2\pi hc^2}{\lambda_1^5\left(\exp\left(\dfrac{hc}{\lambda_1 k_\mathrm{B} T}\right)-1\right)}}{\varepsilon(d_\mathrm{p},\lambda_2)\dfrac{2\pi hc^2}{\lambda_2^5\left(\exp\left(\dfrac{hc}{\lambda_2 k_\mathrm{B} T}\right)-1\right)}}, \tag{5.15}$$

which can be solved for T, iteratively. An explicit and faster way to obtain T is to note that, for many combustion applications of LII,

$$\exp\left(\frac{hc}{\lambda k_\mathrm{B} T}\right) \gg 1 \tag{5.16}$$

(For example, $\exp\left(hc/\lambda k_\mathrm{B} T\right) > 170$ for λ in the range of 400–700 nm and T in the range of 1500–4000 K.) Thus it is a good approximation to omit the -1 in Eq. (5.15), this making it possible to solve for the temperature,

$$T = \frac{hc}{k} \cdot \frac{1/\lambda_2 - 1/\lambda_1}{\ln\left(\dfrac{E(m(\lambda_2))}{E(m(\lambda_1))} \cdot \dfrac{I_1}{I_2} \cdot \left(\dfrac{\lambda_1}{\lambda_2}\right)^6\right)}, \tag{5.17}$$

where the expression for the emissivity, Eq. (2.9), has been used. For soot, $E(m)$ is a function that varies quite slowly with the wavelength, λ. If the wavelengths λ_1 and λ_2 are not particularly far apart, it is a good approximation to set the ratio of the $E(m)$s to one another to 1.0, resulting in

$$T = \frac{hc}{k} \cdot \frac{1/\lambda_2 - 1/\lambda_1}{\ln\left(\dfrac{I_1}{I_2} \cdot \left(\dfrac{\lambda_1}{\lambda_2}\right)^6\right)}, \tag{5.18}$$

For the wavelengths used in the work reported in Paper II of the thesis (445 nm and 575 nm), this expression for the temperature deviates by less than 0.1 % from the temperature calculated using the full expression, i.e. Eq. (5.15), for particles having temperatures in the range 1500–4000 K.

If the signal comes from a size distribution of soot particles, the temperature equation for a soot particle, Eq. (5.18), can still be used as long as the particles have approximately the same temperature. This is not the case for soot particles in an LII measurement generally, but measures can be taken to assure that the *peak* temperatures of the particles are approximately the same. Since soot particles are volume absorbers if they are small relative to the laser wavelength, they all have approximately the same temperature directly after being heated by the laser pulse, provided they have all been subjected to the same laser fluence.* This is only the case if the laser profile has a tophat shape, that is, if there is only one fluence within the laser profile. When such is the case, uncertainties in the absorption term in the LII model have a much lesser effect, since that term can be calculated then from the experimental signals directly, on the basis of the peak temperature of the particles.

If all the particles within the measurement volume are of approximately the same size, it is possible to determine the real temperature trace of the soot particles for the duration of the LII signal as a whole, including the temperature decay (as long as the noise level is sufficiently low). This is rarely the case, however, since even the distribution of the primary particle diameters at a specific height in a McKenna burner flame, that burner being designed to give "one-dimensional" flames, has a FWHM (full-width at half maximum) of as much as 10 nm at 12 mm above the burner (Paper II). It is still possible nevertheless to use Eq. (5.18) to calculate an effective temperature curve, T_{eff}, for the particles, one that can be compared with a similar effective temperature curve calculated using the LII model.

Comparing the experimentally acquired and the modelled temperature curves enables the particle size distribution to be evaluated in a manner similar to that which will be described in Section 5.6. However, the temperature calculated from Eq. (5.18) depends on the ratio of the two irradiances, I_1/I_2, both of which are degraded by noise, when these are measured experimentally. Taking the ratio of two noisy signals amplifies the noise and makes it more difficult to make accurate evaluations. Also, to calculate the correct (effective)

*This assumes the processes that cool the particles are much slower than the rapid heating by the laser pulse. The assumption is clearly applicable in the case of flames at atmospheric pressure, but may not be as applicable under high-pressure conditions, since the much higher heat conduction to the ambient gas there may have a noticeable effect, also during the laser pulse.

temperature, the background stemming from the particles that were not laser-heated needs to be removed. Since it is no simple matter to determine the exact level of this background, the temperatures close to the flame temperature remain uncertain. These are the reasons for the particle sizes being evaluated not on the basis of the "effective" temperature decay, but on the basis of the signal decay instead.

5.5 Signal Preparations

Before the model evaluation of the experimental signals is carried out, the signals needs to be prepared. In all of the following, the incident laser pulse is assumed to have a tophat spatial profile, a temporal profile with a FWHM of ~10 ns and a fluence in the low-fluence regime.

Since the peak temperature of the particles has been calculated, the usually uncertain parameter $E(m)$ is not needed beforehand in order to calculate the absorption term, using Eq. (5.4). Instead, the amplitude of the absorption term is tuned in the model until the peak temperature of the model and the experiment agree. When the absorption has been calculated, it can be included in the energy balance equations. However, calculating the absorption term using the *peak* value of the temperature has the disadvantage that a part of the laser pulse heats the particles, even after their maximum temperature has been reached. The reason that the particles can cool even when the pulse has not yet passed is that the heat conduction term, though generally small compared with the absorption term, becomes larger than the absorption term by the end of the pulse.

It would be useful if evaluation of the signal could start after the absorption term has played its role, since the exact shape and magnitude of the laser pulse could then be ignored in evaluating the decay. To do this, instead of adjusting the absorption term so that the experiment and model *peak* temperatures agree, the absorption term is adjusted so that the *effective* temperature, T_{eff}, of the experiment and the model agree directly after the laser pulse has passed, this being defined as time t_0.* The effective temperature, together with the diameter distribution which is to be fitted, define the state of the particles completely, so that the evaluation can be started at t_0 even if at that time only T_{eff} is known. It is important to note, however, that the effective temperature depends on

*This time can be chosen to be even later if this is needed, and the evaluation will be essentially the same. One problem in choosing too large a value for t_0 is that less information regarding the particle sizes will be available later, especially for smaller particles, for which the signal decays quickly.

the particle size distribution. Since the distribution is varied during the fitting procedure, it is important to check that the effective temperature as obtained from the model matches that of the experiment at t_0, each time the distribution is changed.

5.6 Signal Decay Evaluation

Once the parameters for the LII model have been determined, and the procedure described in the previous section has been carried out, everything is prepared for evaluating the particle size distribution of the experiment. This involves finding the particle size distribution that results in the signal that most closely resembles that from the experiment. For the signal decay evaluation, only the parts of the modelled and the experimental signal starting at t_0 and ending at the last time value for the experimental signal, t_{end}, are used, for the reasons taken up in the previous section.

The modelled signal, S_{mod}, which is most similar to the experimental signal, S_{exp}, is defined here as that which is the closest in the least-squares sense. Since all experimental signals are sampled, the problem here is discrete, so that the best fit can be found by minimising the sum of the residuals,

$$r_{\text{tot}}(p(d_{\text{p}})) = \sum_{i=1}^{M} r_i(p(d_{\text{p}})) = \sum_{i=1}^{M} (S_{\text{mod},i}(p(d_{\text{p}})) - S_{\text{exp},i})^2, \qquad (5.19)$$

where it is shown explicitly that the modelled signal is a function of the particle size distribution of diameters, $p(d_{\text{p}})$.* The index of summation, i, is used to denote the times of the elements in the signal vectors, so that $i = 1$ corresponds to t_0 and $i = M$ corresponds to t_{end}, M being the number of elements in the signal vectors.

To find the best fit, use is made of a minimisation algorithm. If nothing is known about the particle size distribution in advance, it is very difficult to find a particle distribution that is similar to the distribution that was the source of the signal. The reason for this is that the problem of getting back from the signal to the original size distribution is a mathematically ill-conditioned problem, since there are many different distributions that each give a very small total residual, r_{tot}. In short, the problem lies in the fact that an LII signal from

*Note that the sum of the residuals is a function of the entire function $p(d)$, its not being just a function of d, since all the values in $p(d)$ are needed to calculate r_{tot}.

a particle size distribution is given by the weighted sum of a usually large number of decays (see Section 5.1.3), each decay corresponding to the signal of a particle of a particular size. Although it is simple to generate such a signal, finding the frequency of each particle size from such a sum of different decays is very difficult. Although it is rather easy to find a distribution that results in a model signal that fits the experimental signal very well, there is no guarantee that this distribution is at all similar to the original distribution. To be able to solve the problem, some constraint on the problem is needed.* The constraint is one based on certain prior knowledge of what the shape of the distribution should be. It is important to bear in mind that imposing a constraint on the solution removes all possible solutions that are not compatible with the constraint. Thus it is important to choose the constraint wisely.

One way to impose a constraint on the distribution is to assume that it is given by a parametrised function. The simplest parametrised function is the monodisperse distribution,

$$p(d_\mathrm{p}, d_\mathrm{mono}) = \begin{cases} 1, & d_\mathrm{p} = d_\mathrm{mono} \\ 0 & \text{otherwise} \end{cases}, \tag{5.20}$$

which has the property that all particles in the distribution have the same size, namely d_mono. This distribution can be used if the distribution that is probed experimentally is known to be narrow, or if only the approximate size of the particles in the distribution is sought.

Soot particles within combustion processes have been shown to often have a size distribution that is approximately lognormal [53],

$$p(d_\mathrm{p}, d_\mathrm{g}, \sigma_\mathrm{g}) = \frac{1}{\sqrt{2\pi} d_\mathrm{p} \ln \sigma_\mathrm{g}} \exp\left(- \left(\frac{\ln\left(d_\mathrm{p}/d_\mathrm{g}\right)}{\sqrt{2} \ln \sigma_\mathrm{g}} \right)^2 \right), \tag{5.21}$$

*In theory, it may be possible to test "all" possible distributions, and to choose as the solution the one that gives the smallest total residual. This is the most unconstrained method I can think of, but the computational effort needed to do this is would be enormous. Here is an example, one in which the result is still at quite low resolution (and which might thus still not be similar to the original distribution): Assume the original distribution is known to have a range (from the smallest to largest particle size) of 40 nm, and that one discretises this range in 1 nm steps. Assume too that the ratio of the maximum to the minimum (non-zero) of the distribution is 9, and that each particle size can have a frequency of 0 to 9 (integers only). Then, the number of distributions that need to be tested is 10^{40}. If a thousand distribution can be carried out per second, the total time for this algorithm to be completed would be approximately 10^{19} times the currently estimated age of the universe [52]. This thesis is unfortunately due before such a computation can be completed.

where d_g and σ_g are the geometrical mean diameter and the geometrical standard deviation, respectively. If a lognormal distribution is plotted with the d_p axis in log-scale, the shape of the distribution is that of a normal distribution.

Once a parametrised function is selected, the total residual equation, Eq. (5.19), can be calculated. Many algorithms that are used to find the minimum of the total residual need an initial guess of the parameters, which can be regarded as a point in the parameter space. The algorithm then looks at the value of the total residual at the initial guess and at some neighbouring points in the parameter space. On the basis of this information, the algorithm calculates a new guess, one that has a smaller total residual, and uses the neighbouring points of the new guess to calculate another, better, point. The iteration continues until the solution is deemed "good enough". This condition can be based, for example, on how small the total residual is or how short the steps of the parameters of the last iteration are. Two examples of least squares fits, using a monodisperse size distribution, are shown in Fig. 5.1.

For the monodisperse and the lognormal distributions, it appears that the correct solution can be found independent of what the initial guess is. The tests that have been performed indicate that there is only one global minimum point for the least-squares fitting of these distributions to an arbitrary experimental signal, and that there are no local minima [54]. Thus the solution is not dependent on the initial guess, but can be found more quickly if the initial guess is close to the solution.

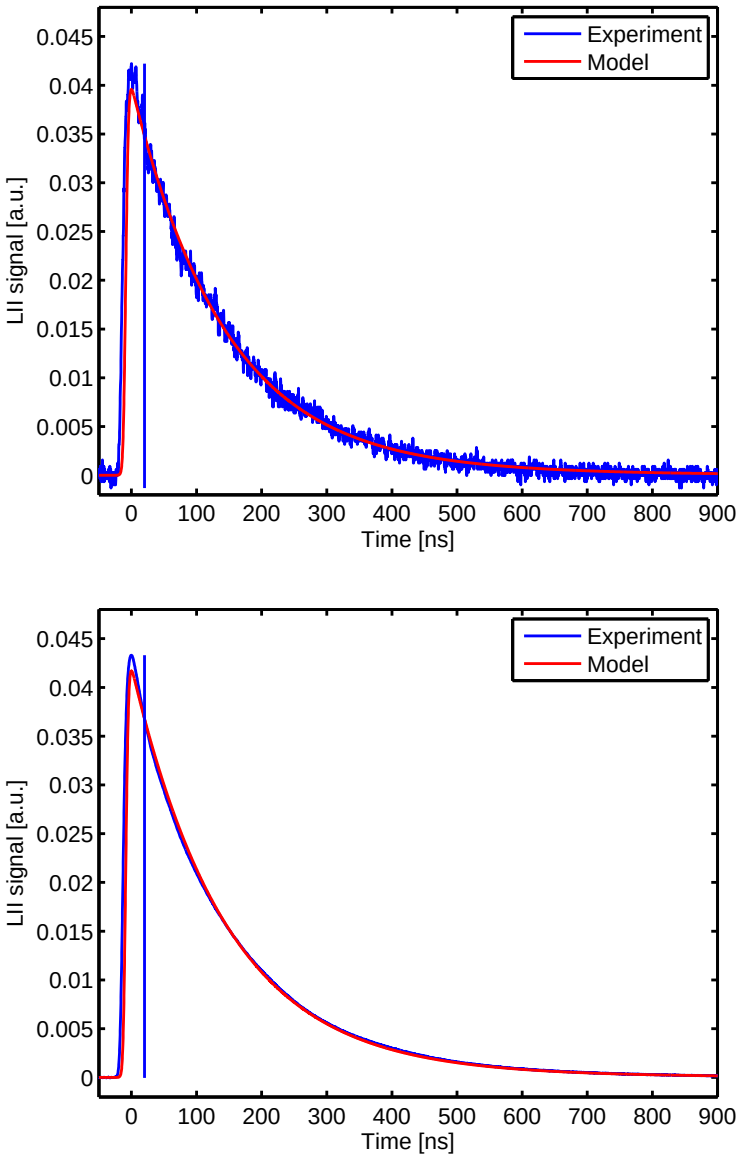

Figure 5.1: Least squares fits to experimental signals using modelled signals from a monodisperse particle size distributions. The experimental signal is the one used in Paper II, from 10 mm above the burner at $\Phi = 2.1$. The burner properties are shown in Table 2.1. **Top:** Single-shot evaluation. **Bottom:** Evaluation of the mean of 1000 signals.

Chapter 6

The Effect of Soot Aggregation on LII Particle Sizing

When the fuel/air ratio in a combustion process is sufficiently high, soot aggregates are often formed in the last step of the soot formation process (cf. Section 2.1). These soot aggregates are formed in a random process in which initially approximately spherical soot particles stick together, forming small aggregates. These, in turn, stick together, and in this way larger and larger aggregates are created. Since the collisions are random, this process results in randomly structured aggregates, with a broad range of number of primary particles within each aggregate [55].

The primary particles within an aggregate shield each other from the ambient gas so that the heat conduction rate decreases as compared with what it had been if the primary particles had not been in contact. To make accurate evaluations of particle sizes by use of LII it is thus necessary to take this shielding into account [56]. To calculate the shielding, it is necessary to first construct aggregates numerically.

In Paper V measurements were made on soot aggregates and LII signals were evaluated using the LII model, using the aggregation corrections by Liu et al. [48] for the heat conduction term. The same model was used to calculate a comparison value in Paper IV. In Paper VII the effect of bridging between primary particles in an aggregate on the heat conduction from aggregates, and the implications for LII evaluations, were investigated.

In this chapter the concept of fractals is first explained and it is shown how it can be used to describe and analyse the structure of soot aggregates. It is then shown how soot aggregates can be constructed numerically, with and without bridging. It is also described how the heat conduction rate from the aggregates

to the ambient gas can be calculated. Finally, it is described how the shielding is quantified and how it can be incorporated into the LII model.

6.1 Fractals

The term *fractal* was introduced by Benoît B. Mandelbrot in 1975 (in a French book, translated to English in 1977 [57]) as a name for structures that are *self-similar*. The self-similarity of a structure lies in that it looks similar independent of the scale at which it is observed. Such structures can be constructed theoretically. As an example it is shown in Fig. 6.1 how to construct the fractal known as the Koch snowflake [58]. Starting out with an equilateral triangle, the snowflake is constructed iteratively, by replacing each straight line of the object with an angular shape in each step. The fractal is constructed by repeating this process infinitely many times. The Koch snowflake has some mind-bending properties: it consists of a continuous line of infinite length (by construction) having no derivative at any point; still the line encloses an area of finite size. It is possible to construct fractal objects with a wide variety of shapes and forms, yet one thing they all have in common is that they have rich structures that are present, independent of the scale they are viewed at. The fractal dimension, D_f, is one of the parameters that characterizes a fractal object.

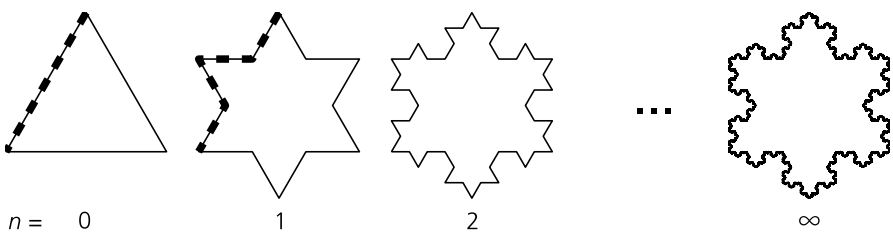

Figure 6.1: The Koch snowflake [58]. At each iteration, n, each straight line is replaced by an angular shape, marked with a dashed line, from $n = 0$ to $n = 1$. The fractal structure is only complete when $n \to \infty$.

6.1.1 Determining the Fractal Dimension of an Object

For non-fractal objects, the spatial dimension, D, describes how the object extends in space,* such as a point ($D = 0$), a line ($D = 1$), a plane ($D = 2$), or a cube ($D = 3$). One method of determining the dimension of a non-fractal object is to use the box-counting algorithm [59]: count the number of cubic boxes, N, having side lengths s, that are needed to completely cover the object. The side length here can be thought of as the scale at which we observe the object. The relation between N and s can, when s is sufficiently small, be written as

$$N(s) = \frac{1}{s^D} \Leftrightarrow \ln N(s) = D \cdot \ln \frac{1}{s}, \tag{6.1}$$

where D is the dimension of the object. Figure 6.2 shows a visualization of how N increases with decreasing s in some simple cases. It can be seen that one large box is sufficient to cover both the line, the plane and the cube. When the side length of the boxes, s, is halved, more boxes are needed, and the increase is larger the higher the dimension of the object is.

The dimension of an object can be calculated as

$$D = \lim_{s \to 0} \frac{\ln N}{\ln(1/s)}. \tag{6.2}$$

The reason that the limit needs to be taken is that edge effects and the overall shape of the object could otherwise influence determination of the dimension of the object; the objects and boxes in Fig. 6.2 are special cases that show the simple dependence of Eq. (6.1) also when s is large.

For non-fractal objects, calculating the dimension by use of Eq. (6.2) always results in an integer value (0, 1, 2 or 3). If the object is a fractal, Eq. (6.2) can be used to calculate the fractal dimension ($D_\mathrm{f} = D$), a value that is generally not an integer but can be any value in the range from 0 to 3. As an example, the circumference of the Koch snowflake has a fractal dimension of $\ln 4 / \ln 3 \approx 1.26$ [60].

In reality, it is seldom possible to calculate the limit in Eq. (6.2), because experimental data in general are limited in resolution. Instead, $\ln N$ is plotted as a function of $\ln 1/s$, and the slope is used to determine the fractal dimension D_f. In Fig. 6.2 this procedure has been carried out for some simple objects, showing that the slopes yield the integer dimensions 1–3. The same procedure

*We only consider here objects in Euclidean, three-dimensional space.

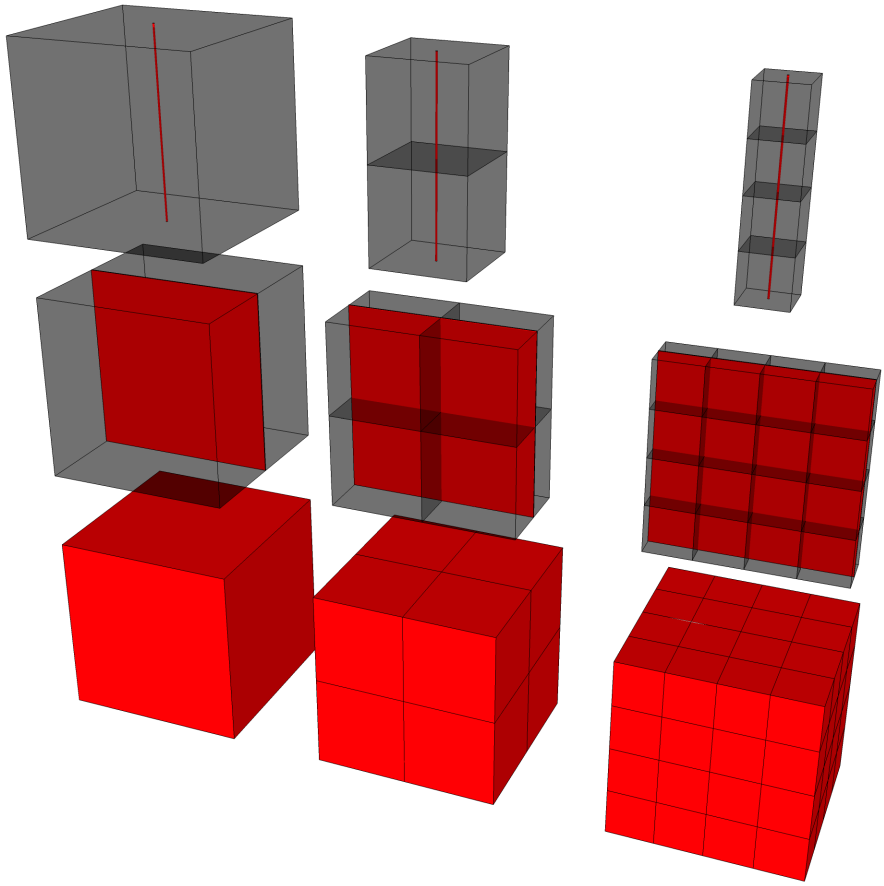

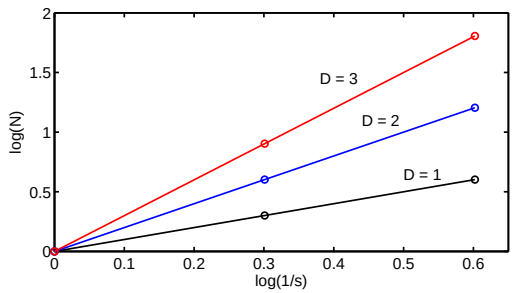

Figure 6.2: Top: An illustration of determining the dimensions of a (red) line, a plane and a box, using the box-counting algorithm. When the side length, s, of the covering grey boxes is decreased, a larger number of boxes, N, are needed. **Bottom:** By plotting $\log N$ as a function of $\log 1/s$, the dimension of the objects can be obtained from the slopes.

was made in Fig. 6.3, for a simplified Koch snowflake and at a wide range of box sizes. The simplifications are that only seven iterations of the algorithm shown in Fig. 6.1 ($n = 7$) were made and that only the corner-points of the snowflakes were used (not the lines in between). Despite these simplifications much can be learned from Fig. 6.3 that is relevant for the analysis of soot aggregates.

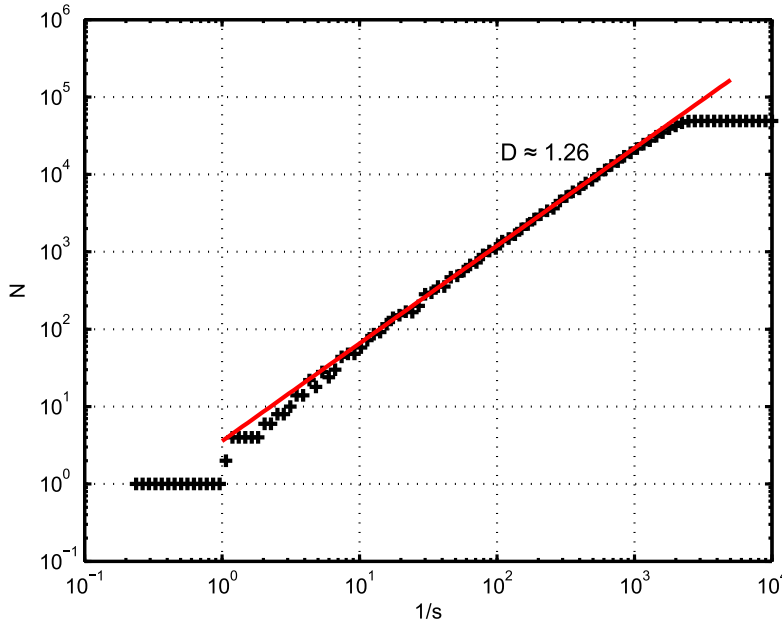

Figure 6.3: Example of how the slope that is produced by a simple box-counting algorithm can be used to determine the fractal dimension of an approximation of the Koch snowflake shown in Fig. 6.1 where only the set of corners of the snowflake are analysed ($n = 7$). Note that the value of the slope is not an integer, as opposed to the non-fractal objects in Fig. 6.2.

Starting from the left in Fig. 6.3, it can be seen that if the box size, s, is sufficiently large, only one box is needed to completely cover the snowflake. When s is decreased so that the snowflake no longer fits within a single box, the slope of the curve starts. (The reason that N at some points *decreases* with decreasing s is that, in the simple implementation that was used, the boxes are always

positioned on a rectangular grid, centred over the snowflake. This means that N is sometimes slightly larger than necessary.) Along the slope, a line with a slope of 1.26 is drawn, matching the known fractal dimension of the snowflake. The calculated slope is only reasonably linear in the approximate interval $10^2 < 1/s < 10^3$, or over about one order of magnitude, and in this range the calculations match the known slope very well. Above $1/s = 2 \cdot 10^3$ the boxes start to probe the length scale where it can be found that the object consists of points. When the boxes are as small as the points, there is no need to increase N any further; independent of how small the boxes are, it is sufficient that the boxes cover one point each. Thus the curve both starts and ends with a slope of zero.

The main points of this discussion are:

1. You must look at scales significantly smaller than the scale of the object in order to find the correct fractal dimension from the slope.

2. If you have only a limited amount of information concerning the smaller scales, this must be taken into account.

There are many other algorithms that have been designed for calculating the fractal dimension of an object [59]; they are commonly based on either the box-counting algorithm or the two-point correlation algorithm. Independent of the algorithm employed, it is important to take the finite range of self-similarity into account to obtain the correct value.

Because soot aggregates are composed of primary particles of finite size, the smaller scale limit is present in the structure itself, and is not due to any limits in experimental measurements. Also, because soot aggregates are created in a random process, they are not self-similar at different scales in the same way as the Koch snowflake is; you will never find exactly the same shape at different scales. Soot aggregates are random fractals, which means that they are only statistically self-similar [61]. When analysing the fractal dimension of soot aggregates using e.g. the box-counting algorithm it is therefore necessary to average over an ensemble of aggregates with the same structural properties to obtain a stable estimate [61].

6.2 Fractal Soot Aggregates

Soot aggregates are often modelled as N_p spherical primary particles having the radius a at locations $\mathbf{r}_i$, connected in clusters where the particles are in point

contact with each other. A measure for the length of the aggregate that is commonly employed is the radius of gyration

$$R_{\mathrm{g}} = \sqrt{\frac{1}{N_{\mathrm{p}}} \sum_{i=1}^{N_{\mathrm{p}}} (\mathbf{r}_i - \mathbf{r}_0)^2}, \tag{6.3}$$

also known as the root-mean-square radius. Here $\mathbf{r}_0$ denotes the centre of mass of the aggregate,

$$\mathbf{r}_0 = \frac{1}{N_{\mathrm{p}}} \sum_{i=1}^{N_{\mathrm{p}}} \mathbf{r}_i. \tag{6.4}$$

The fractal structure of the aggregates result in a relationship between N_{p}, a and the radius of gyration of the aggregate, often termed "the fractal scaling law",

$$N_{\mathrm{p}} = k_{\mathrm{f}} \left(\frac{R_{\mathrm{g}}}{a} \right)^{D_{\mathrm{f}}}, \tag{6.5}$$

where k_{f} is the fractal prefactor. Note that experimental results suggest that this relationship only holds on average, so that there is a variation of R_{g} for any given N_{p}; see e.g. Köylü et al. [55]. The general effect of k_{f} on an aggregate can immediately be understood from this equation: If we consider only aggregates in which N_{p}, a and D_{f} are assumed to be fixed, larger values of k_{f} correspond to aggregates having smaller values of R_{g}, the aggregates thus being smaller and denser for higher k_{f} values. However if the condition is met that $R_{\mathrm{g}} \gg a$, two aggregates with the same values of a, D_{f} and R_{g} but significantly different values of k_{f} have similar structures, because the fractal dimension is the same. Still, when viewing the aggregates at the same distance it will always be clear that one aggregate is denser than the other; even if the primary particles cannot be discerned, the total projected area of the aggregate having a larger k_{f} will be larger.

Investigations of the fractal dimension and the fractal prefactor of fractal aggregates have been carried out by use of simulations and in experimental studies; some of them have been summarized by Wu et al. [62], Köylü et al. [63] and Brasil et al. [64]. In the experimental studies, the fractal parameters are commonly determined using TEM, 3-D TEM, or elastic light scattering. Since only the two-dimensional projections of the aggregates can be found in the TEM images, the 3-D properties of the aggregates need to be calculated from

the 2-D information, see e.g. Oh and Sorensen [65] and Brasil et al. [66]. For 3-D TEM, the TEM grid is tilted in the microscope so that the projection of each aggregate can be recorded at two angles. In this way, the 3-D structure of each aggregate can be reconstructed, see e.g. [67]. When using elastic light scattering, polarized light is employed and the angular scattering can be detected. The angular scattering information can be used then to determine the fractal properties of the aggregates [68].

In most studies, the fractal dimension of the aggregates is calculated from an ensemble of aggregates, each with a different value for N_p. This is the most convenient way to do it, since the soot aggregate distribution in a flame is generally very broad. Thus, sampling the flame with a TEM probe yields aggregates with a wide distribution of sizes, and an angular scattering measurement in the flame will automatically result in information about all of the aggregates at the same time. For the TEM results, some variant of Eq. (6.5) is usually employed (together with a correction that takes the projection into account). After plotting N_p as a function of R_g/a, the fractal dimension and fractal prefactor can be found by fitting a straight line to the slope of the curve, using information from all the aggregates. D_f is found from the slope of the line while k_f is found from the position where the line crosses the N_p axis. This procedure can be compared to the box-counting algorithm described in the previous section in which the fractal dimension was found after probing a single aggregate at different scales. In a manner similar to the box-counting algorithm, the finite size of the aggregates needs to be taken into account when calculating D_f from this distribution of aggregates. The length of the slope of the log-log curve of N_p vs. (R_g/a) that can be used is limited by the largest aggregates at the upper end. I have found no studies on where to limit the slope at the lower end of the curve, although it should be above $N_p = 2$, since these aggregates cannot fulfil Eq. (6.5) for the general case.

Brasil et al. [64] made a comparison of results from simulations and experiments on soot aggregate structures. Most of the studies agree in concluding that D_f should be in the range of 1.6–1.9, whereas, for the fractal prefactor, k_f, the simulation and the experimental results show a variation of more than 200 %. In almost all the cases listed, the simulations predicted a significantly lower value of the fractal prefactor, $k_f \sim 1.3$, than was found in the experiments, that regularly resulted in values above $k_f = 2$. It has been suggested by Brasil et al. [64, 66] and Oh and Sorensen [65] that this difference could be caused by *bridging*, more than point contact between primary particles within the aggregate.

6.3 Aggregate Modelling

The aggregation construction algorithm that was used in Paper VII is based on the cluster-cluster algorithm (CCA) formulated by Filippov et al. [56]. In this algorithm, values of the fractal dimension and the fractal prefactor that have been found from experiments are used, together with the fractal scaling law, Eq. (6.5), to build fractal aggregates, starting out from isolated primary particles. Clusters having 5–8 primary particles are first created using particle–cluster aggregation, so that the clusters grow with one primary particle at a time. Each primary particle is added at a random position on the aggregate, with the constraints that the primary particles have point-contact with the aggregate, that there be no overlap with the aggregate, and that Eq. (6.5) is fulfilled after each addition. These clusters are then put together, pairwise, to build larger aggregates, still with the constraints of point-contact, no overlap and Eq. (6.5) being fulfilled. In this way, aggregates with tunable values of k_f, D_f, a and N_p can be created effectively. Some examples of aggregates created using this algorithm can be seen in Fig. 6.4. It can be seen how both k_f and D_f influences the structure of the aggregates. The top two examples show that D_f values close to one result in line-like aggregates, whereas D_f values close to three result in denser, "spherical" aggregates. (The k_f values are not the same here, because of limitations in the algorithm implementation.) The middle and bottom rows show that for aggregates with the same D_f, higher values of k_f result in denser aggregates. However, in the bottom row you can still see similarities in the overall structure, caused by the same value of D_f.

In Paper VII we investigate how bridging affects LII particle sizing. Bridging was introduced by overlapping the spheres that represent the primary particles, Fig. 6.5, the amount of bridging being quantified using the overlap parameter,

$$C_{ov} = \frac{\delta}{a}, \tag{6.6}$$

where δ is defined in Fig. 6.5. An aggregate with bridging can then be constructed easily from an aggregate with point contact, through simply increasing the radius of all the primary particles by the same factor, from a_p to $a = K \cdot a_p$, as shown in Fig. 6.6. It was argued that one reasonable way to define the fractal prefactor for the aggregate with bridging, k_f, is to obtain it from the fractal

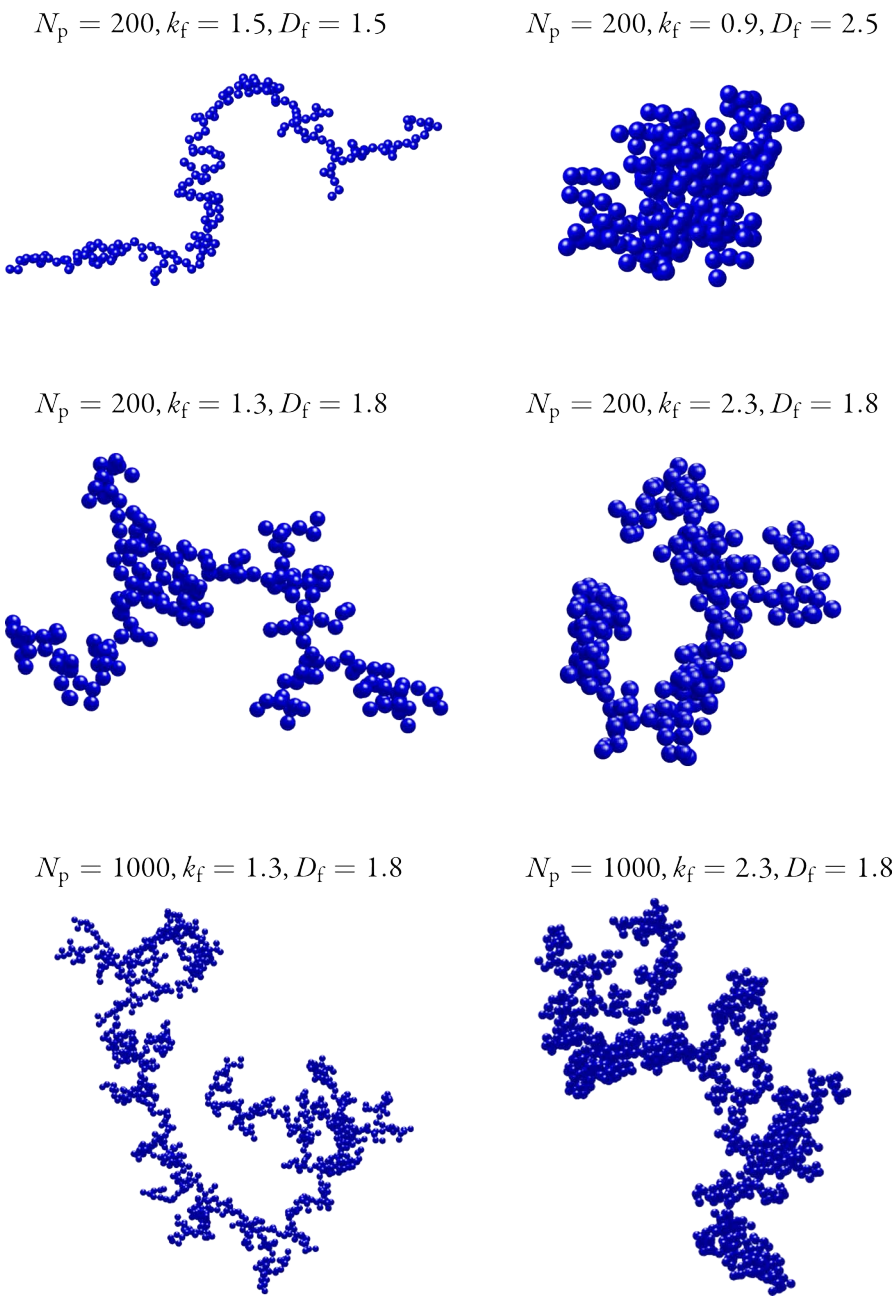

Figure 6.4: Examples of aggregates constructed using an implementation of the CCA algorithm by Filippov et al. [56]. Because only the projections of the aggregates can be shown here, the aggregates have been rotated to reveal as much detail as possible.

scaling law, Eq. (6.5), using the new particle radius a,

$$k_f = N_p \left(\frac{R_g}{a}\right)^{-D_f} = N_p \left(\frac{R_g}{K \cdot a_p}\right)^{-D_f} = K^{D_f} N_p \left(\frac{R_g}{a_p}\right)^{-D_f} = K^{D_f} k_{f,p}. \tag{6.7}$$

It can be shown that $K = (1 - C_{ov})^{-1}$ so that

$$k_f = (1 - C_{ov})^{-D_f} k_{f,p} \tag{6.8}$$

and

$$a = (1 - C_{ov})^{-1} a_p. \tag{6.9}$$

Thus, an aggregate with bridging, having the prefactor k_f and the radius a, defined as described above, can be constructed by first building an aggregate with primary particles in point contact, with a fractal prefactor and primary particle radii (from Eqs. (6.8) and (6.9))

$$k_{f,p} = (1 - C_{ov})^{D_f} k_f \tag{6.10}$$

and

$$a_p = (1 - C_{ov}) a. \tag{6.11}$$

Increasing the primary particle radii to a enables the desired aggregate with bridging to be obtained. An example comparison is shown in Fig. 6.7, in which two aggregates have been created, differing in the amount of bridging employed ($C_{ov} = 0$ and $C_{ov} = 0.25$), but otherwise involving the same parameters, as defined above.

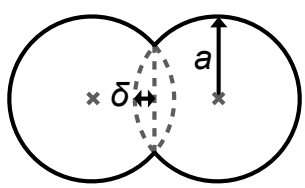

Figure 6.5: Definitions of the distances δ and a that are used to calculate the overlap parameter, C_{ov}, in Eq. (6.6).

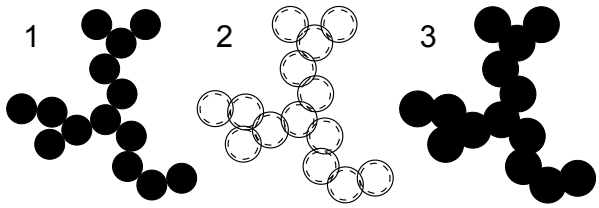

Figure 6.6: An illustration of the bridging process involving use of by overlapping spheres: (**1**) The starting point is an aggregate having primary particles in point contact. (**2**) The radii of the primary particles of the aggregate are increased in size, so that the primary particles overlap. (**3**) The union of the primary particles constitutes the aggregate with bridging. (In this two-dimensional case, $C_{ov} = 0.2$.)

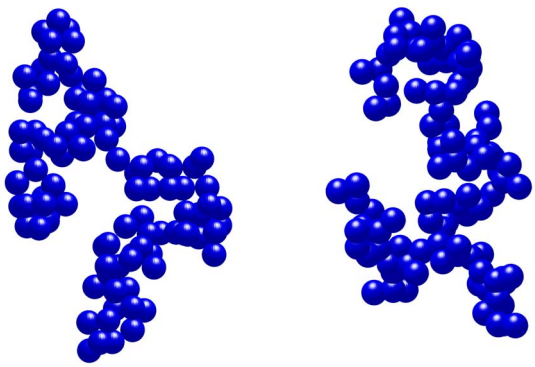

Figure 6.7: A comparison of aggregates, with and without bridging, where $N_p = 20$, $a = 10\,\text{nm}$, $k_f = 2.3$ and $D_f = 1.8$. **Left:** An aggregate with point contact between the primary particles. Since this is a projection of a three-dimensional aggregate, point contact between the primary particles can only be seen at a few places. **Right:** An aggregate with bridging; $C_{ov} = 0.25$.

6.4 Heat Conduction Modelling

LII measurements are usually made under atmospheric pressure or at higher pressure, as for example in an IC engine. As described in Section 5.1.1.1, the former condition is on the border between the free-molecular and the transition regimes, whereas the latter is within the transition regime. Thus, the ideal way to calculate heat conduction would be to take the effects introduced by the transition regime into account. However, it is more complicated to carry out the transition regime calculations, whereas the free-molecular calculations are relatively simple to perform. Since the results of the calculations in the free-molecular case can also be used to approximately calculate the heat conduction rate in the transition regime, only the free-molecular case will be discussed here.

In the free-molecular case, the heat reservoir at temperature T_g, that the aggregate of interest is suspended in, is a gas that is so dilute that none of the molecules that hit it has interacted with any other molecule for a very long distance. Thus, all these molecules approach the aggregate moving in uniformly random directions and with velocities that correspond to the Maxwell velocity distribution for the heat reservoir, completely independent of the shape or size of the aggregate. Similarly, molecules that have interacted with the aggregate surface travel a very long distance before they interact with any other molecule, so that any energy they would have gained or lost in the interaction will never have any effect on subsequent molecules that will interact with the aggregate. This means, in turn, that each molecule's collision with the aggregate is completely independent of any other molecule's collision with it, which simplifies the computer implementation of the model.

The interaction between the molecule and the surface of the aggregate can be modelled using the Maxwell kernel [46, 48, 69]. In using the Maxwell kernel it is assumed that the molecule will either completely accommodate to the surface temperature, T_p, and scatter diffusely (no preferred direction), with probability α_T, or reflect specularly without interchanging any energy with the surface, with probability $(1-\alpha_T)$. Complete accommodation here means that the molecule will leave the aggregate surface with a velocity corresponding to the Maxwell velocity distribution at the surface temperature, T_p. Other scattering kernels exist, such as the Cercignani–Lampis–Lord (CLL) kernel [70], that serve to improve the accuracy of the heat conduction calculations. This is done both by altering the probability function that is used to define the scattering direction and by accounting for different thermal accommodation for molecules that impact at different angles, and for the rotational modes of poly-

atomic molecules. However, in the present work, only the Maxwell kernel has been employed since the improvements achieved by use of the CLL kernel were relatively small [70], so that the increased accuracy was not deemed necessary for our initial studies.

The calculation of conductive heat transfer from an aggregate in the free-molecular regime can be made by use of a Monte Carlo algorithm [70]. A molecule is started from a sphere that encloses the aggregate, with the velocity $\mathbf{v}_{\text{in}}$, as sampled from the normalized distribution of velocities $\mathbf{v}$ of the molecules in the heat bath that strike a unit area per unit time [71],

$$f_{\Phi}(\mathbf{v}) \propto f(\mathbf{v}) v \cos \vartheta, \tag{6.12}$$

where $v = |\mathbf{v}|$, ϑ is the angle of incidence of the molecule, relative to the unit area normal, and $f(\mathbf{v})$ is the velocity distribution of molecules in the gas,

$$f(\mathbf{v}) \propto \left(\frac{m}{2\pi k_{\text{B}} T} \right)^{3/2} \exp\left(-\frac{m v^2}{2 k_{\text{B}} T} \right), \tag{6.13}$$

where m is the molecular weight and T is the temperature of the gas (when sampling $\mathbf{v}_{\text{in}}$, $T = T_{\text{g}}$). The molecule is then traced in a straight path until it either hits the aggregate or reaches the boundary surface. If the molecule hits the aggregate, it is assigned a new velocity, using the Maxwell kernel, where either the molecule reflects specularly or it is diffusely scattered, which is modelled by sampling a new velocity $\mathbf{v}_{\text{out}}$ from f_{Φ}, with $T = T_{\text{p}}$. The molecule is then traced until it either hits the aggregate again or reaches the boundary surface. If the molecule hits the aggregate again, a new calculation will be made for its new velocity, and so on, until the molecule finally reaches the boundary surface. In Fig. 6.8, this process is visualized. When the molecule reaches the boundary surface, the difference in its kinetic energy from start to finish is calculated,

$$\Delta E = E_{\text{out}} - E_{\text{in}} = \frac{m v_{\text{out}}^2}{2} - \frac{m v_{\text{in}}^2}{2}. \tag{6.14}$$

Since the total number of molecules that strike a unit area per unit time is known to be [71]

$$\Phi_0 = \frac{\bar{p}}{\sqrt{2\pi m k_{\text{B}} T}}, \tag{6.15}$$

where $\bar{p}$ is the mean pressure in the gas, the conductive heat transfer rate can be approximated by

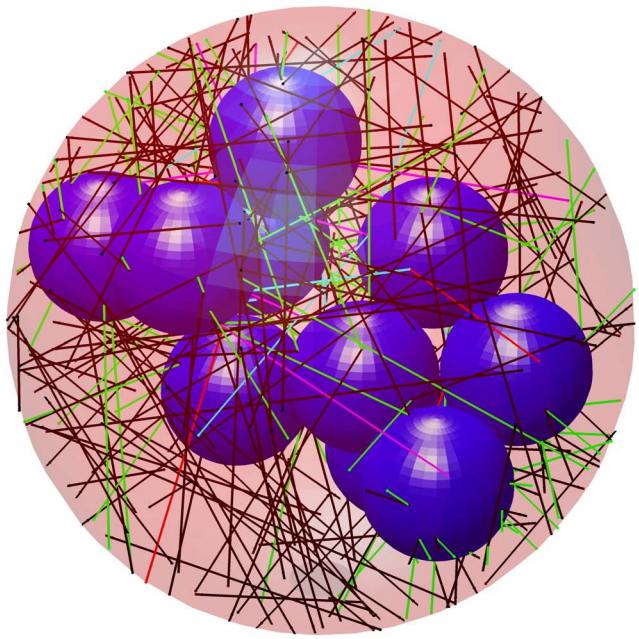

Figure 6.8: Visualization of how 200 molecules are traced, using the Monte Carlo heat conduction algorithm. The molecules start from the boundary surface, interact with the aggregate none, one or multiple times, and finally reaches the boundary surface again. Here, the colour of the traces denote how many times the molecule has collided with the aggregate (black: 0 collisions (starting from the boundary surface), green: 1, magenta: 2, cyan: 3, red: 4).

$$\dot{q}_{\text{agg}} \approx \Phi_0 A \frac{1}{N} \sum_{i=1}^{N} \Delta E_i. \tag{6.16}$$

Here, A is the area of the boundary surface, ΔE_i denotes the energy transferred by a single molecule and N is the total number of molecules that have been sent. The calculation can be made arbitrarily precise by making N sufficiently large. The shielding factor for the aggregate can then be calculated as the ratio of the aggregate heat conduction rate to the combined heat conduction rate for the primary particles, if they were located far from each other,

$$\eta = \frac{\dot{Q}_{\text{con,agg}}}{N_{\text{p}} \dot{Q}_{\text{con}}}. \tag{6.17}$$

Since we use the Maxwell scattering kernel that does not depend on the temperature of the gas or the particle and it is assumed here that α_{T} is temperature independent, η does not depend on the particle or gas temperature. The shielding factor, η, depends on the aggregate structure (defined here by the Filippov et al. [56] clustering algorithm and the fractal parameters), the choice of the scattering kernel and the thermal accommodation coefficient. A visualization of how the primary particles shield each other from the ambient gas is shown in Fig. 6.9.

Liu et al. [48] used numerically constructed soot aggregates to calculate the equivalent sphere diameter, D_{eff}, which denotes the diameter of a spherical soot particle that has the same heat conduction rate as a given aggregate. It was shown that D_{eff} could be written as

$$D_{\text{eff}} = \left(\frac{N_{\text{p}}}{k_{\text{h}}} \right)^{1/D_{\text{h}}} d_{\text{p}}, \tag{6.18}$$

where

$$\begin{aligned} k_{\text{h}} &= 1.04476 + 0.22329\alpha_{\text{T}} + 7.14286 \cdot 10^{-3}\alpha_{\text{T}}^2 \\ D_{\text{h}} &= 1.99345 + 0.30224\alpha_{\text{T}} - 0.11276\alpha_{\text{T}}^2, \end{aligned}$$

for $\alpha_{\text{T}} = 0.1 - 1.0$ and $N_{\text{p}} = 1 - 199$. In Paper VII it is shown that

$$D_{\text{eff}} = \sqrt{\eta N_{\text{p}}} d_{\text{p}}, \tag{6.19}$$

so that it is a simple matter to calculate D_{eff} from η, and vice versa, given that N_{p} and d_{p} are known.

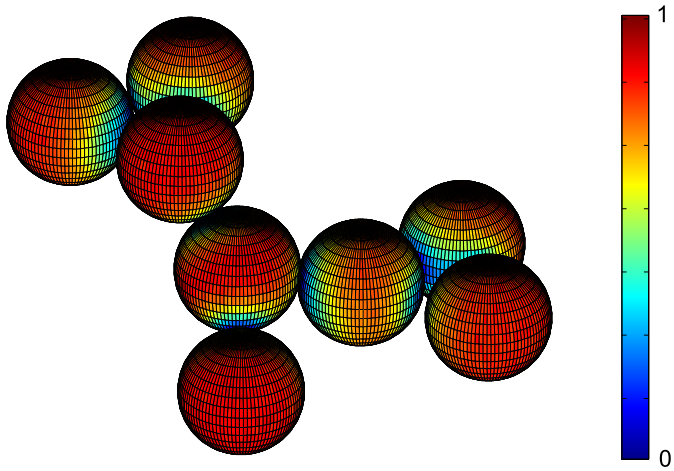

Figure 6.9: The shielding effect, visualized using the geometric accessibility of each surface element on an aggregate to the ambient gas (steradians of open view to the ambient gas/2π steradians).

6.5 LII Primary Particle Sizing for Soot Aggregates

In Chapter 5.1 the LII model for a spherical soot particle is described. Particle sizing using LII is usually made in the low-fluence regime, so that the sublimation is negligible. In this case the heat transfer equation given by Eq. (5.1) can be used, but with the sublimation term removed,

$$\dot{Q}_{\text{int}} = \dot{Q}_{\text{abs}} - \dot{Q}_{\text{con}} - \dot{Q}_{\text{rad}}. \tag{6.20}$$

To be able to use LII for evaluation of the primary particle sizes in an aggregate, this equation can be adjusted so that it instead describes the heat rates involved for an aggregate. Consider an aggregate in which the primary particles are in point contact. The internal energy is volume dependent, so the internal energy rate can be written as $N_{\text{p}}\dot{Q}_{\text{int}}$. It has been shown that the absorption cross section of an aggregate can be calculated to a good approximation as the sum of the cross sections of the constituent primary particles, if they were separated [72]. The error that is made by using this approximation has been shown to be up to about 10 % for aggregates for which $k_{\text{f}} = 2.3$, $D_{\text{f}} = 1.78$, $d_{\text{p}} = 30$ nm and $N_{\text{p}} \leq 1000$ [72]. Thus, the absorption and radiation heat transfer rates can be written as $N_{\text{p}}\dot{Q}_{\text{abs}}$ and $N_{\text{p}}\dot{Q}_{\text{rad}}$, respectively. As was described in the previous section, the shielding that affects the heat conduction rate from a soot ag-

gregate depends on the aggregate shape, the scattering kernel and the thermal accommodation coefficient. In the free-molecular regime, the heat conduction rate can be written using the shielding factor, as $N_\mathrm{p}\eta\dot{Q}_\mathrm{con}$, by simply rearranging Eq. (6.17). The heat transfer equation for a soot aggregate in the free-molecular regime can thus be written

$$N_\mathrm{p}\dot{Q}_\mathrm{int} = N_\mathrm{p}\dot{Q}_\mathrm{abs} - N_\mathrm{p}\eta\dot{Q}_\mathrm{con} - N_\mathrm{p}\dot{Q}_\mathrm{rad}. \tag{6.21}$$

For the transition regime, the heat conduction term can be calculated using the Fuchs model, described in Section 5.1.1.1, using the equivalent sphere diameter, D_eff, (Eq. (6.19)) serving as the particle radius. This is currently the default setting for our LII model, and is used in Papers I and V.

Because the heat conduction in the Fuchs model cannot be described using a closed-form analytical expression, it is more difficult to get an intuitive understanding of the effect of aggregation on the heat transfer equation when discussing the free-molecular regime. However, the main qualitative insights that are discussed here do, to a good approximation, also hold also for the transition regime. For more information on how to use the Fuchs model for aggregates with bridging, see Paper VII.

If the aggregate has some bridging between the primary particles, modelled by overlapping spheres as described in Section 6.3, and we want to keep thinking of the aggregates as a cluster of spheres with radius d_p, this needs to be taken into account in the heat transfer equation, since the mass of an aggregate with given N_p and fractal parameters will decrease with an increase in the overlap factor, C_ov. The relative reduction in mass can be described by

$$\gamma_\mathrm{ov} = \frac{V_\mathrm{agg}}{N_\mathrm{p}\dfrac{\pi d_\mathrm{p}^3}{6}}, \tag{6.22}$$

where V_agg is the volume of the aggregate and $d_\mathrm{p} = 2a$. Note that in general γ_ov is different for every aggregate, because all of them have different random configurations. The generalized heat transfer equation, holding both for aggregates with point contact and with bridging, in the free-molecular regime, can now be written as

$$N_\mathrm{p}\gamma_\mathrm{ov}\dot{Q}_\mathrm{int} = N_\mathrm{p}\gamma_\mathrm{ov}\dot{Q}_\mathrm{abs} - N_\mathrm{p}\eta\dot{Q}_\mathrm{con} - N_\mathrm{p}\gamma_\mathrm{ov}\dot{Q}_\mathrm{rad}. \tag{6.23}$$

The RDG theory [72] is used in this case as well and is assumed to be a reasonable approximation, based on the fact that the structure of an aggregate with

bridging is similar to a corresponding aggregate with point contact. Equation (6.23) reduces to Eq. (6.21) when $\gamma_{ov} = 1$, so that it also works for aggregates with point contact.

Equation (6.23) can be rearranged into

$$N_p \dot{q}_{int} = N_p \dot{q}_{abs} - N_p \left(\frac{\eta}{\gamma_{ov}} \right) \dot{q}_{con,FM} - N_p \dot{q}_{rad}, \tag{6.24}$$

which shows that the total effect of bridging on the decay rate of the particle temperature can be described using a single value, η/γ_{ov}. This value can be useful in providing an approximate indication of how much the evaluated primary particle size would change with bridging, as long as η/γ_{ov} is small.

Chapter 7

Results

The seven articles included in the thesis deal with various problems and questions regarding both the LII measurement technique and the properties of soot particles in flat flames. The summaries of the papers are divided into two subsections. In the first subsection the papers concerned with the development of LII, Papers I–III, V and VII, are discussed. In this part, results of measurements in the carbon black distributor (Section 2.3) are also taken up. In the second subsection the papers related to soot properties in the flat flame on a McKenna burner, Papers IV and VI, are discussed.

7.1 Development and Analysis of LII

7.1.1 Signal Relation to Soot Volume Fraction

In 1984, Melton [29] derived an expression that relates the peak-integrated LII signal, S_{int}, to the primary particle diameter, d_{p}, in the limit of high laser power,

$$S_{\text{int}} \propto d_{\text{p}}^{x}, \tag{7.1}$$

where

$$x = 3 + \frac{0.154 \cdot 10^{-6}}{\lambda}. \tag{7.2}$$

If the approximation that $x \approx 3$ is employed, Eq. (7.1) becomes

$$S_{\text{int}} = C \cdot f_{\text{v}}, \tag{7.3}$$

where f_{v} is the soot volume fraction and C is a constant. This expression has been employed extensively in soot volume fraction experiments involving use of LII; see Section 3.1.

In Paper I in this work, a theoretical investigation was carried out concerned with how accurate Eq. (7.3) is under various experimental conditions. Since C is not a constant in reality, it will henceforth be termed the proportionality parameter. Following the approach outlined by Seitzman et al. [73], the investigation involved first finding the proportionality parameter, $C(d_\mathrm{p})$, for each of the particle diameters in a specified range, and then calculating the error of C as a function of d_p, using $C(d_\mathrm{p} = 30\,\mathrm{nm})$ as the reference point. Corresponding time-resolved tests were also carried out, to determine how the errors in C varied over time. The error for the time-integrated LII signal is defined as

$$\varepsilon = \frac{C_\mathrm{test} - C_\mathrm{ref}}{C_\mathrm{ref}}, \tag{7.4}$$

where

$$C_i = \frac{\int_{t_1}^{t_2} S(t)\,dt}{\frac{\pi}{6} N_\mathrm{p} D_0^3} \left(\equiv \frac{S_\mathrm{int}}{f_\mathrm{v}} \right). \tag{7.5}$$

$S(t)$ is the time-resolved LII signal, N_p is the number of primary particles within an aggregate, and D_0 is the primary particle diameter before the particle has been affected by the laser beam. This means that if the parameter C is known at some point in an LII measurement image, the evaluation of the soot volume fraction at another point in the image, using this parameter and Eq. (7.3), results in an over- or underprediction of the soot volume fraction in that point, by an amount given by the error, ε. The corresponding error for the time-resolved LII signal is defined similarly,

$$\varepsilon'(t) = \frac{C'_\mathrm{test}(t) - C'_\mathrm{ref}(t)}{C'_\mathrm{ref}(t)}, \tag{7.6}$$

where

$$C'(t) = \frac{S(t)}{\frac{\pi}{6} N_\mathrm{p} D_0^3}. \tag{7.7}$$

Here, $\varepsilon'(t)$ is the time-resolved error in the time-resolved proportionality parameter $C'(t)$.

One way of more easily understanding some of the qualitative results in the paper is to keep in mind that the reason for Eq. (7.3) being approximately correct is that the particles are both volume absorbers and volume emitters. The absorption and the emission terms are the only ones in our LII model that are particle-volume dependent, whereas in contrast the heat conduction and sublimation terms are approximately particle-surface-area dependent. Thus, for

most of the sets of parameters involved, it holds that the less that heat conduction and sublimation come into play, the more correct Eq. (7.3) will be.

The paper is rather comprehensive, calculations of the diameter-dependent errors having been carried out for the integrated and time-resolved LII signals obtained at several different parameter settings. The base case model for all comparisons in the paper is presented in Table 7.1.

Table 7.1: The base case used for the tests in Paper I.

Properties of the laser pulse	
Wavelength	1064 nm
Temporal profile	Gaussian with FWHM 8 ns
Spatial profile	Top-hat
Fluence	0.1 and 0.4 J/cm^2
Properties of the detection system	
Gate timing	20 ns centred on the laser pulse
Spectral	Single wavelength at 500 nm
Properties of the measurement volume	
Pressure	0.1 MPa
Temperature	1800 K
Aggregation	No
Primary particle size	Monodisperse distribution

Examples of the results taken up in the paper are shown in Fig. 7.1: At the top left, the differences between the model results and Melton's predictions, Eq. (7.1), are plotted as a function of the detection wavelength. Also shown, at the top left, is a straight reference line corresponding to the case in which $x = 3$ in Eq. (7.1). Note that Melton's expression gives results very similar to the model results, and that results for both deviate more from a linear relationship between signal and soot volume fraction the shorter the detection wavelength is. At the bottom left, the same model calculations have been carried out, but there the gate in the model has been delayed 100 ns, the linearity assumption, Eq. (7.3), in that case, resulting in much larger errors.

At the right in Fig. 7.1, two of the error plots from the paper are shown, the upper involving the time-integrated error, C, and the lower the time-resolved

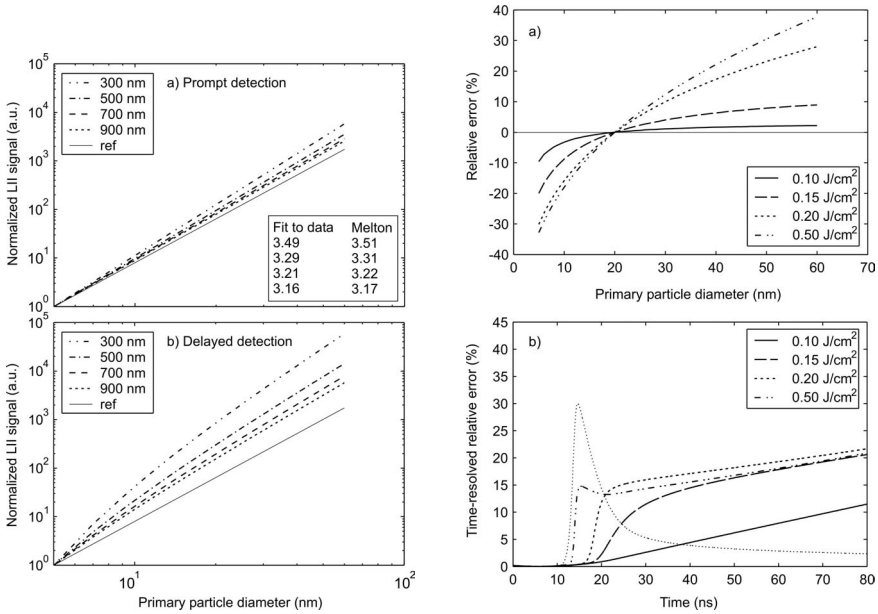

Figure 7.1: Left: Assessment of Melton's expression, Eq. (7.1), by comparing it to the results from our LII model at different wavelengths at a prompt gate (top) and a 100 ns delayed gate (bottom). Also shown are references lines corresponding the exponent $x = 3$ in Eq. (7.1) **Right:** The relative error introduced in the evaluated soot volume fraction if the linear dependence between soot volume fraction and LII signal is assumed. The relative error is plotted as a function of primary particle size and laser fluence, for the base case. It can be seen that the relative error is larger for larger fluences.

error, $C'(t)$. These plots allow the effects of different laser fluences to be assessed. In the upper plot there at the right it can be seen that for larger fluences the relative error becomes larger, and that how much larger it becomes depends on how different the actual particle size in the probe volume is, as compared with the particle size at the calibration point (chosen at 20 nm). In the lower plot, the time-resolved error obtained for a particle with a size of 30 nm is shown relative to the reference particle size of 20 nm. There, the error is larger in connection with larger fluences. As can be seen, the error level for each of the fluence levels except 0.50 J/cm^2 are relatively small at the beginning of the signal. This is due to none of the surface-area dependent heat transfer terms having had an appreciable effect at that point, the particle temperatures being below the sublimation threshold and the heat conduction being relatively weak compared with the laser absorption. At a high fluence level, 0.50 J/cm^2, the error has already become relatively large even before the peak of the signal is reached, due to the strong surface-area-dependent sublimation of the particles there.

At the end of the paper, error estimates are provided for a more complex case in which a number of the parameters involved are uncertain. This would be the case in a real-world measurement situation. In the case chosen, the overprediction of the soot volume fraction could be approximately a factor of two if the size dependence of the signal were not taken into account. (The calibration point was in a 20 nm region, the measurements being made in a 60 nm region here.)

A number of conclusions were drawn in the paper, various of them summarised here. The linearity statements are related to Eq. (7.3).

- The linear relationship between the LII signal and the soot volume fraction can be increased by using short prompt gates and longer detection wavelengths.
- In atmospheric flames, the effects of particle size on the linearity here were found to be small in the low-fluence regime, and to be more noticeable in the high-fluence regime.
- The spatial beam profile of the laser was shown to affect the linearity only slightly.
- At high pressures and in the high-fluence regime, use of a short prompt gate is to be recommended, since the sublimation process competes with the heat conduction process there, effectively reducing the effects of the pressure during the first 10–15 ns of the signal.

- The aggregation of particles has little effect on the linearity found under high fluence conditions, the effect being greater in the low-fluence regime.
- When the ambient temperature is decreased, the non-linearity increases.
- Low-fluence LII under atmospheric flame conditions results in a relatively high degree of linearity between the signal and the soot volume fraction, as compared with use of high-fluence LII. However, the sensitivity of the signal to pulse-to-pulse fluctuations in the laser energy, together with beam attenuation, makes low-fluence LII less useful for visualisation purposes under practical conditions.
- If it is possible to extract particle size information simultaneously with the carrying out of LII measurements, information from the model can be used to compensate for the errors found in using Eq. (7.3).

7.1.2 Effect of the Laser Beam Profile on the Evaluated Particle Size

In the theoretical considerations regarding which laser beam profile should best be used for particle sizing in the use of LII (Section 5.4), it was found that a tophat profile is to be preferred. An advantage in the use of a tophat profile is that the soot particles within the measurement volume are all heated then to approximately the same temperature. Since this temperature can be measured using pyrometry, the evaluation can start just after the end of the laser pulse, using the measured temperature as the initial value. In this way the uncertainties in the absorption term of the model can be avoided.

In Paper II, we were interested in how different the results of a particle size evaluation using a nonuniform profile would be as compared with the results obtained using a tophat profile. The tophat profile was created by cutting out the central part of the laser beam and imaging it into the measurement volume; Fig. 4.1. The nonuniform profile, in turn, was created by placing a small pinhole close to the focal planes of the lenses in the imaging system, so that many of the higher spatial frequency components in the tophat profile were removed. The respective profiles and the corresponding histograms are shown in Fig. 7.2.

One set of measurements was made for each profile, within a premixed ethylene/air flame with a nitrogen co-flow on a McKenna burner at $\Phi = 2.1$, at 10, 12 and 14 mm above the burner. Two types of evaluations were then carried out for both of sets of measurements. First, evaluations of all the signals

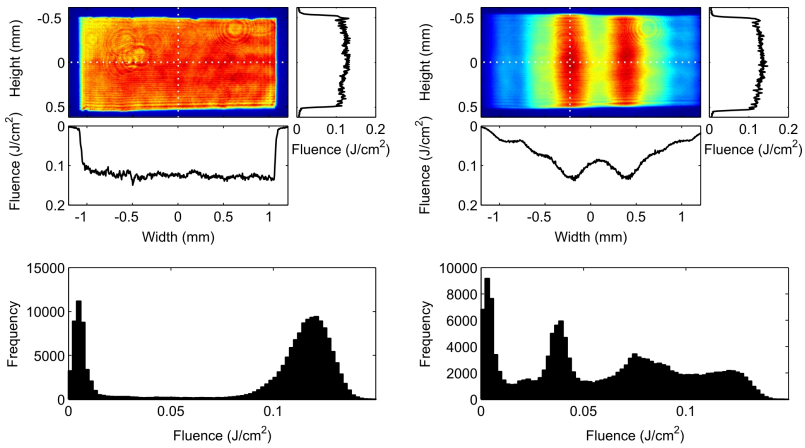

Figure 7.2: Top: Images of the rectangular tophat and the nonuniform profiles used in Paper II. **Bottom:** The fluence histograms corresponding to the profiles above.

were carried out as if a perfect tophat laser profile were being used, to determine whether it is important to take the profile into account during evaluation. Secondly, evaluations of all the signals were carried out using the measured beam profiles in the model, in order to determine whether this would make the results of the evaluations more similar. It was expected that results of the former evaluations would be different for the two cases, due to the signals being created using different beam profiles. It was reasoned that the differences between the results in the case of the latter evaluations should be considerably less, since there the different profiles are taken into account. Since the thermal accommodation coefficient, α_T, that is involved in the cooling rate of the particles, was not known for the experimental conditions, a transmission electron microscope (TEM) was used to measure the particle sizes. The sizes acquired using TEM were then used to select the best value for α_T. Since the aim of these measurements was to determine the effect of the spatial profile on the evaluated sizes, the use of a different method for determining the thermal accommodation coefficient is no disadvantage.* Rather, it helps define the experimental environment by providing complementary particle size information, and making it possible to determine how closely the sizes found by means of LII and by means of TEM correlate with each other.

*If only LII were used to measure the particle sizes in a given combustion process, the value of the thermal accommodation coefficient would need to be selected from prior measurements or calculations made under similar conditions.

The results of the evaluations (Fig. 7.3) show that the effect of the spatial profile on the evaluated particle size is relatively small in this case. The results of evaluating the signal from the nonuniform profile differs by less than 18 % in both cases. The reason for the relatively small difference here may be that the radiation from the particles that are affected by the strongest fluences have a much larger effect than those affected by the lower fluences, the peak fluences being approximately the same for the two profiles. As expected, the evaluated particle size from the tophat signals differs from that obtained from the nonuniform signals, when both are evaluated as if they were induced by an ideal tophat. However, the difference does not decrease overall when the profile is used as input to the model, as one might expect, but only for the signal from 10 mm above the burner. The reason for this is not clarified, yet since the nonuniform profile requires the model to output a weighted signal from particles heated to different temperatures, it is reasonable to expect that any errors introduced due to uncertainties in the LII model or in its parameters will be amplified as compared with the simple tophat case.

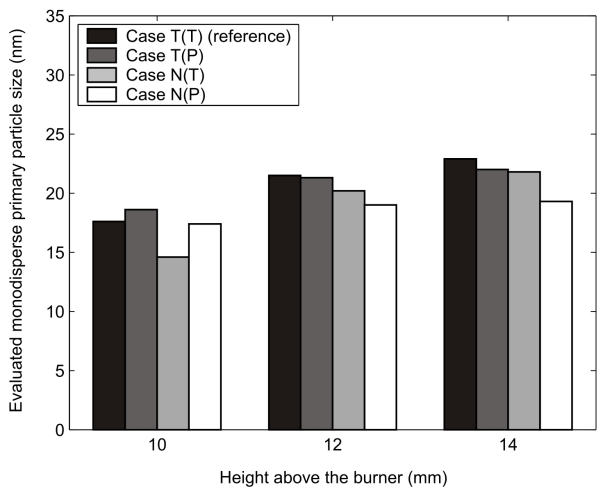

Figure 7.3: The evaluated monodisperse particle size for the tophat case, T(x), and the nonuniform case, N(x), where x=T means that the evaluation was carried out assuming that the spatial profile of the laser beam was an ideal tophat, whereas x=P means that the profile that was measured in the experiment was used as input to the model during the evaluation.

7.1.3 The Effect of Bimodal Lognormal Distributions on Unimodal Evaluation

It has been shown that soot particle distributions in combustion processes are sometimes bimodal [74,75]. Bimodal lognormal distributions represent these distributions quite accurately. The distributions are constructed by simply weighting and adding two lognormal functions differing in the geometrical diameters and the geometrical standard deviations involved. Our group found there to be a large number of small but diffuse particles in the TEM measurements of soot presented in Paper II. Since these particles might possibly be explained by a mode of smaller particles in the size distributions, we decided to assess the effect of a bimodal lognormal size distribution on evaluations in which the distribution is assumed to be unimodal, i.e. to involve a monodisperse or a lognormal distribution. Paper III is primarily concerned with these investigations. The bimodal lognormal size distribution, $p_{\mathrm{b}}(d_{\mathrm{p}})$ was defined (cf. Eq. (5.21)) as

$$p_{\mathrm{b}}(d_{\mathrm{p}}) = w_1\, p_1(d_{\mathrm{p}}, d_{\mathrm{g1}}, \sigma_{\mathrm{g1}}) + w_2\, p_2(d_{\mathrm{p}}, d_{\mathrm{g2}}, \sigma_{\mathrm{g2}}) \tag{7.8}$$

where d_{g1} and d_{g2}, σ_{g1} and σ_{g2}, and w_1 and w_2 are the geometric mean particle diameters, the geometric standard deviations, and the weights of the (normalised) small-size mode, p_1, and the large-size mode, p_2, respectively. (For the definitions of p_1 and p_2, see Paper III.)

Three types of evaluations were carried out. In the first, a bimodal lognormal size distribution similar to one measured by Stirn et al. [75] was employed. The bimodal distribution we chose was measured under experimental conditions that were very similar to our measurements in Paper II at 10 mm above the burner. Stirn et al. [75] acquired this size distribution using a scanning mobility particle sizer (SMPS, see Section 3.3), that was sensitive to very small particles. The height of 10 mm above the burner was selected, since the particles were not expected to be aggregated to any marked degree at this height. It was important to employ data for non-aggregated particles, since we wanted to be able to use a particle size distribution obtained using SMPS, and to employ it in the LII model, the methods involved resulting in different effective diameters if the particles were aggregated.

The bimodal distribution was employed to create a signal by using the LII model. The signal was then evaluated, first by use of a monodisperse (single particle size) fit, and second by use of a lognormal distribution. The results are shown in Fig. 7.4. It is evident there that in this case the small-size mode of the bimodal distribution has only a slight effect on the evaluated lognormal distri-

bution. The evaluated lognormal distribution was close to the large-size mode in the bimodal distribution, and had shifted only slightly towards the small-size mode. The effect of the small-size mode on the monodisperse evaluation was found to be even less: the evaluated monodisperse size being practically the same when the signal from the bimodal distribution was employed as when only the large mode of the bimodal distribution was used to create the original signal.

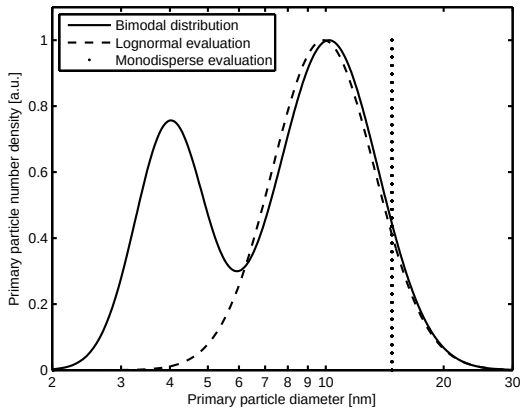

Figure 7.4: The solid curve shows a bimodal lognormal size distribution used in the LII model to calculate a signal that could be evaluated. The dashed curve shows the distribution obtained, when the signal was evaluated as if it originated from a lognormal distribution. The vertical dashed line shows the particle size obtained when it was assumed that the signal originated from a monodisperse (single-size) distribution.

In the second test, a parameter study was carried out. A bimodal lognormal distribution was created, the parameters of the large-size modes being fixed at d_{g2} = 11.0 nm and σ_{g2} = 1.3, whereas for the small-size modes only the geometrical width was fixed, where σ_{g1} = 1.3. The weight, w_1, and the geometrical mean diameter, d_{g1} (the "position") of the small-size mode were allowed to vary within limits set to values corresponding approximately to those found experimentally by Wang and Stirn [74, 75]. Signals were created from these

distributions, a range of different weights and geometrical mean values being used for the small-size mode, the LII model being employed. The signals were evaluated under the assumption that the particle distribution was monodisperse, the evaluated sizes being shown in Fig. 7.5. As can be seen, the effect of the small-size mode on the evaluated size only becomes noticeable when the weight of the small-size mode is relatively large.

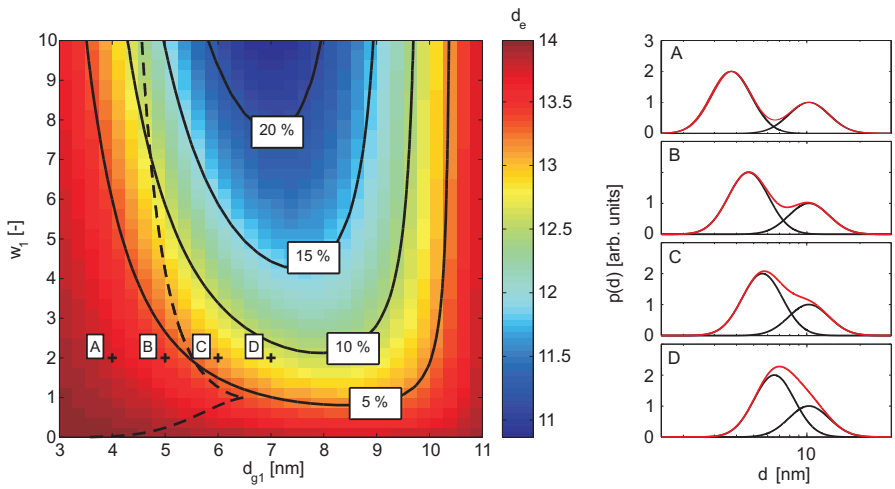

Figure 7.5: Left: The monodisperse sizes, d_e, evaluated from signals created from bimodal lognormal distributions having different values for d_{g1} and w_1. The solid black lines are contour lines showing the deviation from the evaluated monodisperse size of the large-size mode. The dashed black line shows where the minimum between the peaks of the bimodal distribution disappears in moving from left to right in the figure. **Right:** Four plots showing how the shape of the bimodal distribution changes when $w_1 = 2$ and d_{g1} increases, as marked in the left plot. In each plot both the individual modes and the total distribution are shown.

Since the smaller particles cool faster than the larger ones, their effect on the LII signal decreases over time when the signal decays. To test how this would affect the overall results, the monodisperse particle size was evaluated for the signal from the bimodal distribution, using a range of different start times. It

was found that the evaluated monodisperse size is larger, the later the start time is. This is consistent with the fact that the smaller particles cool faster.

The main result of the study reported in this paper was that the small-size mode of a bimodal lognormal distribution appears to have a small effect on the evaluated size distribution, if the distribution is assumed to be monodisperse or lognormal. Also, it is important to start the evaluation not longer after the signal peak is reached, if the smaller particles that the distribution contains are of interest.

7.1.4 Measurements in a Flame-based Soot Generator

Paper V deals with the results of a collaborative study by our group and a group from the Division of Ergonomics and Aerosol Technology (EAT) of Lund University. The work involved measurements obtained in the flame-based soot generator described in Section 2.3.3. The sizes of the soot particles in the exhausts from the soot generator were measured by use of an SMPS and a DMA-APM (see Section 3.3) by the EAT group, and by use of LII by our group. The aim of these joint measurements was to carry out a preliminary investigation of how the results the different methods provide are related to one another.

Three cases, A–C, differing in their settings on the soot generator, were selected. The SMPS measurements were used to ensure the stability of each of the emitted soot distributions (Fig. 7.6). The SMPS results showed the mobility diameter distributions in A–C to shift towards larger diameters, this being found to correlate with the trend in the TEM images (Fig. 7.7) where it can be seen that the level of aggregation increases noticeably from case A–C. At the same time, the histograms of the primary particle sizes, extracted from the TEM images, showed the primary particle sizes to remain approximately the same for all three cases. This suggested the differences in time decay for the LII signals one can note in Fig. 7.6 to be due to the differences in aggregation levels that were found. Since the signal decay is larger for the more aggregated cases, the sensitivity of the LII signal to the degree of aggregation can be attributed to the shielding effect that exists in the more aggregated particles.

The LII model described in Section 6.5 was used to verify the preliminary assumption we made of the only small differences found in the primary particle distributions being unable to explain the large difference in decay rate found for the LII signals. Combining the TEM and the DMA-APM data made it

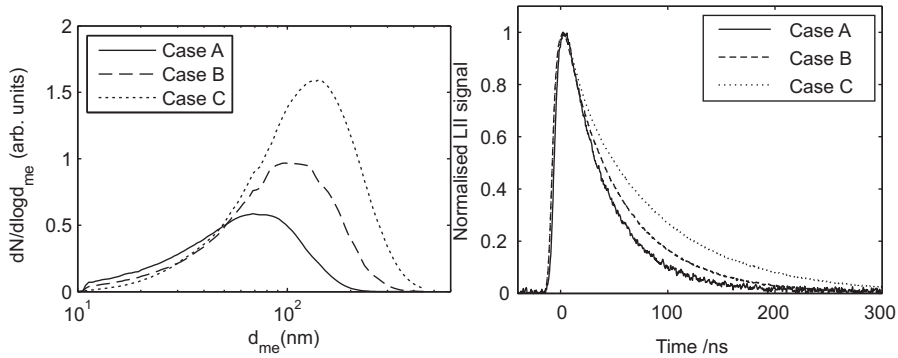

Figure 7.6: Measurements of three different soot distributions produced by the flame-based soot generator. **Left:** Mobility diameters as measured using the SMPS. **Right:** Shot-averaged, normalised LII signals.

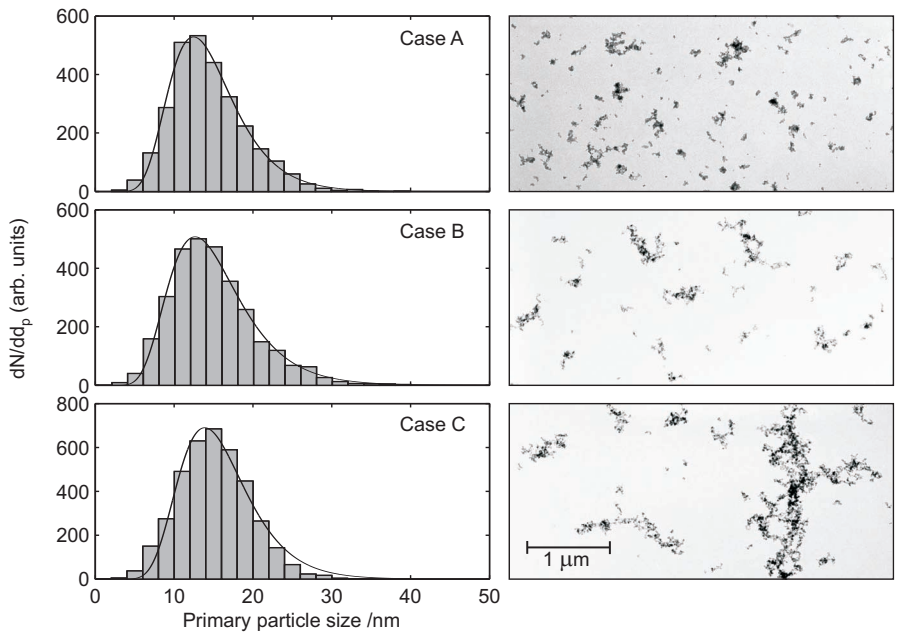

Figure 7.7: TEM images of the soot distributions, together with histograms of the primary particle sizes as extracted from the images.

possible to determine the aggregate size distribution (Fig. 7.8). Using this distribution in the LII model indicated the LII signals to differ markedly in decay rate, but did not replicate the large difference found in the experimental LII signals. For a detailed discussion of these discrepancies, see Paper V.

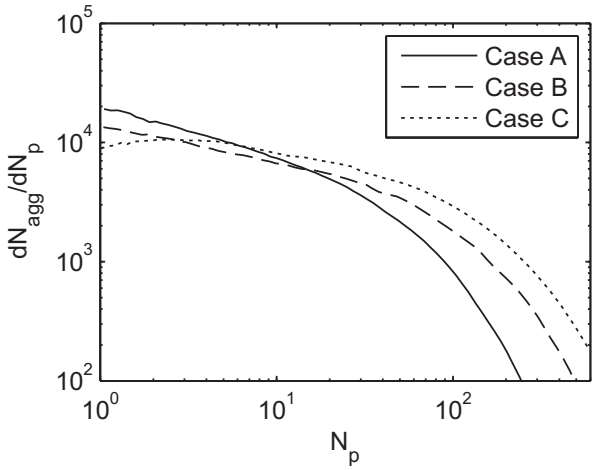

Figure 7.8: Aggregate size distributions obtained by combining the TEM and DMA-APM data.

7.1.5 The Effects on LII of Aggregates with Bridging

Soot aggregates are often modelled as consisting of a number of spherical soot primary particles connected through being in point contact with one another to form ramified, fractal clusters. It is also well-known that the primary particles are connected at more than single points, i.e. that there is certain *bridging* (also termed *necking*) between the primary particles. An example of an aggregate with a significant degree of bridging is shown in Fig. 7.9. A simple way of investigating the possible effects of bridging on various experimental procedures undertaken, such as particle size characterization on the basis of TEM images and heat conduction calculations on numerically constructed aggreg-

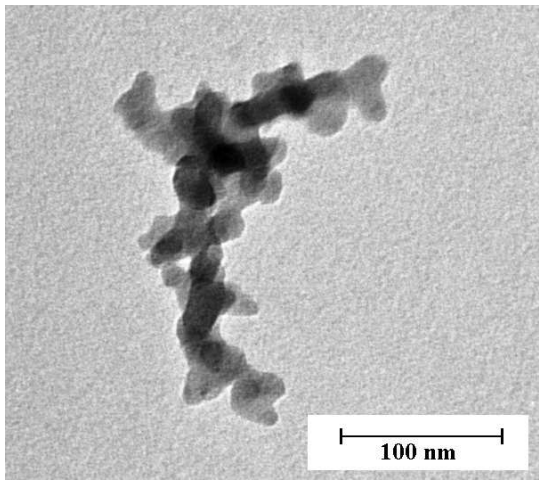

Figure 7.9: An example of an aggregate from a premixed ethylene/air flame, in which bridging can be seen between the primary particles.

ates, is to model the bridging by use of overlapping spheres. Exactly how this bridging is done is described in Section 6.3, and in more detail in Paper VII.

One of the objectives in Paper VII was to investigate how bridging affects the particle sizes as evaluated on the basis of the LII signals. Aggregates having point contact and bridging (C_{ov} values of 0.125 and 0.25, respectively) between the primary particles were constructed numerically, with fractal parameters $k_f = 2.3$ and $D_f = 1.8$, and the sizes $N_p = \{5, 10, 20, 50, 100\}$. The shielding factor, η, was then calculated, for conditions both of full thermal accommodation and of more realistic thermal accommodation, one of $\alpha_T = 0.37$ [18]; see Fig. 7.10. In the figure, an appreciable effect of bridging on η can be seen, especially at $\alpha_T = 0.37$. The shielding factor was found to decrease as the amount of bridging increased. This was expected due to the surface area of the aggregate being reduced under such conditions.

Looking at the changes in η alone is not sufficient, however, for obtaining an adequate understanding of how large the effect on the decay of the LII signals, and thus on the evaluated primary particle size, will be. A better estimate can be obtained by also taking the difference in mass between the aggregates showing point contact and bridging, γ_{ov}, into account, and looking at η/γ_{ov}, as taken up in Section 6.5. This latter ratio is plotted in Fig. 7.11, where it can be seen that the effect of bridging is reduced as compared with that shown in Fig. 7.10. The reason for this reduction occurring can be understood by recognizing the

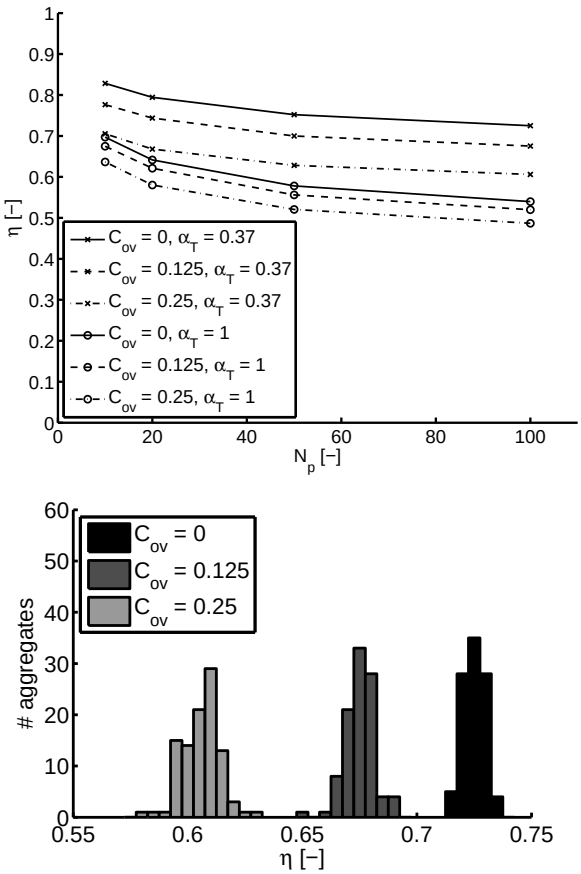

Figure 7.10: a) Shielding factors in the free-molecular regime, shown for thermal accommodation coefficients of $\alpha_T = 0.37$ and $\alpha_T = 1$. The aggregates were created for $k_f = 2.3$ and $D_f = 1.8$, and the sizes $N_p = \{5, 10, 20, 50, 100\}$, and for $C_{ov} = 0$, 0.125 and 0.25. Each point indicates the mean shielding of 100 aggregates of the type involved. **b)** Histograms of η for the 100 aggregates for which $N_p = 100$ and $\alpha_T = 0.37$.

fact that increasing C_{ov} while keeping all other the parameters fixed not only leads to a smaller surface area but also to particles having less mass to cool.

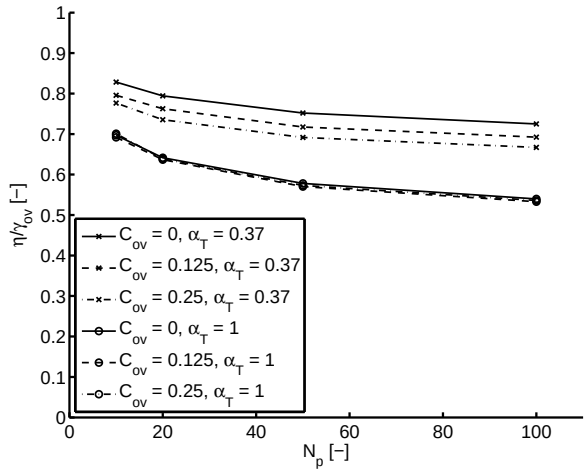

Figure 7.11: The shielding factor divided by the reduction in volume, (η/γ_{ov}), shown for the same aggregates as in Fig. 7.10. Note that this ratio is less affected by the bridging than by the shielding itself.

Calculations of how large the error in the evaluated primary particle size was when the aggregates producing the LII signals had bridging of a specific degree were carried out, point contact between the primary particles being assumed. The aggregate parameters were $k_f = 2.3$, $D_f = 1.8$, $d_p = 20$ nm, $N_p = 100$ and $C_{ov} = 0$, 0.125 and 0.25. The calculations were carried out then in the transition regime, using the modified LII model described in Section 6.5, and ambient gas temperature T_g of 1800 K. The thermal accommodation coefficient was set to $\alpha_T = 0.37$ [18] and the absorption function to $E(m) = 0.4$ (Paper IV). The spatial profile of the laser was a tophat, and the laser wavelength, the pulse duration (Gaussian FWHM) and the fluence were set to 1064 nm, 10 ns and 0.1 J/cm^2, respectively. Detection was carried out at 445 nm and 575 nm, the detector being assumed to have a rise time sufficiently short to not affect the shape of the signals that were detected. The calculated LII signals at 575 nm are shown in Fig. 7.12, in which the peak of the laser

pulse is at 50 ns and the signal is calculated for 1500 ns. The LII signal from an isolated primary particle is also shown for comparison purposes.

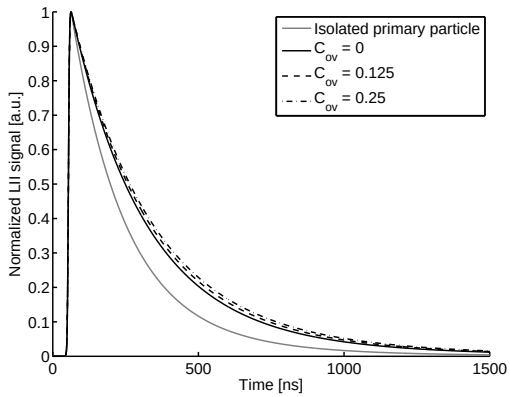

Figure 7.12: Theoretically calculated LII signals for $\alpha_T = 0.37$ ($k_f = 2.3$ $D_f = 1.8$, $d_p = 20$ nm, $N_p = 100$, $C_{ov} = 0$, 0.125 and 0.25). The signal from an isolated primary particle is shown for reference purposes.

The fitted primary particle diameters for the aggregates for which $C_{ov} = 0.125$ and 0.25 ($d_p = 20$ nm) were found to be overestimated by 5 % (21.0 nm) and 9 % (21.7 nm), respectively, when point contact was assumed. For comparison purposes, the signals for the aggregates for which $C_{ov} = 0$, 0.125 and 0.25 and $N_p = 100$ were evaluated, the primary particles being assumed to be isolated ($N_p = 1$). This resulted in overestimations of the primary particle diameters of 39 % (27.7 nm), 45 % (29.0 nm) and 51 % (30.1 nm), respectively. Thus, there was found to be a noticeable effect of bridging on the evaluated primary particle size, although this effect was much less than it would have been if aggregation had not been taken into account at all during evaluation.

It is important to bear in mind that such comparisons can only be said to hold when the definitions of the primary particle radius and of the fractal prefactor for the aggregates with bridging that were described in Section 6.3 are employed.

7.1.6 Measurements of Carbon Black

LII particle size measurements in the carbon black distributor were carried out (see Section 2.3.2), as a part of Nils Hernäng's master thesis project [22]. Four different standard samples of carbon black (Standard Reference Blacks, SRB A6, C6, E6 and F6) were involved. The standard carbon black samples were defined using different oil-adsorption methods, these measuring among other things the surface area of the particles. All of the samples consisted of large, massively aggregated soot primary particles of a wide range of different sizes, as can be seen in the TEM images in Fig. 7.13.

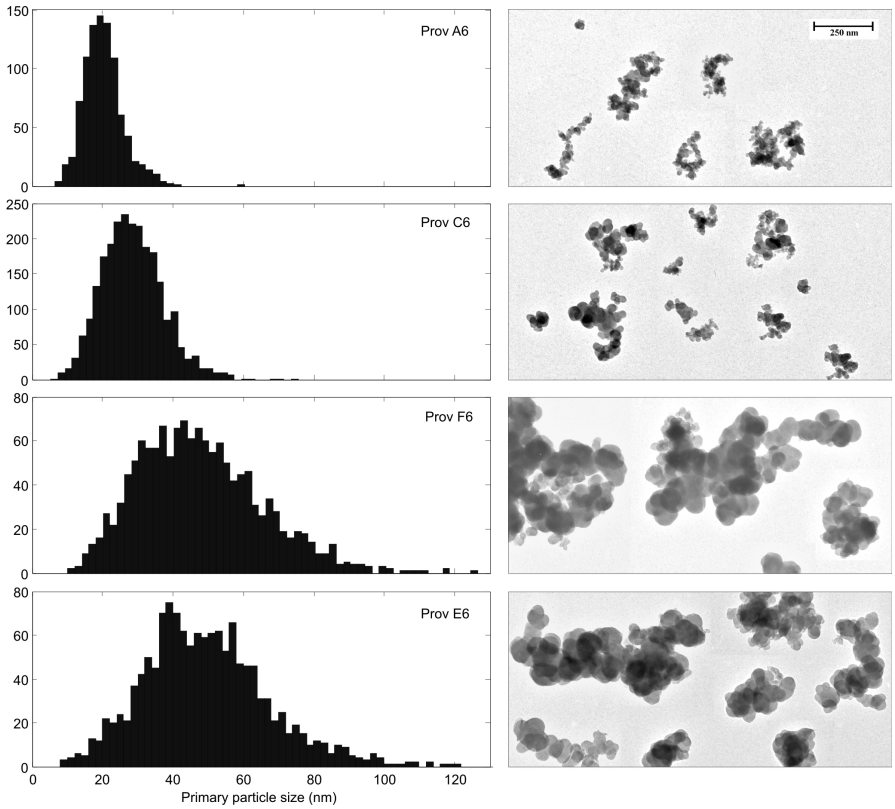

Figure 7.13: TEM evaluations of carbon black standard types SRB A6 C6 E6 and F6. **Left:** Histograms of the primary particle sizes in the images. **Right:** Examples of carbon black soot particles for the different types.

To obtain approximate size estimates for the samples through use of LII, the LII signals from the samples were evaluated under the assumption of these having a monodisperse particle distribution. Although these estimates are rough and the fitted signals do not in visual terms fit the experimental signals very well (Fig. 7.14), these correlate rather well with the LII-equivalent primary particle sizes as measured in the TEM images. The LII-equivalent primary particle size was determined by creating a modelled LII signal from the particle distribution as measured in the TEM images, and then fitting this signal by use of a monodisperse LII signal. The thermal accommodation parameter α_T was then adjusted to get the LII size for the sample SRB E6 to agree with the TEM measurement. A comparison of the LII and TEM particle sizes is shown in Table 7.2.

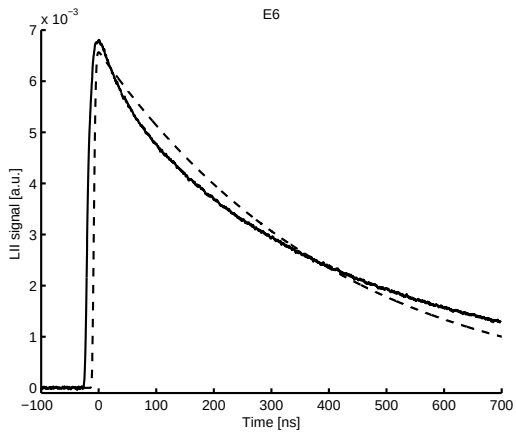

Figure 7.14: Experimental, 1000-shot averaged LII signal from the carbon black type SRB E6 (solid line) fitted using a modelled LII signal from a monodisperse size distribution (dashed line), normalised near their peaks, where the lines cross. The decay of the modelled signal is approximately exponential, but the experimental signal decays faster in the beginning of the signal than in the end. This might be an effect of the broad size distribution of the carbon black.

Table 7.2: Primary particle diameters for the Standard Reference Blacks A6, C6, E6 and F6, as determined using LII and TEM.

SRB	TEM [nm]	LII [nm]	STSA [nm]
A6	31.7	32.1	24.6
C6	42.3	40.0	42.1
E6	68.3	68.3	95.0
F6	65.7	68.8	97.7

Indicative diameters derived from surface measurements used in the carbon black industry (using the Statistical Thickness Surface Area, STSA and a surface to volume conversion formula, see Hernäng [22]) are shown in Table 7.2. Since the sizing methods used in these preliminary tests differ, it can only be said that the LII and the STSA results agree relatively closely with one another. For a detailed discussion of the differences between the diameters determined using TEM, LII and the STSA area, see Hernäng [22].

To accurately evaluate the properties of these aggregates by use of LII, the LII model and the fitting routines need to be improved. There are a number of things need to be taken into account, such as the fact that the aggregates are dense and that each of the aggregates consist of a large number of primary particles with bridging between them. The primary particles also differ considerably in size, just as the aggregates themselves do. Taking these facts into account adequately is difficult. Accurately measuring both the degree of aggregation and the primary particle sizes would probably require complementary information, for example from measurements of elastic light scattering.

7.2 Flat-flame Studies

7.2.1 Optical Soot Properties in the Growth Region

In Paper IV soot properties in the growth region of a flat flame were investigated using LII, TEM and coherent anti-Stokes Raman spectroscopy, CARS [9, 76]. How these properties change with soot particle age is of interest in order to better understand the soot formation process. It is also valuable to know how the properties vary, and how large the variation can be, in evaluating LII signals.

The experiments in question were carried out in an ethylene/air flame ($\Phi = 2.1$) on a bronze McKenna burner at a height of 4–17 mm above burner (HAB). At each height, the gas temperature was measured by use of N_2 rota-

tional CARS [77]. The LII measurements were carried out in the low-fluence regime, by relay-imaging of the letter-box, top-hat, part of the laser beam into the flame (0.13 J/cm^2, 1 × 4.8 mm). The profile was monitored by means of a beam profiler and a pulse energy meter. Detection was carried out at 445 nm and 575 nm, so that the peak temperature of the soot particles could be calculated by means of pyrometry. The general LII setup was the same as that described in Chapter 4. A probe was also employed for sampling the soot particles at the different heights and examining them by use of TEM.

The CARS temperatures were employed in the primary particle size evaluation using LII, as can be seen, together with the TEM primary particle size distributions, in Fig. 7.15. The LII-equivalent TEM size at 9 mm HAB was used for calibration of the LII particle sizes. It can be seen that the LII sizes increase more rapidly with height, especially above 10 mm HAB. At such heights, the difference can be explained in terms of the onset of aggregation, since the primary particle sizes as obtained by use of LII were not compensated for the aggregation that was present there, since statistics on aggregate size were not available.

Using the gas temperature, $T_{g,CARS}$, the LII peak temperature, $T_{p,max}$, and an LII model made it possible to calculate the variation in $E(m)$ with HAB, its being assumed that the product of the heat capacity and the density of the particles does not change with HAB. The results are shown in Fig. 7.16. As can be seen, $E(m)$ increases with HAB, its increasing from 0.2 to 0.45 when going from 7 to 17 mm HAB.

7.2.2 Assessment of the One-dimensionality of the McKenna burner

Flat flames on McKenna burners (Section 2.3.1) are of considerable interest in soot studies. They can be expected to produce flames that are approximately one-dimensional, meaning that within each horizontal section of the flame the conditions should be essentially the same. This is useful for making line-of-sight absorption measurements and also makes it possible to investigate soot of different age by looking at different heights in the flame. Although the one-dimensionality does not hold, of course, close to the flame edges, Migliorini et al. [21] found, when they investigated the one-dimensionality of premixed flames on their McKenna burner, the flames to be very inhomogeneous, also in the centre of the flames. Many of our experimental studies are based on

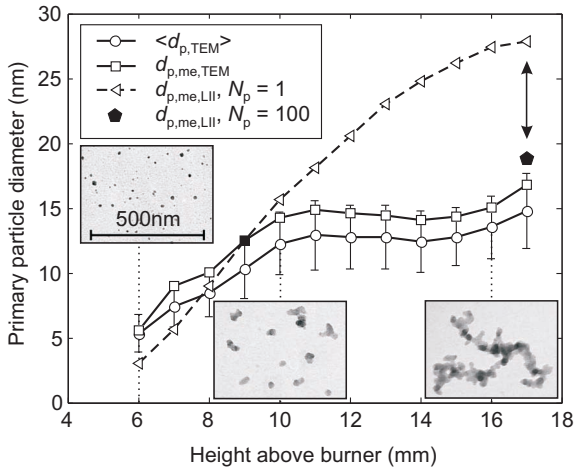

Figure 7.15: Primary particle sizes evaluated using TEM and LII. The error bars and $\langle d_{p,TEM} \rangle$ show the standard deviation and mean values of the TEM distributions. Note that $d_{p,me,TEM}$ is the LII monodisperse equivalent of the TEM distributions, calculated using the LII model and that $d_{p,me,LII}$ shows the sizes as evaluated on the basis of LII signals, calibrated to $d_{p,me,TEM}$ at 9 mm HAB. The pentagon shows how accounting for aggregation could possibly explain the gap between LII and TEM particle sizes.

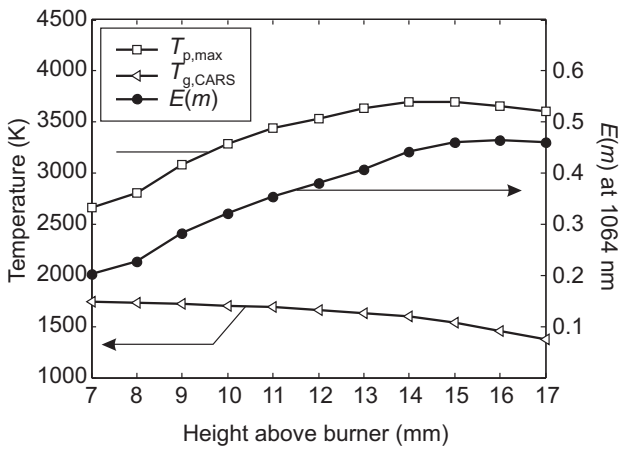

Figure 7.16: Peak soot particle temperature, $T_{p,max}$, flame temperature, $T_{g,CARS}$, and the absorption function $E(m)$, shown as function of HAB.

results applying to flames on the McKenna burner, but we have not seen any large variation with radial position in the flame. We decided to investigate the homogeneity of the flames on our burners and at the same time investigate the effect of different co-flows. It is important not only to know to what extent the flame on this kind of a burner is "flat", but also to know the properties of the flame near its edges.

The studies to determine this were carried out in two different premixed ethylene/air flames on a bronze McKenna burner from the early 1990s (Fig. 7.17). The equivalence ratio was $\Phi = 2.1$ and either nitrogen or air was used as the shroud gas, for purposes of stabilisation. A stainless-steel stabiliser was positioned with its lower edge at a height of 21 mm above burner (HAB). In an air-shroud flame it can be seen that the combustible gases near the edges react with the oxygen in the air-shroud, resulting in an outer diffusion flame.

To characterise the flame, rotational N_2 coherent anti-Stokes Raman spectroscopy (CARS) [9, 76, 77] was used for flame temperature measurements, T_g; LII for particle sizing, d_p, and soot volume fraction measurements, f_v; and elastic light scattering (ELS) [19, 68] for calculating the differential scattering coefficient, Q_{vv}. These measurement were made radially 10 mm above burner, where the primary particles are for the most part non-aggregated. These data were complemented by imaging measurements of the ELS signal at 8, 10 and 12 mm HAB.

The CARS measurements showed the flame temperatures to vary with less than ~1 % within each of the two flames, at radial positions $r \leq 23$ mm. The temperatures in the air shroud flame were slightly higher than those in the nitrogen shroud flame, 5–10 K, although this difference was at the limit of significance. Outside this region, the temperature of the nitrogen-shroud flame fell off, because of the inert N_2 there, whereas the temperature first increases before decreasing then in the case of the air-shroud flame, due to outer shroud flame.

The primary particle sizes provided by LII (Fig. 7.18) show only a slight variation from the centre to $r = 16$ mm. Outside this range, the particle sizes decrease in the nitrogen shroud flame, probably due to cooling by the nitrogen shroud. The particle sizes in the air-shroud flame remain quite stable out to $r = 15$ mm, probably because of the gas temperature being maintained by the shroud flame.

The soot volume fraction and the differential scattering coefficient measurements showed trends associated with radial position that in qualitative terms

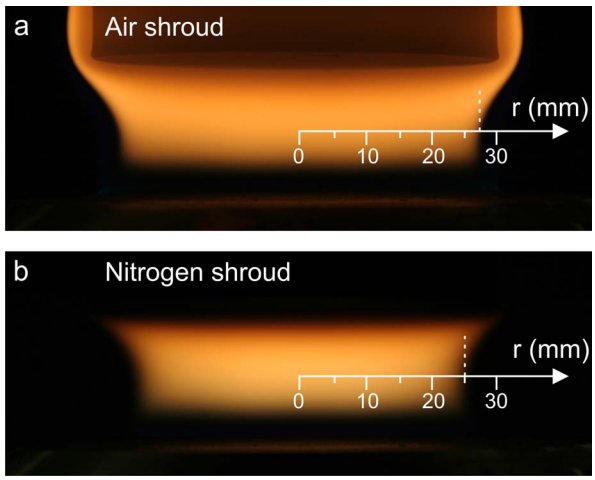

Figure 7.17: Ethylene/air flames obtained using **a**) an air shroud gas and **b**) a nitrogen shroud gas, where for both $\Phi = 2.1$. Most of the measurements were carried out as functions of the radial position at 10 mm HAB, as shown by the vertical positions of the scales in the images.

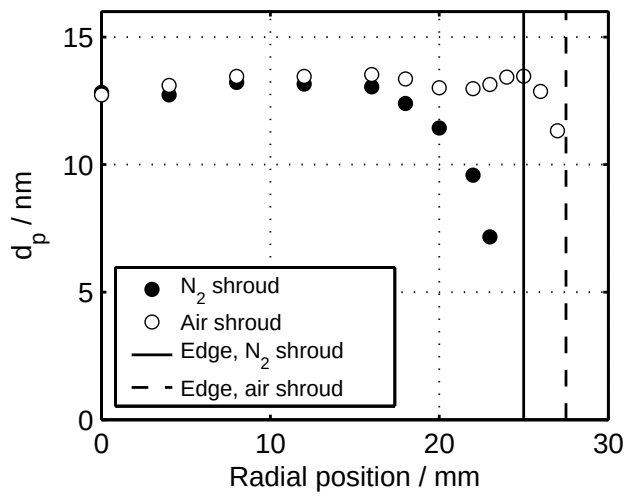

Figure 7.18: Primary particle diameters as assessed using LII, shown as function of the radial position in the flames.

appeared quite similar to those evident in Fig. 7.18. However, the magnitude of the variations was clearly stronger for f_v and was much greater for Q_{vv}. Since $f_v \propto d_p^3$ and $Q_{vv} \propto d_p^6$ for spherical particles in the Rayleigh regime, we decided to plot d_p determined by use of time-resolved LII, $\sqrt[3]{f_v}$ and $\sqrt[6]{Q_{vv}}$, normalised in the same plot, Fig. 7.19. Making this comparison means assuming that the primary particle size is the only explanation for the variations in f_v and Q_{vv} that are found, although other parameters might also explain the variation. However, the normalised curves in Fig. 7.19 show that the variations in d_p, $\sqrt[3]{f_v}$ and $\sqrt[6]{Q_{vv}}$ are very similar in magnitude and position, especially in the inner part of the flame, out to about $r = 16$ mm. Thus, it is plausible to assume that variations in d_p are the main cause of the variations in f_v and Q_{vv}.

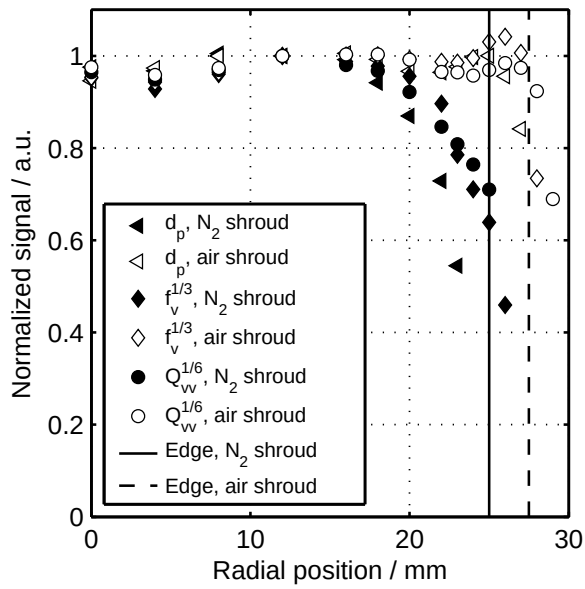

Figure 7.19: Primary particle diameters, d_p, as assessed using time-resolved LII, $\sqrt[3]{f_v}$ and $\sqrt[6]{Q_{vv}}$. The three functions are normalised at $r = 12$ mm.

The measurements obtained showed that the flames on the bronze McKenna burner clearly shows one-dimensional properties, as long as measurements are

made sufficiently far from the edges of the flame. The air-shroud flame had one-dimensional properties also close to the flame edges, because of the supporting shroud flame.

Two other McKenna burners were also investigated with respect to their one-dimensionality, although not to the extent described above; the one a stainless-steel McKenna burner from the early 1990s and the other a bronze McKenna burner manufactured by Holthuis and Associates in 2010. The burner from 2010 in particular, showed inhomogeneous ELS profiles, similar to those observed by Migliorini et al. [21]. This implies it to be important to characterize the flames from burners carefully so as to ensure that the one-dimensional properties are present.

Chapter 8

Summary and Outlook

In the work reported on here the diagnostic technique LII was investigated, tested and developed further, and it was applied in different laboratory flames and soot sources. A laboratory LII system having close control of the spatial laser beam profile and measurement volume was designed and set up. This setup, with minor variations, was used to test the effect of beam profile shape on LII measurements (Paper II), as well as to investigate the properties of soot in a flame on an McKenna burner (Paper IV) and for determining the one-dimensionality of a similar flame (Paper VI). In addition, the behaviour of LII when taking measurements on sources of cold soot was investigated, the results obtained being compared with those of complementary techniques (Paper V). Also, three theoretical studies were carried out. The relationship between the prompt LII signal and the soot volume fraction was examined and certain best practices were suggested for improving the accuracy of the linear relationship between the signal and the volume fraction (Paper I). The effect of a bimodal particle size distribution on LII evaluation was also tested, assuming that only one mode was present (Paper III). Finally, the effect on LII of bridging between the primary particles in soot aggregates was investigated (Paper VII).

The work as a whole provides information that can be used to improve LII as a soot diagnostic technique, and can contribute to an understanding of how best to use LII and interpret LII measurements. Two main issues connected with LII are uncertainties regarding both the absorption function $E(m)$ and the thermal accommodation coefficient α_T of soot. For nascent particles these issues are more complicated, since it was shown in Paper IV that $E(m)$ and, possibly, α_T, as well as particle heat capacity and density, change with particle age. The fact that particle properties can change with the height above the burner has also been shown by Cléon et al. [78] and Maffi et al. [79]. Since accurate LII measurements rely on having adequate values for the relevant soot properties, well-characterized soot sources are very useful in developing LII.

The present work improves on knowledge of soot properties in some specific, well-defined flat flames on the McKenna burner (Papers IV and VI).

In recent years, interest in using elastic light scattering (ELS) to measure soot aggregate properties has been increasing within the LII community. The angle-dependence of ELS obtained from soot aggregates can be used in determining aggregate size (radius of gyration) and the aggregate fractal dimension [68]. It has been shown that the detection of the elastic light scattering at many different angles relative to the laser beam can be used in determining the aggregate size distribution [80,81]. By combining the information obtained from ELS with evaluations of primary particle size on the basis of LII signals a more complete picture of the aggregates could be obtained. It can also be worthwhile to combine LII with SMPS or similar probe techniques, which we showed in Paper V to be a promising approach. Although these techniques are more intrusive than laser-based techniques, use of them can provide additional information regarding soot properties, such as the aggregate mass, and the distribution of number of primary particles per aggregate. In addition to increasing our knowledge of soot properties, such comparisons between different techniques can also provide insight into their respective limits and strengths.

It is clear that the development of LII depends in part on having insight into a wide variety of different areas, as well as associated skills. In the study reported in Paper VII, for example, it was important to have a close understanding of the background of soot aggregate modelling, of how to construct aggregates numerically and of how to perform Monte Carlo calculations, in order to obtain the shielding factor for the LII model. Another example, not concerned with the present work, is the analysis of TEM images of soot samples, often used for verifying or calibrating results of LII measurements. Interpreting the aggregate structures found on the basis of the images obtained is a topic of its own. For example, since soot aggregates seldom consist of completely spherical primary particles and usually only 2-D projected images are available, it can be difficult to objectively define primary particle diameters. In developing LII it is also important to understand the details of the LII model and the uncertainties in its parameters. It is very useful also to be knowledgeable within different areas of mathematics in evaluating LII signals, such as knowing how to best apply different inversion techniques to mathematically difficult, so-called ill-posed problems. Although it is far from trivial, it may also be possible to use mathematical techniques to provide better estimates of the uncertainties of an LII measurement, through including the uncertainties in different parameters used in the experiment and in the model when performing the evaluation.

Both the advantages in combining different techniques so as to improve LII and the various skills needed to improve LII evaluations suggest it to be worthwhile to keep working towards increasing the cross-disciplinary connections to groups that are more experienced within different areas. Our group has close connections with the Aerosol Technology Division and with Electrical and Information Technology at Lund University, but close connections with other groups in other areas should be considered.

I believe that the development of LII and related techniques could progress more rapidly if the kinds of computer programs that are commonly needed (and that are reasonable stable in their implementation) could be created in a collaborative effort within the LII community. I believe that an extensible LII model, together with appropriate aggregation construction routines and programs for TEM image analysis could fit this description. These should preferably be available as open source code and be documented, supported and improved by the LII community. Insights from different groups within the community could then be incorporated in the same programs, enabling more rapid progress to be attained and easier ways of comparing results from different research groups to be achieved. Indeed, in the 2012 LII Workshop, the idea of a community-supported LII model code was discussed.

Bibliography

[1] S. R. James, R. W. Dennell, A. S. Gilbert, H. T. Lewis, J. A. J. Gowlett, T. F. Lynch, W. C. McGrew, C. R. Peters, G. G. Pope, A. B. Stahl, and S. R. James. Hominid use of fire in the lower and middle pleistocene: A review of the evidence [and comments and replies]. *Current Anthropology*, 30(1):1–26, 1989.

[2] International Energy Agency. Key world energy statistics 2011, 2011.

[3] S. Solomon, D. Qin, M. Manning, Z. Chen, M. Marquis, K. B. Averyt, M. Tignor, and H. L. Miller, editors. *Climate Change 2007: The Physical Science Basis – Contribution of Working Group I to the Fourth Assessment Report of the Intergovernmental Panel on Climate Change (IPCC)*. Cambridge University Press, 2007.

[4] E. J. Highwood and R. P. Kinnersley. When smoke gets in our eyes: The multiple impacts of atmospheric black carbon on climate, air quality and health. *Environment International*, 32(4):560–566, 2006.

[5] C. Arden, R. T. Burnett, M. J. Thun, E. E. Calle, D. Krewski, K. Ito, and G. D. Thurston. Lung cancer, cardiopulmonary mortality, and long-term exposure to fine particulate air pollution. *Journal of the American Medical Association*, 287:1132–1141, 2002.

[6] Irvin Glassman. *Combustion*. Academic Press, San Diego, 3rd edition, 1996.

[7] Stephen R. Turns. *An Introduction to Combustion: Concepts and Applications*. McGraw-Hill Higher Education, Singapore, 2nd edition, 2000.

[8] John F. Griffiths and John Allan Barnard. *Flame and Combustion*. Blackie Academic & Professional, London, 3rd edition, 1995.

[9] Alan C. Eckbreth. *Laser Diagnostics for Combustion Temperature and Species*. Combustion science and technology book series, 3. Gordon & Breach, New York, 2nd edition, 1996.

[10] John B. Heywood. *Internal Combustion Engine Fundamentals*. McGraw-Hill series in mechanical engineering. McGraw-Hill, New York, 1988.

[11] A. D'Anna. Combustion-formed nanoparticles. *Proceedings of the Combustion Institute*, 32:593–613, 2009.

[12] H. Wang. Formation of nascent soot and other condensed-phase materials in flames. *Proceedings of the Combustion Institute*, 33:41–67, 2011.

[13] H. A. Michelsen. Understanding and predicting the temporal response of laser-induced incandescence from carbonaceous particles. *Journal of Chemical Physics*, 118(15):7012–7045, 2003.

[14] C. Schulz. Special issue: Laser-induced incandescence. *Applied Physics B*, 83(3):331–331, 2006.

[15] S. S. Krishnan, K. C. Lin, and G. M. Faeth. Optical properties in the visible of overfire soot in large buoyant turbulent diffusion flames. *Journal of Heat Transfer*, 122(3):517–524, 2000.

[16] S. S. Krishnan, K. C. Lin, and G. M. Faeth. Extinction and scattering properties of soot emitted from buoyant turbulent diffusion flames. *Journal of Heat Transfer*, 123(2):331–339, 2001.

[17] W. H. Dalzell and A. F. Sarofim. Optical constants of soot and their application to heat flux calculations. *Journal of Heat Transfer*, 91:100–104, 1969.

[18] D. R. Snelling, F. S. Liu, G. J. Smallwood, and Gülder Ö. L. Determination of the soot absorption function and thermal accommodation coefficient using low-fluence LII in a laminar coflow ethylene diffusion flame. *Combustion and Flame*, 136(1-2):180–190, 2004.

[19] Craig F. Bohren and Donald R. Huffman. *Absorption and Scattering of Light by Small Particles*. Wiley, New York, 1998.

[20] A. Bohlin and P.-E. Bengtsson. Rotational cars for accurate thermometry in standardized flat premixed flames, 2009. Joint Meeting: Scandinavian-Nordic and French Sections November 9–10, Copenhagen.

[21] F. Migliorini, S. De Iuliis, F. Cignoli, and G. Zizak. How "flat" is the rich premixed flame produced by your McKenna burner? *Combustion and Flame*, 153(3):384 – 393, 2008.

[22] N. Hernäng. Experimental investigations of carbon black aerosols. Master's thesis, Lund University, 2009.

[23] Carbon Black User's Guide: Safety, Health, & Environmental Information, International Carbon Black Association. 2004. http://carbonblack.org/carbonblackuserguide.pdf.

[24] R. W. Weeks and W. W. Duley. Aerosol-particle sizes from light emission during excitation by TEA CO_2 laser pulses. *Journal of Applied Physics*, 45(10):4661–4662, 1974.

[25] A. C. Eckbreth. Effects of laser-modulated particulate incandescence on Raman scattering diagnostics. *Journal of Applied Physics*, 48:4473–4479, 1977.

[26] S. Will, S. Schraml, and A. Leipertz. 2-dimensional soot-particle sizing by time-resolved laser-induced incandescence. *Optics Letters*, 20(22):2342–2344, 1995.

[27] P. Roth and A. V. Filippov. In situ ultrafine particle sizing by a combination of pulsed laser heatup and particle thermal emission. *Journal of Aerosol Science*, 27(1):95–104, 1996.

[28] R. L. Vander Wal and M. Y. Choi. Pulsed laser heating of soot: Morphological changes. *Carbon*, 37:231–239, 1999.

[29] L. A. Melton. Soot diagnostics based on laser-heating. *Applied Optics*, 23(13):2201–2208, 1984.

[30] J. E. Dec. Soot distribution in a D. I. Diesel engine using 2-D imaging of laser-induced incandescence, elastic scattering, and flame luminosity. *SAE Technical Paper 920115*, 1992.

[31] R. L. Vander Wal and D. L. Dietrich. Laser-induced incandescence applied to droplet combustion. *Applied Optics*, 34(6):1103–1107, 1995.

[32] P.-E. Bengtsson and M. Alden. Soot-visualization strategies using laser techniques: Laser-induced fluorescence in C_2 from laser-vaporized soot and laser-induced soot incandescence. *Applied Physics B: Lasers and Optics*, 60(1):51–59, 1995.

[33] H. A. Michelsen. Derivation of a temperature-dependent accommodation coefficient for use in modeling laser-induced incandescence of soot. *Applied Physics B*, 94:103–117, 2009.

[34] P.-E. Bengtsson and M. Aldén. C_2 production and excitation in sooting flames using visible laser-radiation: Implications for diagnostics in sooting flames. *Combustion Science and Technology*, 77(4-6):307–318, 1991.

[35] C. Schulz, B. F. Kock, M. Hofmann, H. Michelsen, S. Will, B. Bougie, R. Suntz, and G. Smallwood. Laser-induced incandescence: recent trends and current questions. *Applied Physics B*, 83(3):333–354, 2006.

[36] J. Zerbs, K. P. Geigle, O. Lammel, J. Hader, R. Stirn, R. Hadef, and W. Meier. The influence of wavelength in extinction measurements and beam steering in laser-induced incandescence measurements in sooting flames. *Applied Physics B: Lasers and Optics*, 96:683–694, sep 2009.

[37] W. T. Ham, Jr., J. J. Ruffolo, Jr., and D. Guerry III. The nature of retinal radiation damage: Dependence on wavelength, power level and exposure time. *Vision Research*, 20(12):1105–1111, 1991.

[38] David B. Williams and C. Barry Carter. *Transmission Electron Microscopy*. Plenum Press, 1996.

[39] William C. Hinds. *Aerosol Technology: Properties, Behavior, and Measurement of Airborne Particles*. Wiley-Interscience, 2 edition, 1999.

[40] Orazio Svelto and David C. Hanna. *Principles of lasers*. Plenum Press, New York, 4th edition, 1998.

[41] M. Charwath, R. Suntz, and H. Bockhorn. Influence of temporal resolution on time-resolved laser-induced incandescence signal evolutions. *Applied Physics B*, 83(3):435–442, 2006.

[42] H. Bladh. *On the use of laser-induced incandescence for soot diagnostics – From theoretical aspects to applications in engines*. PhD thesis, Lund University, 2007.

[43] Lev S. Ruzer and Naomi H. Harley, editors. *Aerosols Handbook – Measurement, Dosimetry, and Health Effects*. CRC Press LLC, 2005.

[44] F. Liu, M. Yang, F. A. Hill, D. R. Snelling, and G. J. Smallwood. Influence of polydisperse distributions of both primary particle and aggregate size on soot temperature in low-fluence LII. *Applied Physics B*, 83(3):383–395, 2006.

[45] B. J. McCoy and C. Y. Cha. Transport phenomena in rarefied-gas transition regime. *Chemical Engineering Science*, 29(2):381–388, 1974.

[46] A. V. Filippov and D. E. Rosner. Energy transfer between an aerosol particle and gas at high temperature ratios in the Knudsen transition regime. *International Journal of Heat and Mass Transfer*, 43(1):127–138, 2000.

[47] N. A. Fuchs. On the stationary charge distribution on aerosol particles in a bipolar ionic atmosphere. *Pure and Applied Geophysics*, 56(1):185–193, 1963.

[48] F. Liu, K. J. Daun, D. R. Snelling, and G. J. Smallwood. Heat conduction from a spherical nano-particle: status of modeling heat conduction in laser-induced incandescence. *Applied Physics B*, 83(3):355–382, 2006.

[49] D. R. Snelling, F. Liu, G. J. Smallwood, and Ö. L. Gülder. Evaluation of the nanoscale heat and mass transfer model of the laser-induced incandescence: Prediction of the excitation intensity. In *Proceedings of the 34th National Heat Transfer Conference*, volume NHTC2000-12132, Pittsburg, PA, 2000.

[50] G. J. Smallwood, D. R. Snelling, F. Liu, and Ö. L. Gülder. Clouds over soot evaporation: Errors in modeling laser-induced incandescence of soot. *Journal of Heat Transfer*, 123(4):814–818, 2001.

[51] D. Lichtman and Y. Shapira. Photodesorption: A critical review. *Critical Reviews in Solid State and Materials Sciences*, 8(1):93–118, 1978.

[52] N. Jarosik, C. L. Bennett, J. Dunkley, B. Gold, M. R. Greason, M. Halpern, R. S. Hill, G. Hinshaw, A. Kogut, E. Komatsu, D. Larson, M. Limon, S. S. Meyer, M. R. Nolta, N. Odegard, L. Page, K. M. Smith, D. N. Spergel, G. S. Tucker, J. L. Weiland, E. Wollack, and E. L. Wright. Seven-year Wilkinson Microwave Anisotropy Probe (WMAP) observations: Sky maps, systematic errors, and basic results. *The Astrophysical Journal Supplement Series*, 192(2), 2011.

[53] K. Tian, F. S. Liu, K. A. Thomson, D. R. Snelling, G. J. Smallwood, and D. S. Wang. Distribution of the number of primary particles of soot aggregates in a nonpremixed laminar flame. *Combustion and Flame*, 138(1-2):195–198, 2004.

[54] K. J. Daun, B. J. Stagg, F. Liu, G. J. Smallwood, and D. R. Snelling. Determining aerosol particle size distributions using time-resolved laser-induced incandescence. *Applied Physics B*, 87(2):363–372, 2007.

[55] Ü. Ö. Köylü, G. M. Faeth, T. L. Farias, and M. G. Carvalho. Fractal and projected structure properties of soot aggregates. *Combustion and Flame*, 100:621–633, 1995.

[56] A. V. Filippov, M. Zurita, and D. E. Rosner. Fractal-like aggregates: Relation between morphology and physical properties. *Journal of Colloid and Interface Science*, 229(1):261–273, 2000.

[57] B. B. Mandelbrot. *Fractals: Form, Chance and Dimension*. W. H. Freeman & Co Ltd, San Francisco, 1977.

[58] H. von Koch. Sur une courbe continue sans tangente obtenne par une construction géométrique élémentaire. *Arkiv för Matematik, Astronomi och Fysik*, 1:681–702, 1904.

[59] J. Theiler. Estimating fractal dimension. *Journal of the Optical Society of America A*, 7(6):1055–1073, 1990.

[60] K. C. Clarke and D. M. Schweizer. Measuring the fractal dimension of natural surfaces using a robust fractal estimator. *Cartography and Geographic Information Systems*, 18(1):37–47, 1991.

[61] P. Meakin. Fractal aggregates in geophysics. *Reviews of Geophysics*, 29(3):317–354, 1991.

[62] M. K. Wu and S. K. Friedlander. Note on the power law equation for fractal-like aerosol agglomerates. *Journal of Colloid and Interface Science*, 159:246–248, August 1993.

[63] Ü. Köylü, Y. Xing, and D. E. Rosner. Fractal morphology analysis of combustion-generated aggregates using angular light scattering and electron microscope images. *Langmuir*, 11:4848–4854, December 1995.

[64] A. M. Brasil, T. L. Farias, and M. G. Carvalho. Evaluation of the fractal properties of cluster–cluster aggregates. *Aerosol Science and Technology*, 33:440–454, November 2000.

[65] C. Oh and C. M. Sorensen. The effect of overlap between monomers on the determination of fractal cluster morphology. *Journal of Colloid and Interface Science*, 193:17–25, September 1997.

[66] A. M. Brasil, T. L. Farias, and M. G. Carvalho. A recipe for image characterization of fractal-like aggregates. *Journal of Aerosol Science*, 30(10):1379–1389, 1999.

[67] Ü. Ö. Köylü. Fractal and projected structure properties of soot aggregates. *Combustion and Flame*, 100:621–633, 1995.

[68] C. M. Sorensen. Light scattering by fractal aggregates: A review. *Aerosol Science and Technology*, 35(2):648–687, 2001.

[69] J. C. Maxwell. On stresses in rarified gases arising from inequalities of temperature. *Philosophical Transactions of the Royal Society of London*, 170:231–256, 1879.

[70] K. J. Daun. Effect of selective accommodation on soot aggregate shielding in time-resolved laser-induced incandescence experiments. *Journal of Heat Transfer*, 132:091202–, 2010.

[71] Federick Reif. *Fundamentals of statistical and thermal physics*, pages 262–273. McGraw-Hill Book Company, Singapore, 1985.

[72] F. Liu and G. J. Smallwood. Effect of aggregation on the absorption cross-section of fractal soot aggregates and its impact on LII modelling. *Journal of Quantitative Spectroscopy and Radiative Transfer*, 111:302–308, January 2010.

[73] B. Mewes and J. M. Seitzman. Soot volume fraction and particle size measurements with laser-induced incandescence. *Applied Optics*, 36(3):709–717, 1997.

[74] A. D. Abid, N. Heinz, E. D. Tolmachoff, D. J. Phares, C. S. Campbell, and H. Wang. On evolution of particle size distribution functions of incipient soot in premixed ethylene-oxygen-argon flames. *Combustion and Flame*, 154(4):775 – 788, 2008.

[75] R. Stirn, T. Gonzalez Baquet, S. Kanjarkar, Meier W., K. P. Geigle, H. H. Grotheer, C. Wahl, and M. Aigner. Comparison of particle size measurements with laser-induced incandescence, mass spectroscopy, and scanning mobility particle sizing in a laminar premixed ethylene/air flame. *Combustion Science and Technology*, 181(2):329–349, 2009.

[76] S. Roy, J. R. Gord, and A. K. Patnaik. Recent advances in coherent anti-Stokes Raman scattering spectroscopy: Fundamental developments and applications in reacting flows. *Progress in Energy and Combustion Science*, 36(2):280–306, 2010.

[77] F. Vestin, M. Afzelius, C. Brackmann, and P.-E. Bengtsson. Dual-broadband rotational CARS thermometry in the product gas of hydrocarbon flames. *Proceedings of the Combustion Institute*, 30(1):1673–1680, 2005.

[78] G. Cléon, T. Amodeo, A. Faccinetto, and P. Desgroux. Laser induced incandescence determination of the ratio of the soot absorption functions at 532 nm and 1064 nm in the nucleation zone of a low pressure premixed sooting flame. *Applied Physics B*, 104:297–305, 2011.

[79] S. Maffi, S. De Iuliis, F. Cignoli, and G. Zizak. Investigation on thermal accommodation coefficient and soot absorption function with two-color Tire-LII technique in rich premixed flames. *Applied Physics B*, 104:357–366, 2011.

[80] O. Link, D. R. Snelling, K. A. Thomson, and G. J. Smallwood. Development of absolute intensity multi-angle light scattering for the determination of polydisperse soot aggregate properties. *Proceedings of the Combustion Institute*, 33:847–854, 2011.

[81] D. W. Burr, K. J. Daun, K. A. Thomson, and G. J. Smallwood. Optimization of measurement angles for soot aggregate sizing by elastic light scattering, through design-of-experiment theory. *Journal of Quantitative Spectroscopy and Radiative Transfer*, 113:355–365, 2012.

Acknowledgements

During the time I have worked at the Division of Combustion Physics at Lund University I have had the opportunity to work with many people. I want to thank you all for contributing to the friendly atmosphere at the division, for interesting discussions, good collaboration in different tasks and for the numerous hours of fun we have had together. I would like to particularly express my appreciation to the following persons.

I want to especially thank Prof. Per-Erik, my supervisor, for giving me the opportunity to work at the division. You have taught me a lot about how to work as a scientist and your guidance and support have been of great value to me. I appreciate that you have always taken the time to help me and discuss anything whenever I decided to knock on your door. Your constant striving for high-quality results has been an inspiration to me. I would also like to thank my assistant supervisor Dr. Henrik Bladh for numerous fruitful (as well as not-so-fruitful...) discussions on the subjects of physics and LII – and anything else! – and for helping me with the laboratory work. Thank you for being so patient with me when I am constantly interrupting you in your work. You have both helped me so much during the years, and I appreciate that you have given me the opportunity to go abroad for conferences so many times. Some notable and memorable trips were to Canada (my first LII Workshop and Combustion Symposium), China (having a talk at the Combustion Symposium) and Italy – the last being memorable because it did not happen, since Eyjafjallajökull suddenly decided to throw an enormous amount of ash into our flight path. Nils-Erik Olofsson joined us in the soot group a few years after I started and has been a great addition to our small team. I have enjoyed working with all of you.

I would also like to thank Prof. Marcus Aldén, head of the division, for continuously working on keeping the division at the forefront of the field of laser diagnostics for combustion applications.

One thing that has been a constant during my years at the division is the reliable lunch company of Edouard Berrocal, Christoph Knappe, Alexis Bohlin and, until recently, David Sedarsky. It has been a pleasure! The most frequently recurring topic during these lunches has been that of the differences of

customs and mindsets in Sweden, France, Germany and the USA. Occasionally we have also discussed work-related matters and from Edouard I have over the years learned more about Monte Carlo simulations, droplets and optical depths than I ever feared for in my worst nightmares.* Ed, thank you for your energetic support, your humour (good and bad) and your never-ending stream of new amazing ideas. Christoph, thank you for all the fun times and for your contagious laughter that always cheers me up.

Elias Kristensson and I have shared the same office from day one and it has worked out very well.† You have always been available when I have needed to ask quick questions or wanted to discuss various problems or ideas that pop up. I also greatly appreciate the spontaneous composition of new songs that have frequently occurred, as well as the long period of only listening to a single song by Nina Simone or Muse.‡ Johannes Lindén and Johan Sjöholm have been located in the office next door. Because their office is also close to the printers it has been putting them at great risk of being interrupted by me, either when taking a break or when wanting to discuss some research of current interest. Thank you for your patience. I have learned to know Johannes also at my two main hobbies during these years, singing in a choir and dancing, and I very much appreciate your infectious positive energy.

Thank you Andreas Lantz, Olof Johansson, Linda Vallenhag, Nils-Erik Olofsson and Ronald Whiddon not only for working with you on occasional work- or study-related matters but also for being part of making the work environment at this division so great. I want to thank Andreas for all corridor discussions and for being a great floorball team-mate, Linda and Olof for their never-ending (and often sarcastic) humour, Nille for his recurring mischief and Ron for his computer-related fearlessness.

I would like to thank Andreas Ehn and Sven-Inge Möller for several longer discussions of both experimental and theoretical nature. Andreas never ceases to come up with interesting experiments involving LII while Sven-Inge without hesitation discusses fun subjects such as Babylonian mathematics, group theory and obscure UNIX commands.

I had the pleasure of visiting New York together with Billy Kaldvee and Johan Zetterberg. It was fun to explore the city with you. The GPS that later helped us to the conference site in New Hampshire was, however, rather adventurous, preferring the "cattle track" through the woods to the boring mo-

*Just kidding, Ed. :-) I'm glad you taught me and it *is* interesting!

†Except for our beautiful flowers that now are all dead, except maybe for the cactus. As opposed to the case for Schrödinger's cat, looking at the cactus does not collapse its wavefunction.

‡"Opossum in the tree, you know what I mean."

torways. Although this route was indeed exciting, the next time I propose that we rent a car with a higher ground clearance.

Rutger Lorensson and Susanne Dunér: thank you for your support regarding any lab- or computer related issues.

The carbon black measurements in this work was carried out in cooperation with Nils Hernäng, and the measurements in the flame-based soot generator were made in collaboration with Hussam Abdulhamid, Joakim Pagels and Jenny Rissler at the Division of Ergonomics and Aerosol Technology (EAT), Lund University. I am also glad that we have cooperated with Anders Karlsson at the Division of Electrical and Information Technology (EIT), Lund University, and his students on matters regarding light scattering from soot aggregates. It has always been interesting and I have learned a lot. Thank you all for working with me in these projects.

Cecilia Bille, thank you for all your help with administrative and economy issues – especially in those last-minute cases. I have also received much needed help from Anneli Nilsson-Ahlm, Nina Mårtensson, Sara Holmgren, Eva Persson and Minna Ramkull to cope with the sometimes incomprehensible administrative systems. Thank you all for your assistance!

I would also like to express how important all of my non-work-related friends are to me. Without you this work would have been significantly more difficult to finish. I would like to especially thank my friends from Laurentiistiftelsen, my choir friends from Lunds Akademiska Kör and my lindy hopping friends. I would especially like to thank Zache for numerous (but not enough!) meetings with pizza, beer (or water...) and movies, and both Mia and Gustav, and Johannes and Magda for always welcoming me whenever I, usually on a whim, decide it would be fun to visit them.

Last I want to thank my family and extended family who are always there for me whenever I need it. Thank you mum, Christian, Staffan and Ingemar.

Contribution to Papers

I. I verified that the LII model in the paper was correctly implemented in Matlab, and did some verification that the model was internally consistent. I improved the performance of the Fuchs heat conduction code that was used in the LII model implementation. I participated in the preparation of the manuscript.

II. I designed the experimental setup together with Henrik Bladh and Per-Erik Bengtsson. I constructed the setup then together with Henrik Bladh, the two of us carrying out the experiments together. I adapted and optimised the implementation of the LII model so that it could be more easily employed for evaluations. I implemented the necessary algorithms for the particle size evaluation procedure. I made the model evaluations for the paper and wrote parts of the manuscript.

III. I was the main person responsible for the paper. I carried out the computer simulations and evaluations and wrote the manuscript.

IV. I carried out the particle size evaluations from the LII measurements and compared them to LII-equivalent particle sizes calculated from the TEM data. I analysed the results and figured out what they could reveal regarding changes in soot optical properties with height in the flame. I wrote parts of the manuscript.

V. I participated in the design of the soot generator which was later finalised by Hussam Abdulhamid. I set up the LII laser system together with Henrik Bladh and we made the LII measurements. I evaluated the particle sizes using the LII model and worked together with Jenny Rissler to calculate the aggregate size distribution from the combined LII and SMPS data. I wrote parts of the manuscript.

VI. I carried out the particle size evaluations from the LII measurements and participated in the manuscript preparation.

VII. I implemented the aggregate construction routines and the Monte Carlo code for calculating the heat conduction from the aggregates. I

worked out how to take bridging into account in the LII model and how to make comparisons between aggregates with and without bridging. I wrote the manuscript.